

CONTRACTOR REPORT

SAND81-8192/1
UC-62d
Unlimited Release

Alternate Central Receiver Power System, Phase II Volume I—Executive Summary

Martin Marietta Corporation

Prepared by Sandia National Laboratories, Albuquerque, New Mexico 87185
and Livermore, California 94550 for the United States Department of Energy
under Contract DE-AC04-76DP00789.

Printed January 1984

***When printing a copy of any digitized SAND
Report, you are required to update the
markings to current standards.***

Issued by Sandia National Laboratories, operated for the United States Department of Energy by Sandia Corporation.
NOTICE: This report was prepared as an account of work sponsored by an agency of the United States Government. Neither the United States Government nor any agency thereof, nor any of their employees, nor any of the contractors, subcontractors, or their employees, makes any warranty, express or implied, or assumes any legal liability or responsibility for the accuracy, completeness, or usefulness of any information, apparatus, product, or process disclosed, or represents that its use would not infringe privately owned rights. Reference herein to any specific commercial product, process, or service by trade name, trademark, manufacturer, or otherwise, does not necessarily constitute or imply its endorsement, recommendation, or favoring by the United States Government, any agency thereof or any of their contractors or subcontractors. The views and opinions expressed herein do not necessarily state or reflect those of the United States Government, any agency thereof or any of their contractors or subcontractors.

Printed in the United States of America
Available from
National Technical Information Service
5285 Port Royal Road
Springfield, VA 22161

NTIS price codes
Printed copy: A02
Microfiche copy: A01

MCR-81-1707
CONTRACT SANDIA-18-6879C

May 1981

FINAL REPORT

ALTERNATE CENTRAL RECEIVER
POWER SYSTEM, PHASE II

VOLUME I: EXECUTIVE SUMMARY

MARTIN MARIETTA DENVER AEROSPACE
P.O. Box 179
Denver, Colorado 80201

FOREWORD

This report is submitted by the Martin Marietta Corporation to Sandia Laboratories in accordance with the provisions of contract Sandia No. 18-6879C. This final report consists of the following volumes:

Volume I - Executive Summary (this volume)

Volume II - Molten Salt Receiver

Volume III - Molten Salt Materials Tests

The contract was under the technical direction of Mr. William C. Peila of Sandia Laboratories, Livermore, California. The following organizations have contributed to this work:

- 1) Martin Marietta Corporation (Denver) Program management and overall responsibility for the design, fabrication, and test phases of the Subsystem Research Experiments (SRE's), and for the refinement of the conceptual design of a commercial receiver.
- 2) Badger Energy, Inc. (Cambridge) Selection of critical molten salt components, control system engineering, and structural design of the molten salt system piping. Provide engineering expertise in the areas of design, manufacturing, and operation of molten salt components and subsystems.
- 3) Arizona Public Service Company (Phoenix) Utility observer of the test program at CRTF and contributor to the final report.

<u>TABLE OF CONTENTS</u>		<u>Page</u>
	Forewordii
I.	INTRODUCTION AND SUMMARYI-1 thru I-6
	A. Receiver SREI-1
	B. Materials TestingI-5
II.	EVOLUTION OF THE RECEIVER SRE DESIGNII-1 thru II-17
	A. Conceptual Design and LayoutII-1
	B. Scaling the SRE ReceiverII-3
	C. Pre-Test AnalysesII-4
	D. Supporting DocumentsII-16
III.	DESCRIPTION OF RECEIVER SRE DESIGN AND OPERATIONIII-1 thru III-27
	A. Test System DescriptionIII-1
	B. Test FacilityIII-15
	C. Instrumentation and Data ReductionIII-18
	D. Typical Daily Operation of the SRE ReceiverIII-20
	E. Description of Special TestsIII-23
	F. Test HistoryIII-27
IV.	RECEIVER PERFORMANCE AND TEST RESULTS	IV-1 thru IV-37
	A. Thermal Performance	IV-1
	B. Thermo-Structural Performance and Design Data	IV-11
	C. Thermo-Hydraulic PerformanceIV-19
	D. Receiver ControlIV-26
	E. Hardware ReliabilityIV-34
V.	COMMERCIAL RECEIVER DESIGN UPDATEV-1 thru V-10
	A. Modularity StudyV-1

TABLE OF CONTENTS (continued)

Page

	B. Control Zone Optimization	V-1
	C. Detailed Analysis of Preferred Configuration	V-4
	D. Comparison with SRE Results	V-10
VI.	DESCRIPTION OF MATERIALS COMPATIBILITY AND SALT CHEMISTRY TESTSVI-1 thru VI-10
	A. Materials Immersion TestsVI-1
	B. Mechanical Properties of Materials in Molten SaltVI-3
	C. Dynamic Testing - Molten Salt Flow LoopVI-5
	D. Salt Chemistry Tests	VI-9
VII.	MATERIALS AND SALT CHEMISTRY TEST RESULTSVII-1 thru VII-10
	A. Salt Chemistry	VII-1
	B. Molten Salt Flow Loop	VII-5
	C. Materials TestsVII-7
VIII.	CONCLUSIONS AND RECOMMENDATIONSVIII-1 thru VIII-5

LIST OF FIGURES		Page
I-1	Receiver SRE Schematic.	I-2
I-2	Artist's Concept of Receiver SRE - Cavity Configuration . . .	I-2
I-3	SRE and Heliostat Field During Operation.	I-3
II-1	Receiver SRE Candidate Configurations	II-2
II-2	Tube Metal Temperature vs Fluid Temperature - Cavity.	II-6
II-3	Performance Map - Cavity Configuration.	II-7
II-4	Results of Receiver Salt Cooldown Transient Analysis.	II-11
II-5	SRE Transient Response - 4-Minute Cloud (MITAS Simulation). . .	II-13
III-1	Simplified Receiver SRE Schematic	III-2
III-2	Artist's Concept of Receiver - Exposed Configuration.	III-3
III-3	Artist's Concept of Receiver - Cavity Configuration	III-3
III-4	Receiver SRE Control Console.	III-5
III-5	Receiver Tubes and Headers Subassembly.	III-9
III-6	Close-up of Welded Receiver Tubes	III-10
III-7	SRE Main Support Structure.	III-11
III-8	Air-Cooled Heat Exchanger (Air Cooler).	III-12
III-9	Molten Salt Sump and Vertical Cantilever Pump	III-14
III-10	General Layout of the Heliostat Array	III-16
III-11	CRTF Tower Cross Section.	III-17
III-12	Typical Colorgraphic CRT Display.	III-19
III-13	Typical Clear Day Operational Timeline.	III-21
IV-1	Output vs Input Plot.	IV-3
IV-2	Efficiency vs Input - Aim Point Comparison.	IV-4
IV-3	Efficiency vs Input - C_p Comparison	IV-4
IV-4	Output vs Input - Aim Point Comparison.	IV-5
IV-5	Existing Free Convection Correlations	IV-7
IV-6	Molten Salt Specific Heat vs Temperature.	IV-9
IV-7	Out-of-Plane Tube Deflections	IV-13
IV-8	Weld Failure Locations with Failure Dates	IV-15
IV-9	Permanent Tube Deformations	IV-18
IV-10	Pressures vs Flow Rate - Receiver SRE	IV-20
IV-11	Friction Factor vs Reynolds Number - Receiver SRE	IV-22
IV-12	Predicted and Actual Metal Temperatures vs Salt Temperatures. .	IV-24
IV-13	Temperature Profiles for Accelerated Cycles	IV-25
IV-14	Analog Receiver Control - Outlet Temperature.	IV-29
IV-15	Computer Algorithm Receiver Control - Outlet Temperatures . .	IV-29
IV-16	Block Diagram for Receiver Control Simulation	IV-31
IV-17	Temperature Response to Step Change in Salt Flow Rate	IV-32
IV-18	Modified Algorithm Response to Flux Transient	IV-33
IV-19	Trace Heater Failure Modes and Failure Rate	IV-35
V-1	Receiver Modularity Analysis.	V-2
V-2	Preferred Commercial Receiver Configuration	V-3
V-3	Commercial Receiver Cavity Layout - North, East, South Apertures	V-5
V-4	Stress Considerations - Commercial Receiver	V-7
V-5	Convection Losses as a Function of Gaps Between Receiver Tubes	V-8
VI-1	Molten Salt Flow Loop Schematic	VI-6
VI-2	Long-Term Molten Salt Flow Loop	VI-7
VI-3	Materials Coupons with Holder	VI-8

LIST OF TABLES

Page

II-1	Test Program Status	II-17
III-1	Instrumentation List.	III-19
III-2	Test Program Plan	III-24
III-3	Weekly Summary of Receiver SRE Testing - 8 Aug 80 to 19 Dec 80	III-27
V-1	Tube-to-Tube Salt Temperatures.	V-8
VI-1	Trace Contaminants Test Matrix.	VI-1
VI-2	Extended Immersion Test Matrix.	VI-2
VI-3	Special Purpose Materials Tested.	VI-3
VI-4	Intergranular Corrosion/Tensile Test Matrix	VI-3
VI-5	Stress Corrosion Test Matrix.	VI-4
VI-6	Environmental Effects Test Matrix	VI-9
VI-7	Molten Salt Regeneration Test Matrix.	VI-10
VII-1	Effect of Temperature on Conversion to Nitrite in Molten Salt	VII-3
VII-2	Room Temperature Tensile Properties of Materials After Nine Months Salt Exposure.	VII-10

The objective of the Phase II Alternate Central Receiver program was to demonstrate the feasibility of the molten salt central receiver power system by conducting a series of experiments and using the results to update the commercial-scale design developed during Phase I of the program. The experiments were directed at two levels of inquiry: the systems-level testing of a 5 MW_{th} molten salt receiver---hereafter referred to as the receiver SRE; and the investigation of molten salt chemistry and the compatibility of selected materials with molten salt. Detailed discussion of the receiver testing are contained in Volume II of this report, while the materials tests are the subject of Volume III.

A. RECEIVER SRE

The receiver SRE tests were conducted during the period from May through December of 1980, at the Central Receiver Test Facility (CRTF) operated by Sandia Laboratories for the Department of Energy in Albuquerque, NM. On-site assembly operations started in April of 1980, and were preceded by design, engineering, manufacturing, checkout, and partial assembly efforts initiated in April of 1979, at Martin Marietta Corporation in Denver, Colorado.

A simplified schematic of the receiver SRE is shown in Figure I-1. Molten salt (60% NaNO₃, 40% KNO₃) is maintained at 288°C (550°F) in the sump. A vertical cantilever pump circulates the molten salt through the receiver, which consists of 18 serpentine passes of Incoloy 800 tubes. The active area of the receiver panel is approximately 5.5 m (18 ft) wide and 4.0 m (13 ft) high. Solar energy from the CRTF heliostats is directed onto the receiver panel through an aperture, and heats the circulating salt to 566°C (1050°F). The salt then passes through a forced-draft, air-cooled heat exchanger where it is cooled to 288°C (550°F) before being returned to the sump. The heat exchanger is, of course, test-peculiar equipment, its function being to simulate heat removal by the energy conversion (and storage) subsystems of a commercial plant. The nominal input to the receiver was 5 MW_{th}, with 206 heliostats, each with a reflecting area of 37.2 m² (400 ft²).

Figure I-2 is an artist's concept of the receiver in its cavity configuration. The cavity assembly is a separate structure that mounts in front of the receiver tube panel. In front of the cavity's water-cooled aperture is the Real-Time Aperture Flux (RTAF) system, a Sandia Albuquerque-provided device used for power input measurements. Pneumatically-operated insulated doors are seen on either side of the aperture. Figure I-3 is a photographic overview of the receiver and the heliostat field during operation.

The SRE was designed to duplicate larger, commercial receivers with respect to inlet and outlet salt temperatures, peak flux levels, salt heat transfer coefficients, and power transients. The receiver was designed and coded to ASME Section I, and was fabricated with methods we expect will be used to build commercial receivers. Each of the 288 receiver absorber tubes is welded to the adjacent tubes by a tungsten inert gas (TIG) welding process.

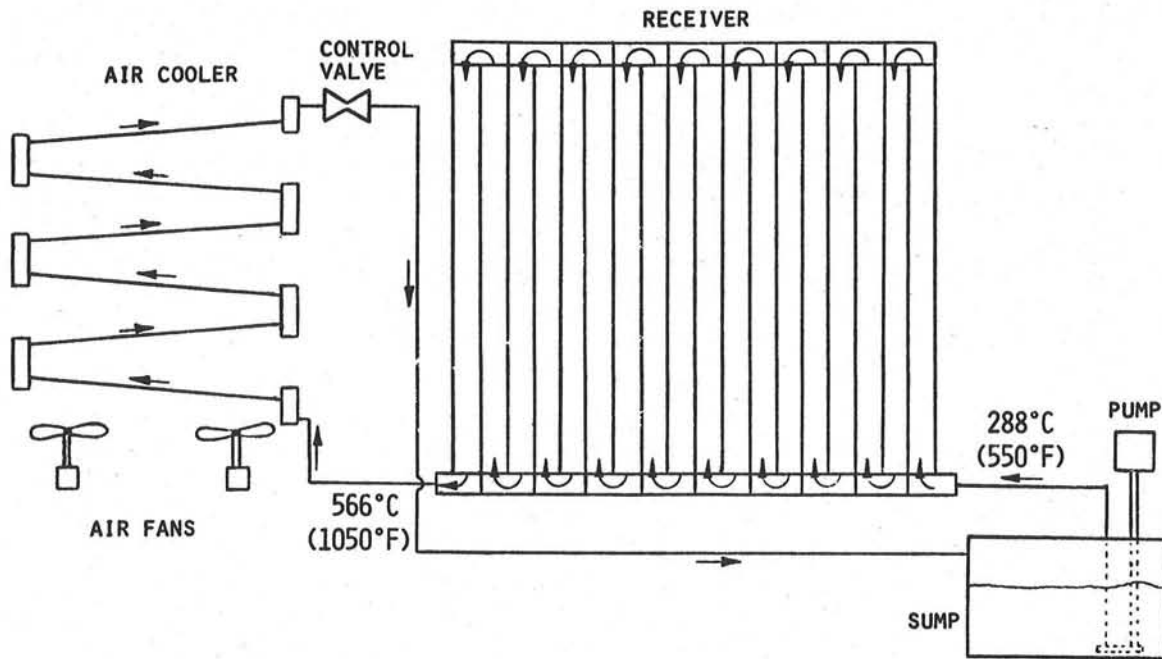


Figure I-1 Receiver SRE Schematic

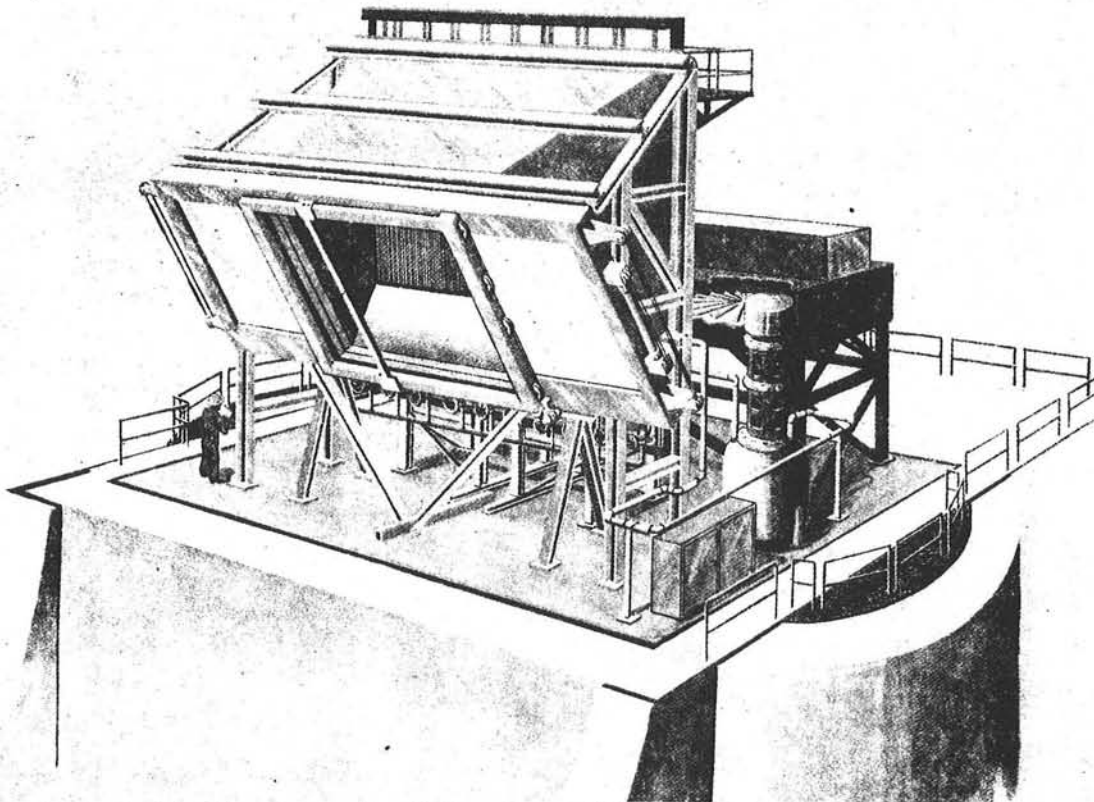


Figure I-2 Artist's Concept of Receiver SRE - Cavity Configuration

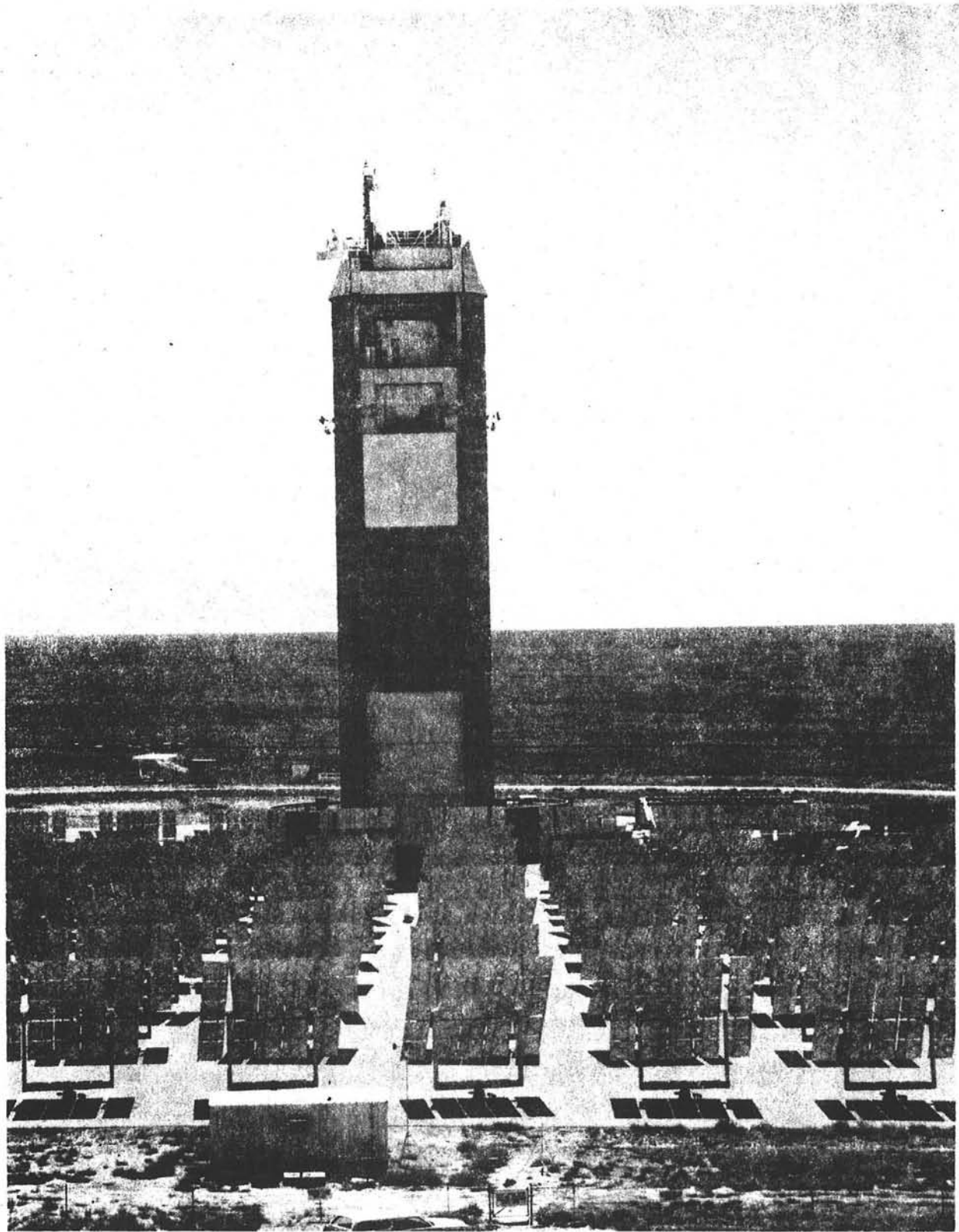


Figure I-3 SRE and Heliostat Field During Operation

The tests of the receiver SRE are believed to have made two significant contributions to the state-of-the-art of central receiver technology: they were the first successfully completed solar tests with a molten salt receiver; and they represent the first solar tests with a cavity type receiver of this size and complexity---at least in the United States. While both of these aspects of the demonstration are important to the commercial-scale effort, the emphasis in this program was primarily on molten salt technology. Specific questions that were to be resolved by the experiment may be grouped into four categories as follows:

- 1) Evaluation of molten salt (60% NaNO_3 , 40% KNO_3) as a heat transfer fluid for central receivers. This is a two-sided question pertaining to thermo/hydraulic as well as thermo/structural aspects of molten salt performance: Molten salt as an effective collector of solar energy at acceptable heat transfer coefficients and pumping requirements; and as an effective coolant to the receiver tubes (especially at partial loads and during cloud transients) to maximize the creep-fatigue life of the receiver.
- 2) Evaluation of thermal performance and its measureability with molten salt as the heat transfer fluid. The salt-oriented aspects of this question are closely related to Item (1) above and to the availability of appropriate thermophysical data; in a broader context it related to the progressing state-of-the-art of techniques for efficiency determinations by direct measurements.
- 3) Operational reliability of components and procedures: the demonstration of sustained operation of the salt-compatible pump, 26 valves, instrumentation, controls, auxiliary systems, and other components of the receiver; in conjunction with acceptable operational procedures in light of the constraints imposed by the high freezing point of salt [221°C (430°F)].
- 4) Applicability of existing design-, manufacturing-, and analytical techniques to molten salt receivers. This, in essence, establishes the state of development of molten salt receiver technology and the ability to predict receiver performance as applied to commercial-scale receiver design.

Following checkout tests with both water and salt, the SRE was subjected to a variety of solar tests, including performance evaluation under both steady state and transient conditions, "margin" tests at above-design flux levels, endurance tests, and accelerated cycle-fatigue life tests. During the reporting period, the SRE has accumulated 356 hours of solar exposure, 166.5 of which were at 100% load, and 96.3 hours at design conditions. It has withstood 153 cycles of accelerated life testing, and approximately an additional 100 cycles due to startups and cloud transients. The thermal efficiency of the SRE at design point conditions is 85.3%.

With some exceptions, detailed under Chapter VIII---Conclusions and Recommendations, all of the pre-test questions outlined above have been resolved affirmatively by the program. We conclude that the state-of-the-art of molten salt receiver technology is sufficiently advanced to permit full-scale demonstration as the next logical step.

B. MATERIALS TESTING

The materials and salt chemistry research experiments were designed to answer important questions on the use of molten salt mixtures of sodium and potassium nitrate in solar receiver applications.

The experiments were conducted to provide data on molten salt stability and materials compatibility which could be used in designing a commercial molten salt central receiver power system with a lifetime of 30 years or more. Specific questions addressed in designing these experiments were:

- o What construction materials could meet the design requirements for a solar receiver in a molten salt environment?
- o Will molten salt stability be adequate for long-term solar use?
- o How can the molten salt be repurified or regenerated if degradation occurs?
- o What effects might commercial salt impurities have on construction materials?
- o Will material surface preparation or finish have an effect on molten salt compatibility?
- o Do the mechanical properties of metal alloys change when exposed to molten salt?
- o Does a material transport mechanism exist in a flowing molten salt system with a thermal gradient?

Four different categories of tests were conducted: (1) materials compatibility; (2) materials mechanical properties; (3) dynamic testing; and (4) salt chemistry. The first two categories consisted of materials immersion tests. The dynamic testing was conducted in a molten salt flow loop covering a temperature gradient of 566°C (1050°F) to 288°C (550°F). The molten salt chemistry tests were carried out in test vessels with controlled thermal and atmospheric environments.

The results indicate that Incoloy 800 and RA330 are acceptable materials for long-term, high-temperature service [up to 580°C (1075°F)], and that 316 and 316L stainless may be acceptable subject to the results of further study. The results of tests on A570 carbon steel

indicate that it is acceptable for low temperature molten salt applications [up to 288°C (550°F)]. None of the low-nickel alloys tested were found to be acceptable for intermediate-temperature service [up to 400°C (750°F)].

We found the stability of the molten salt to be adequate for long-term solar use provided the carbonates and hydroxides are controlled (either with a CO₂/water vapor scrubber, or by regenerating the salt with NO₂).

There were no indications that the effects of surface preparation on mild steel material behavior are significant, and there does not seem to be any direct effect of molten salt exposure on materials properties. We did not find any thermal gradient-induced materials transport mechanisms in the salt flow loop. There are several areas requiring further investigation, and these are detailed in Chapter VIII, Conclusions and Recommendations. Included among these are the search for an intermediate-temperature alloy and more economical (substitute) high-temperature alloys, possibly in the low-chromium ferritic stainless steel family (2-1/4 Cr, 1 Mo). We also need to further investigate the deposits found in the intermediate-temperature sections of the molten salt flow loop.

Chapters II, III, and IV of this volume deal with the receiver SRE; Chapter V summarizes the commercial receiver design update; and Chapters VI and VII present a discussion of the materials tests. Conclusions and recommendations for future work are given in Chapter VIII.

II. EVOLUTION OF RECEIVER SRE DESIGN

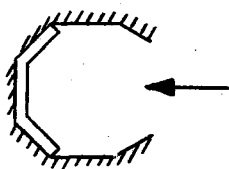
A. CONCEPTUAL DESIGN AND LAYOUT

The two key considerations for selection among alternative approaches during the conceptual design of the experiment were: (1) measurability of performance, and (2) the ability to extrapolate - or "scale" - the test results to commercial-size receivers. The measurability question centered chiefly around the use of the Real-Time Aperture Flux System (RTAF). The RTAF, supplied by the test facility, was considered the only reliable means available for this program for the measurement of power input to the SRE. It provides a flux map, and measurement of integrated power, over its 3.35 m x 3.35 m (11.0 ft x 11.0 ft) aperture area, which, under the above premise, sets an upper limit for the dimensions of the aperture of a cavity type SRE, or for the panel size of an exposed type SRE. It is possible to extrapolate the fluxes, measured by the RTAF to other geometries larger than its size analytically; this, however, was to be avoided in the SRE design, in order to maximize the reliability and accuracy of efficiency determinations. Another impact of the RTAF on SRE conceptual design was the choice of one-sided heating. This choice was based on the considerations outlined above and on the availability of only one RTAF system at the time. Two-sided heating was given serious consideration initially because of its impact on scalability, as discussed below.

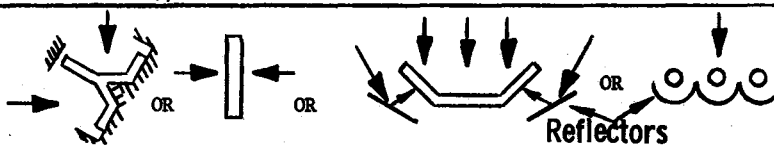
The preferred configuration of a commercial molten salt receiver was determined during previous studies.

Ideally, the SRE should have been a scale model of this full-size preferred concept, which is a four-aperture cavity-type receiver, as will be discussed in Chapter V. As shown in that chapter, the tube panels separating the cavities are heated from both sides, and this would have been desirable to duplicate within the SRE. Shown in Figure II-1 under "Cavity-Two-Sided Heating" are four concepts considered to accomplish this. All would require the use of reflectors and/or a rearrangement of the heliostat field. The complexity of such an arrangement was prohibitive from a standpoint of cost, schedule, and measurability of input (as discussed above), hence the two-sided heating concept was dropped from further consideration. The next step in the conceptual definition phase of the program was the selection between a cavity-type and an exposed-type SRE. The geometries considered in this selection process are depicted on Figure II-1. The cavity was selected as the baseline SRE configuration because of two overriding considerations: Its higher efficiency, shown by the results of the commercial receiver study; and its better protection against freezing of molten salt during startup and shutdown operations. Provisions have been made, however, for converting the cavity receiver into an exposed receiver panel (of the approximate size of the RTAF), so that the two basic receiver configurations could be tested.

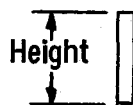
CAVITY - ONE SIDED HEATING



CAVITY - TWO SIDED HEATING

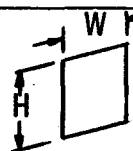


EXPOSED - MODULAR



Height of SRE \approx Height of Commercial Receiver

EXPOSED - "SCALED"



$W \approx H$

COMBINED CAVITY/EXPOSED

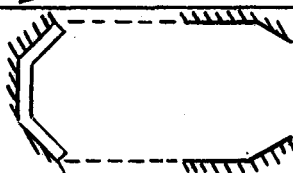


Figure II-1 Receiver SRE Candidate Configuration

The size of the SRE (in its cavity configuration) was selected to accept a nominal 5 MW input, consistent with the capability of CRTF. A smaller size would not have been cost effective; for example, reducing the size from 5 to 2 MW would only have reduced the cost by 20%, while jeopardizing the quality of obtainable performance data.

B. SCALING THE SRE RECEIVER

It is evident from the above the geometrical similarity between the preferred commercial receiver and the SRE could not be maintained. The scale modeling approach was, therefore, limited to "partial scaling" by designing the SRE for peak fluxes, average flux levels, fluid temperatures, Reynolds numbers, fluid velocities, Prandtl numbers and the use of materials and processes that are representative of full-scale applications.

There are two additional considerations related to scaling that need elaboration: spillage; and the distribution of incident fluxes on the internal surfaces of the cavity. These are related to the overall geometry of the heliostat field, the tower, and the location of the receiver on the tower. As will be shown below, there are significant dissimilarities in this respect between the SRE and its commercial counterpart, resulting in a more unfavorable flux distribution inside the SRE cavity. This is believed to have resulted in lower efficiencies measured during the tests than indicated by analyses for the commercial receivers. At the design point, the spillage in the case of the SRE is shown to be comparable to that anticipated for the full-scale designs.

We developed a non-dimensionalized heliostat map showing the boundaries of the CRTF as "viewed" from the various test levels of the CRTF tower (36.6m, 42.7 m, 48.8 m, and 61.0 m). The map also shows the boundaries of two commercial system fields as "viewed" from the tops of their towers.

The following two conclusions were drawn from the map:

First, by comparing the CRTF boundaries with the commercial boundaries, it could be seen that, for accurate scaling of the heliostat radiation geometry, the 36.6 m (120 ft) or 42.7 m (140 ft) test locations at the CRTF would have been appropriate. However, it was only possible to install the SRE at the 61 m (200 ft) level. This means that the incoming flux was on the average at a smaller incidence angle for the experiment than for the commercial receiver, resulting in a disproportionately larger portion of the incident fluxes falling on non-active surfaces inside the cavity.

Second, the minimum theoretical target aperture size required for the SRE (located at the 61 m level) is 2.75 m square. This compares with the actual aperture size of 2.74 m square. The corresponding values for the molten salt commercial receiver are: 9.15 m required vs. 11.0 m square actual. This indicates that the relative spillage in the SRE is slightly higher than for a commercial receiver. Minimizing spillage was not, however, a major consideration in the SRE design.

C. PRE-TEST ANALYSES

Before discussing the analyses, it is important to define two terms relating to the physical layout of central receivers. A receiver control zone is that portion of a receiver associated with a single fluid inlet and single fluid outlet. A receiver with two control zones would have two distinct outlets and two control systems regulating the temperatures of each outlet stream. Fluid passes describes the number of times the fluid flows across the receiver's absorbing surface within a control zone. A single control zone, single pass receiver, for example, is a design having one upper and one lower manifold. The working fluid flows into the lower manifold, which distributes the fluid to a series of parallel tubes. These tubes carry the fluid to the upper manifold and from this manifold to the receiver outlet. For a six-pass receiver, any given fluid particle makes six passes across the receiver's absorbing surface.

The receiver designed for this program is an 18-pass receiver with a single control zone and 16 parallel tubes per pass. Original plans called for the receiver to be tested in three different configurations: fully exposed, partially exposed, and cavity. In the fully exposed configuration, the entire receiver surface is exposed to the solar flux. For the partially exposed configuration, the RTAF (a device for measuring the receiver's input power) is positioned directly in front of the receiver. The aperture of the RTAF is smaller than the receiver's absorbing surface, therefore receiver tubes outside the RTAF aperture are covered with thermal insulation. For this partially exposed configuration, there are eleven active receiver passes. The cavity configuration is similar to the fully exposed arrangement except that a cavity assembly is positioned in front of the receiver tubes with the RTAF in front of the cavity. Only the cavity configuration was tested during the reporting period.

1. Receiver Sizing

It was established early in this program that our molten salt receiver would have a single control zone to minimize the need for receiver outlet temperature regulation hardware and to simplify receiver operation. Incoloy 800 tubing with an outside diameter of 1.9 cm (0.75 in.) was selected as the receiver tubing. It was decided to design the receiver output to be consistent with the CRTF capability of approximately 5 MW. To keep the peak input fluxes below approximately 0.63 MW/m² (200,000 Btu/hr-ft²), the overall receiver size was set at 3.35-m high by 5.49-m long (11 x 18 ft). With these items defined, it was then possible to perform an analysis relating receiver pressure drop and inside convection film coefficient to the number of fluid passes through the receiver. It is important to have as high a film coefficient as practical to limit tube wall temperatures. However, the film coefficient is a strong function of the receiver pressure drop. Based on available pump sizes and a practical compromise between film coefficient and pressure drop, it was decided to design the receiver with 18 fluid passes.

A preliminary evaluation of receiver performance with regard to heat balance, pumping requirements, and tube metal temperatures, was done using a simplified thermal-hydraulic analytical model of the receiver, programmed on an HP 9815A minicomputer.

Typical results of such calculations are depicted in Figure II-2. In this figure the maximum tube metal temperature in each flow pass is plotted against the corresponding salt temperatures at those locations for maximum load conditions in the cavity configuration. The upper curve represents peak local metal temperatures for the cavity configuration, whereas the middle curve depicts the maxima of the external tube metal temperatures averaged over the heat semi-circumference. The peak local temperatures are significant because of the thermal-stress behavior of the tubes. Semi-circumferential averages are used in heat transfer calculations. The maximum internal tube temperatures are also plotted on Figure II-2. These are the peak temperatures of the molten salt in the boundary layer.

Figure II-3 shows the performance map for the cavity configuration. The lower graph shows the calculated temperature of the molten salt exiting the receiver (assuming an inlet temperature of 288°C [550°]) as a function of mass flow rate for different thermal loads (percent of available incident energy). Note that at the 25% level, the receiver cannot be operated at the design point exit temperature without entering the shaded area which represents the calculated turbulent-to-laminar flow transition region (Reynold's number range of 2000 to 4000). The upper graph shows the calculated pressure loss in the receiver as a function of flow rate.

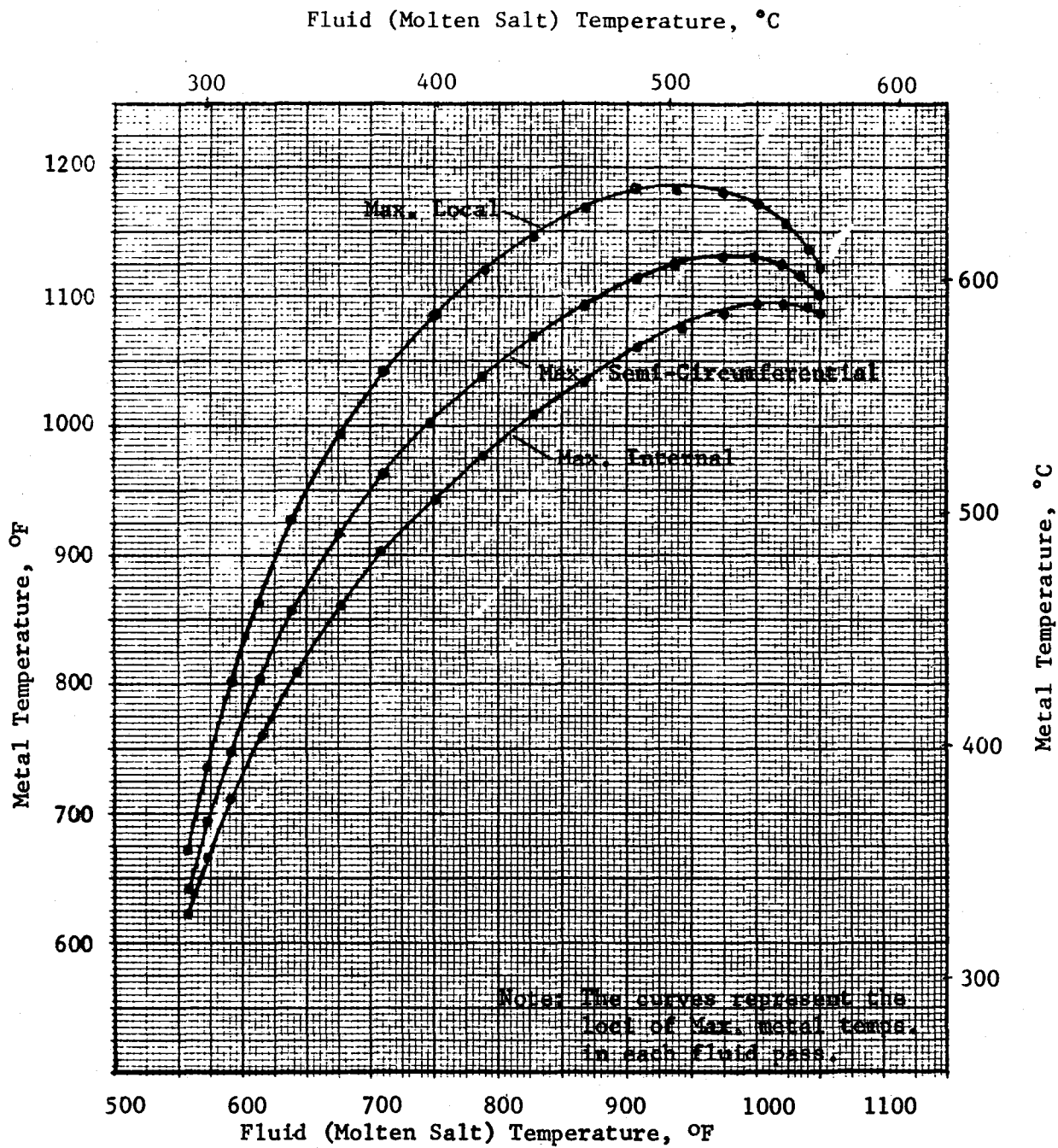


Figure II-2 Tube Metal Temperature Vs Fluid Temperature - Cavity

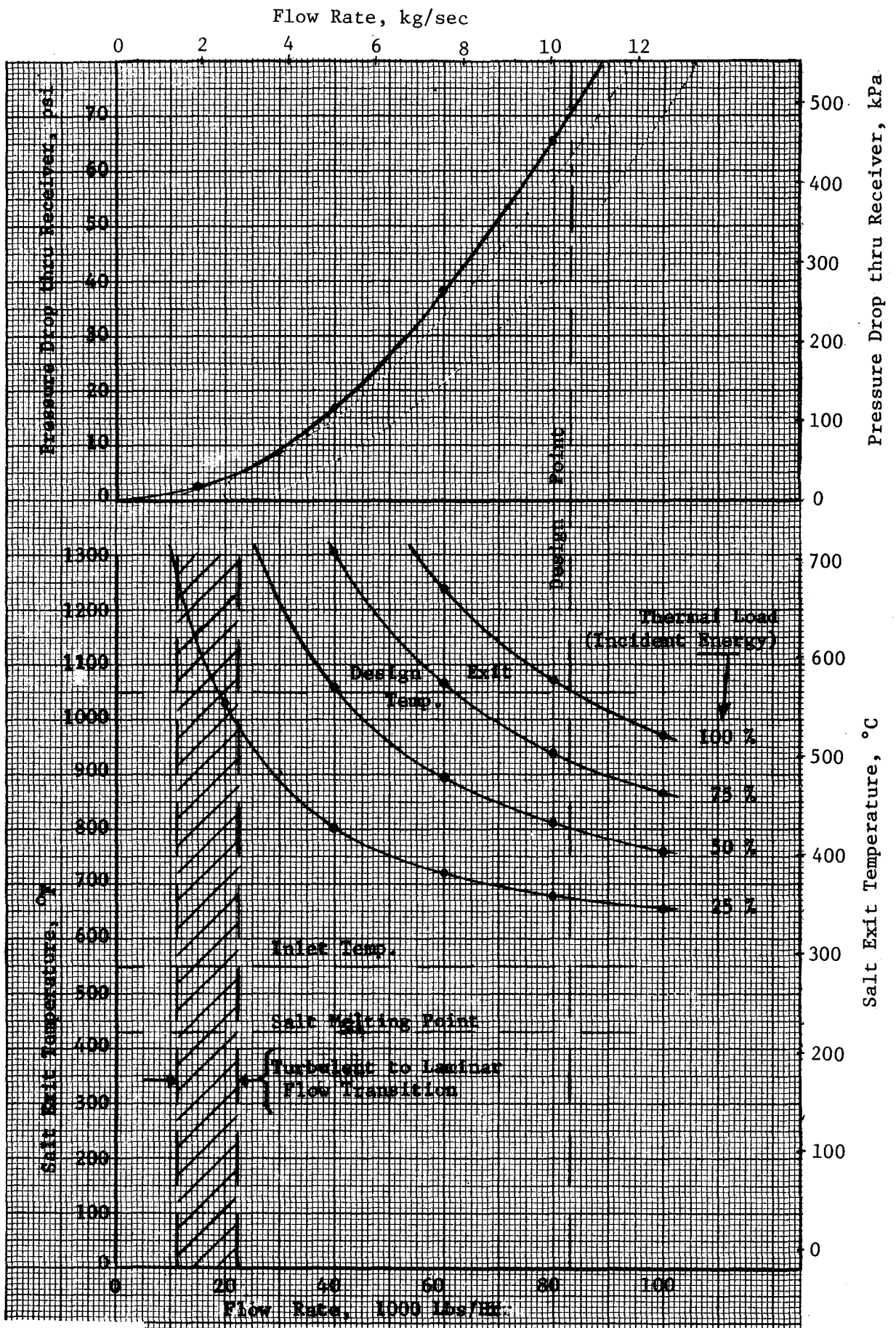


Figure II-3 Performance Map - Cavity Configuration

2. Flux Analyses

The calculation of incident solar fluxes on the receiver surfaces as a function of heliostat field radiation parameters is an important part of receiver design, performance prediction, and operational planning. The analytical tool we used for those calculations is Martin Marietta's Thermal Radiation Analyzer System (TRASYS). This computer program was originally developed to support thermal analysis of space systems but has, in recent years, been expanded to handle heliostat field radiation problems by the addition of a "Mirror Field Library" of subroutines.

The program calculates the incident radiation flux distribution on the target, which may be either of the "exposed" or "cavity" type, the latter being distinguished by the inclusion of an "aperture" node in the definition of target geometry. Comparisons of TRASYS predictions with actual test data indicate that reasonably good match can be achieved--with some exceptions--by proper adjustments of the beam-defining constants in the program.

The flux analyses were divided into four categories: (1) analyses in support of receiver design; (2) the determination of heliostat field configurations for various test operational modes with the given receiver designs; (3) correlation of flux levels at calorimeter locations (RTAF and receiver calorimeters) with those in the aperture plane and on the active surfaces of the receiver; and (4) studies related to partial coverage of the heliostat field by cloud shadows. These are discussed briefly below.

a. Receiver design - Flux analyses in support of commercial-scale power plant designs are normally aimed at optimizing both the radiation geometry of the heliostat field and its interaction with the active (absorbing) surfaces of the receiver. The latter may include such considerations as minimizing spillage, and maintaining local peaks of incident fluxes at acceptable levels. In the case of the SRE, field optimization is obviously not a consideration, and due to configurational constraints mentioned earlier, no attempt was made to minimize spillage or to optimize the geometrical configuration of the cavity. Rather, the design was aimed at providing similarity to full-scale applications at a localized level via absorbed flux levels, Reynolds numbers, heat transfer coefficients, flow velocities, and tube metal temperatures that are representative of proposed commercial-scale receivers.

The receiver panel and cavity flux maps for maximum thermal load-- or "design"--conditions (day 180 at solar noon) for the cavity configuration may be found in Volume II of this report. The predicted peak flux level for the cavity configuration was 0.639 MW/m^2 (203,000 But/hr-ft). Approximately 13% of the energy entering through the aperture was incident on non-active surfaces of the cavity.

b. Partial load studies - The objective of these analyses was to define heliostat configurations for performance tests at partial loads, and for receiver warm-up prior to filling the tubes with molten salt. In establishing these heliostat configurations an attempt was made to maintain a degree of similarity between the partial-load and full-load flux distributions.

Again, the TRASYS program was used to obtain flux distributions for 75%, 50%, and 25% loads, and for heliostat configurations used during warm-up. The criteria used for determining these heliostat patterns was to maintain the radiation equilibrium temperature of the tube wall between 288°C and 593°C (550°F and 1100°F) without salt flow. Since the number and location of heliostats required to achieve this depends on the intensity of insolation, the time of the day, and the test configuration of the receiver, a number of "warm-up modes" (labeled A, B, C, ... etc) were established to suit each anticipated situation.

c. Flux gage correlations - A series of TRASYS models of the RTAF and the cavity aperture were constructed to obtain information needed to develop a transfer function that would allow determination of radiant fluxes passing through the aperture from those measured at the RTAF plane.

To account for various cloud shadowing situations, the heliostat field was divided into ten regions, and a partial transfer function determined for each. The summation of the individual contributions from these regions yielded an overall transfer function for the field.

Due to changes in the relative positions of the RTAF and cavity aperture during installation, a new transfer function was calculated by the HELIOS program, as discussed in connection with receiver efficiency determinations (Section IV-D of Volume II).

d. Partial cloud cover - In order to provide checkout data for the control algorithm for computer control of the receiver, several cloud passage situations were simulated by TRASYS models. For these analyses, the heliostat field was divided into four regions, and the receiver tube wall into six nodes. The field was analyzed twice: once divided vertically simulating east-to-west (or west-to-east) cloud passage, and one horizontally, simulating north-to-south (or south-to-north) passage. The incident flux on each of the six nodes was calculated for four progressive fractions of cloud cover (25%, 50%, 75%, and 100%) and the results used to determine the algorithm's response to the decreases in solar flux.

3. Detailed Receiver Analysis

Areas of detailed analysis of the receiver included receiver tube warm-up with the hot air system, thermal analysis of welded tubes, salt cool-down transients, receiver tube temperature after sudden flow stoppage, the calorimeter cooling system, and two-dimensional tube temperatures. A brief description of these analyses' results are included here.

a. Receiver tube warmup with hot air - Heating up the receiver during checkout tests with heated compressed air was analyzed. Trace heaters are used on every piece of hardware except for the receiver tubes and the air cooler tube bundle. A thermal model was developed to simulate heat loss from the front of the receiver tube using MITAS (the Martin Marietta Integrated Thermal Analyzer System, a generalized thermal modeling computer program).

Results of the model indicate that the receiver would reach operating conditions in approximately 1 hour in the fully-insulated mode and 25 minutes in the partially-insulated mode (Albuquerque test with RTAF in place). (The warmup takes longer when fully-insulated because the mass of the insulation must be heated as well as that of the receiver tubes.)

b. Thermal analysis of tube-to-tube welds - The weld joints on the receiver tubes were also analyzed using the MITAS thermal analyzer program. Worst-case results were achieved at that point of the receiver with the worst combination of fluid temperature [504°C (940°F)] and solar flux [0.536 MW/m² (170,000 Btu/hr-ft²)]. Two additional parametric studies were performed, one at maximum solar flux, and another at a lower flux, but a higher fluid temperature. Results of the analysis indicated there would be no problems with the welds as designed because the maximum temperature in the worst-case situation was 638°C (1180°F).

c. Salt cooldown transients - Worst-case cooldown transients for salt-filled receiver tubes without flow were calculated using a small thermal model programmed on the HP 9815A minicomputer for the following cases: (1) exposed receiver; (2) cavity receiver with the door open; and (3) cavity receiver with the door closed one minute after loss of insolation. The tube metal and the salt were assumed to be a 288°C (550°F) at the beginning of the cooldown transient. In the case of the cavity, that location on the tube wall having the largest view factor to the aperture opening was selected for analysis. Results are shown in Figure II-4.

d. Sudden flow stoppage analysis - Analysis was performed using MITAS to determine the maximum receiver tube wall temperature achieved after a sudden flow stoppage. A conservative assumption made was that the solar flux was constant at 0.694 MW/m² (220,000 Btu/hr-ft²) for 5 seconds then instantaneously reduced to zero for the remainder of the transient analysis.

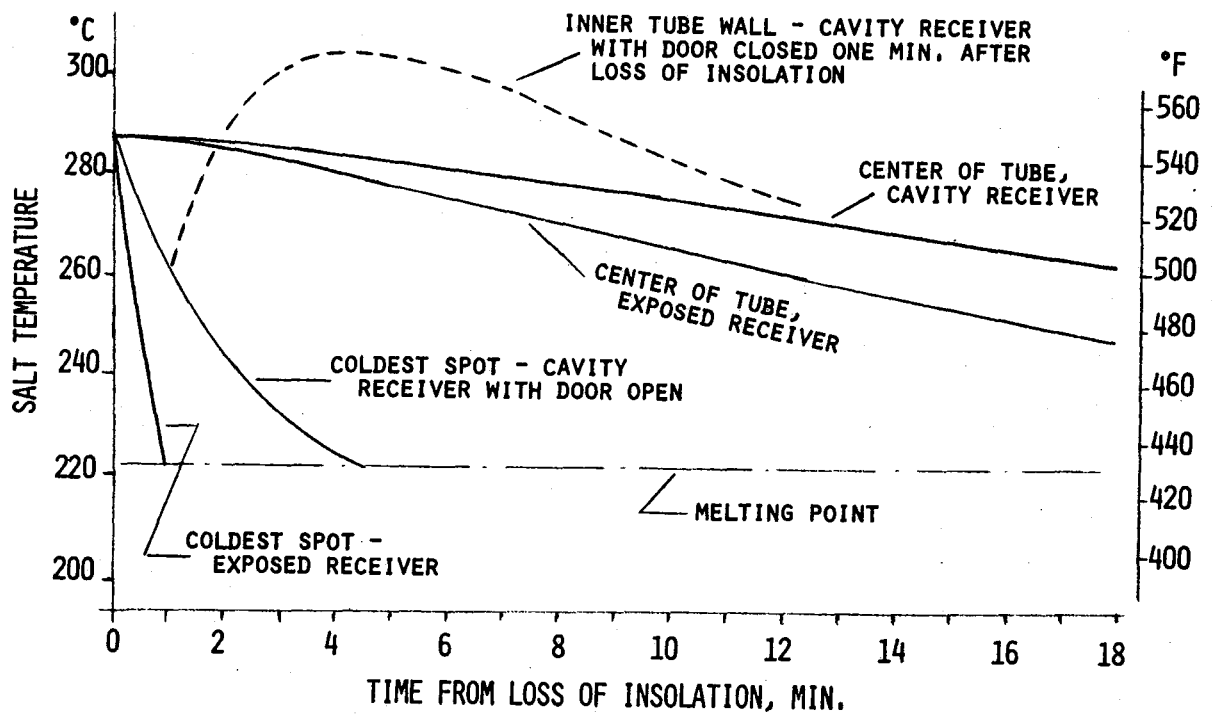


Figure II-4 Receiver Salt Cooldown Transients

e. Receiver calorimeter cooling system - Results of the analysis were used to size the ethylene-glycol chiller and the cooling lines from the chiller to the 18 calorimeters on the receiver surface.

f. Two-dimensional steady-state tube thermal model - To support the receiver tube creep/fatigue studies, a two-dimensional, steady-state thermal model of the tube was developed. The network contains 86 nodes and 165 conductors, and the thermal conductivity of the tube material was varied as a function of temperature. This analysis was carried out using MITAS and 41 different scenarios were analyzed.

4. Air Cooler Thermal Analysis

The thermal analysis used to size the air cooler was performed on a Texas Instruments TI-59 programmable calculator. Two programs were developed for this analysis: the first determined the overall thermal conductance between the molten salt and the air, and the second computed the molten salt and air temperatures throughout the air cooler. Overall thermal conductance calculations were based on a method provided by the finned tube manufacturer (ESCOA) and these were based on empirical correlations.

5. System Drain Time Analysis (Purge Gas Assist Method)

The piping, receiver, and cooler are drained to the sump to prevent salt from freezing in them during shutdown periods. The draining may be accomplished by applying air pressure to the high points of the system. We performed an analysis on the hydraulics of draining the receiver and cooler, assuming a constant pressure of 345 kPa (50 psig) at the receiver drain lines. (We discovered later, during the salt flow checkout tests on the SRE, that a purge-assisted drain was not necessary.)

6. System Transient Response Analytical Model

To gain an understanding of the receiver system transient behavior and to develop the control strategy for the receiver and air cooler outlet temperatures, a thermal model of the system was developed using the MITAS program.

All system components are modeled, including the receiver, air cooler, pump, sump, and interconnecting piping. The program checks at each time step to determine if the flow is laminar or turbulent. It then applies the forced convection film coefficient consistent with the flow regime. Radiation losses from the receiver consist of emission and reflection and the model is constructed so that sensitivity studies can be readily conducted relative to the influence of surface emissivity and absorptivity on these losses.

We conducted case studies using the model to simulate six different operating scenarios for the SRE. They are:

Start-up under automatic control - Simulates a ramp-up from 30% to 100% maximum solar power with the receiver flow rate cooler air flow under automatic control. It assumes that the system was at steady state at time = 0.

Two-, four-, and six-minute clouds - Simulates the passage of a cloud moving at 8.9 m/s (20 mph) over the heliostat field with the SRE operating on automatic. The cloud takes one minute to completely cover the field and one minute to move off. Figure II-5 shows the inlet and outlet temperatures of both the receiver and cooler, the solar flux input to the receiver, the receiver salt flow rate, and the cooler air flow rate for a four-minute cloud passage. This figure is typical of the outputs from all of the MITAS simulations, which were used to develop control strategies for the SRE.

Loss of heliostats - Simulates sudden loss of heliostats (a "scram") after operating at steady-state conditions under automatic control for five minutes. The system remains under automatic control after the loss of flux.

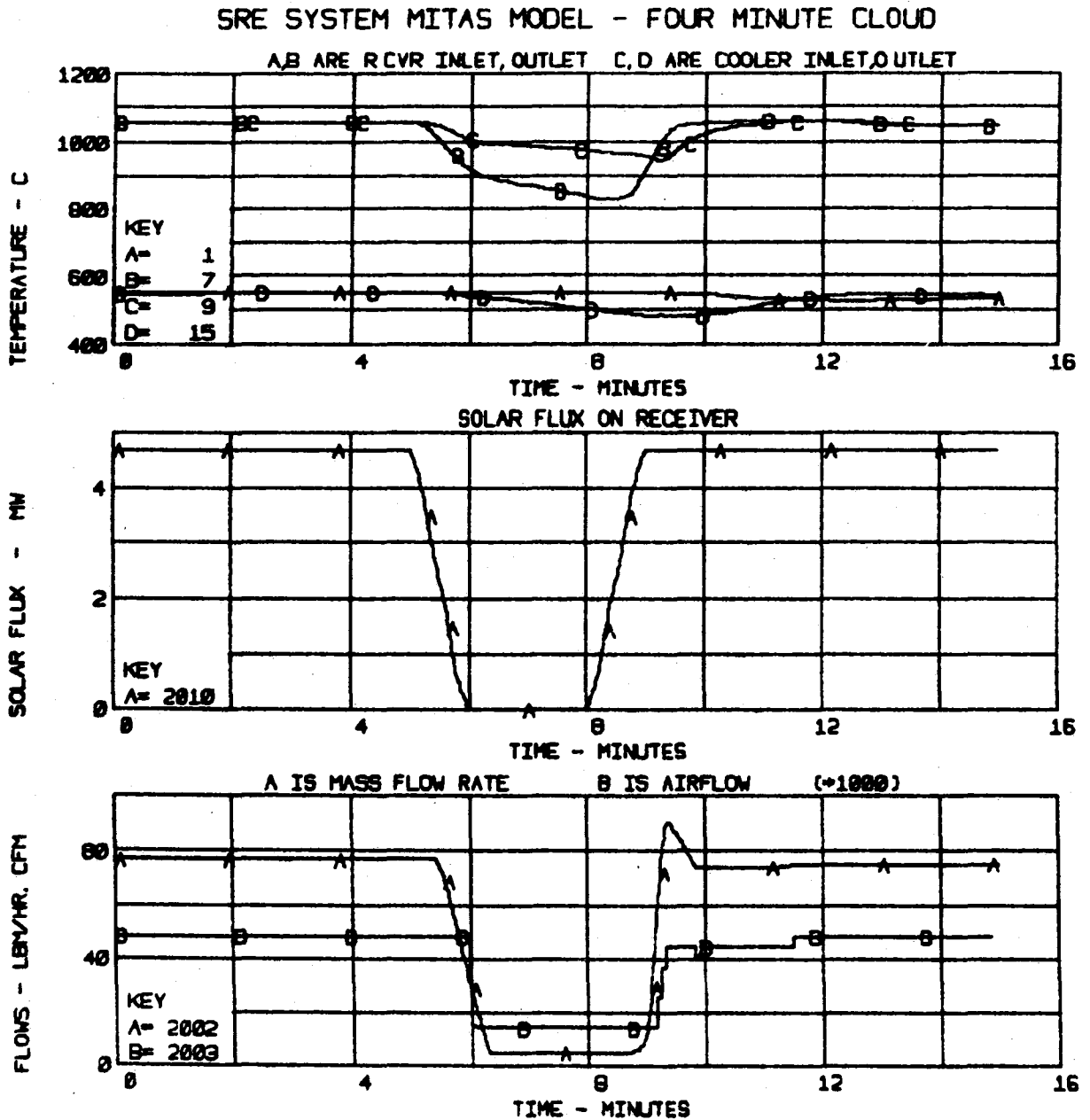


Figure II-5 SRE Transient Response - Four Minute Cloud

Cooler freeze-up - Simulates a "loss of heliostats" under manual (operator) control, where salt flow is stopped but air flow across the cooler continues. (This is a "worst-case" simulation.) This simulation indicates that salt starts freezing in the cooler approximately two minutes after power is lost and salt flow stops.

Control valve closing - Simulates closing of flow control valve during maximum power (this takes about 8 seconds), after which the heliostats are scrambled and cooler air flow is reduced to the minimum. This condition causes a rapid rise in receiver temperature during the sudden flow stoppage [to about 816°C (1500°F)].

Laminar flow conditions - Simulates low insulation condition with SRE under automatic control, where flow rate is decreased to below 2.52 kg/s (20,000 lbm/hr). In the simulation, this elicits laminar flow and yields a very low heat transfer coefficient between the tubes and the salt, which could overheat the tubes. (Note: This simulation assumed a transition Reynolds number of 6000. We did not find a transition to laminar during actual receiver operation even at flow rates resulting in much lower Reynolds numbers.)

7. Additional Thermal/Hydraulic Analyses

Additional analyses that have been performed in support of the receiver SRE are listed below.

- 1) Heat tracing thermal analysis,
- 2) Auxiliary purge air requirements,
- 3) Auxiliary control air requirements,
- 4) Purge air and receiver tube air heating system pressure drops,
- 5) Transient insulation heating due to heliostat "scram",
- 6) System insulation selection, and
- 7) Calibration pot requirements.

8. Stress Analyses

The structural analyses done to support the receiver SRE design include high temperature thermal stress analysis and creep-fatigue damage analyses of the receiver tubes; and the evaluation of the receiver and cavity support structures for critical wind loads of 44.7 m/s (147 ft/s) and seismic loads of 1.5 g's, applied to total weight. The design was checked against ASME Section I design requirements.

a. Creep-fatigue - The design guidelines for creep-fatigue damage on the tubes are based on the ASME Boiler Code, code Case 1592. The thermal stress analysis of the tubes was performed using the finite-element computer program NASTRAN, which uses the temperature distributions around the tube to determine the thermal stresses at each point. (The analysis did not consider the tube-to-tube weld joint, as it was located at a lower-than-maximum tube temperature and much closer to the neutral bending axis. However, this needs to be examined further in the future.)

Very little information is available on Incoloy 800. Although Incoloy 800 is an acceptable material, the boiler code does not list creep and fatigue data for the alloy. The code does, however, show rupture life (Td) and allowable cycles (Nd) graphs for Incoloy 800H. Since the material properties are nearly the same for 800 and 800H at 593°C (1100°F)*, the creep-fatigue data for 800H was used. This was justified by using the curves for slightly higher temperatures than the tubes are actually seeing, thus yielding conservative results.

The stress analysis showed the tubes to be good for two and one-half cycles per day, ten hours per day, for 30 years; or a total of 27,275 cycles and 209,500 hours of operation.

b. Receiver panel and cavity support structures - The receiver and cavity structures were designed according to Sections I and VIII, Division 2, of the ASME Boiler Code. Loading conditions applied to the receiver structure were:

- 1) Wind load - 44.7 m/s (147 ft/s), and
- 2) Seismic load - 1.5 g's applied to total weight.

The appropriate calculations were performed and documented to satisfy the requirements established by the code. A summary list of the calculations which were completed are listed as follows:

- 1) NASTRAN results and calculated wind effects
- 2) Temperature distribution (pass 12 and 13)
- 3) Earthquake (1.5 g lateral acceleration)
- 4) Wind [44.7 m/s (147 ft/s)]
- 5) Combined wind and flux analysis
- 6) Stress analysis on end plates and headers
- 7) Weight and pressure stress (connection of tubes to headers)
- 8) Longitudinal tube expansion (lower header constraint)
- 9) Forces due to lower header constraints (resulting moments)
- 10) Force necessary to align tubes in passes 12 and 13 after flux
- 11) Total moments and deflections
- 12) Upper header supports (stress due to transverse expansion)
- 13) Upper supports
- 14) Hoop bending stress on headers
- 15) Creep-fatigue analysis
- 16) Drain pipe analysis
- 17) Purge pipe analysis
- 18) Welds of tubes to header
- 19) Effects of bends in tubes near headers
- 20) Inlet and outlet reactions
- 21) Butt welds on tubes

The receiver panel was fabricated in accordance with Section I of the ASME Boiler Code.

* This was the temperature of the stress-critical point on the receiver tube.

Thermal stress due to solar flux was analyzed for each individual tube of the receiver. Additional stress due to internal pressure and wind loads was calculated and combined with the thermal stress.

9. Piping Analyses

The interconnecting piping of the SRE was analyzed by Badger Energy, Inc. (Cambridge) to determine the optimum piping layout between components. They performed a pipe stress analysis using standard computer programs established in compliance with the American National Standard Institute (ANSI) Power Piping Code, Section B31.1. The output data from this analysis gives the forces, moments, and pipe stresses at selected points in the piping.

D. SUPPORTING DOCUMENTS

1. Test Plan

Prior to the buildup and testing of the receiver SRE, Martin Marietta developed a detailed test plan describing each of the tests to be conducted during the test program at CRTF. This effort was coordinated with and continually reviewed by Sandia personnel.

We wrote the test plan keeping in mind that the overall objective of this program is to demonstrate the safe, reliable, and efficient operation of a molten salt solar receiver under real steady state and transient conditions. Tests were added to the program as we better understood the problems of solar central receiver operation. Table II-1 shows each of the tests in the test plan and the status of each as of 19 Dec 80. The exposed receiver configuration was deleted from the 1980 test program per agreement with the customer.

The entire test plan may be found in Appendix C of Volume II.

The software requirements addendum to the test plan contains the definitions of the computer algorithms, the sensor calibration curves, CRT displays, heliostat aimpoints, data reduction specifications, and an instrumentation list for the receiver SRE test program. The complete addendum may be found in Appendix B of Volume II.

2. Test Procedures

Martin Marietta wrote separate procedures for each test in the test plan as well as for operations common to all tests (such as start-up, normal shutdown, and emergency shutdown). These step-by-step operating procedures were integrated with the CRTF facility operating procedures and the entire package was reviewed by both CRTF and MMC personnel.

The test procedures were continually updated during build-up and test as operational problems were better understood and system equipment was modified. We believed that carefully written and reviewed procedures are vital to the safety of the operating personnel, test equipment, and facility. An example of these test procedures is in Appendix D of Volume II.

We also identified the possible single point failure modes for the receiver SRE and the potential impact of each failure mode on hardware and personnel safety. This failure mode and effects analysis includes both the receiver hardware and the CRTF support equipment. The analysis identifies the corrective measures to be taken for each failure mode to minimize the probability of that failure. A summary of this analysis is in Appendix E of Volume II.

Table II-1 Test Program Status

1	PC-1	Partial Load - Tower Console Control	Cavity	Complete
2	PC-2	Partial Load - Central Computer Control*	Cavity	Complete*
3	PC-3	Max. Load - Tower Console Control	Cavity	Complete
4	PC-4	Max. Load - Central Computer Control*	Cavity	Complete*
5	PC-5	Max. Load - Tower Console Control	Cavity	Complete
6	PC-6	Max. Load - Central Computer Control*	Cavity	Complete*
7	PC-7	Partial Load with Emergency Shutdown	Cavity	Complete
8	PC-8	Recovery from Simulated Cloud Passage	Cavity	Demonstrated for actual clouds
9	CC	Convection Loss	Cavity	Continuing
10	PFC-1	Efficiency Tests	Cavity	Complete
11	PFC-2	Max. Load for 20 Hours	Cavity	Complete
12	PFC-3	Recovery from Simulated Cloud Passage	Cavity	Demonstrated for actual clouds
16	SE-1	Cycle Tests	Cavity	Continuing; 153 as of 19 Dec 80
17	SE-2	Endurance Test	Cavity	Continuing; 96.3 Hrs as of 19 Dec 80
19	SE-4	Lateral Support Shadowing	Cavity	Complete
20	SE-5	High Localized Fluxes	Cavity	Complete
<p>*All tests calling for central computer control require that the cooler be put on algorithm control. This has not been implemented. The receiver is run on algorithm--the cooler is run from the console or by manual computer keyboard control.</p>				

III. DESCRIPTION OF RECEIVER SRE DESIGN AND OPERATION

A. TEST SYSTEM DESCRIPTION

A simplified schematic of the system is shown in Figure III-1. The entire volume of salt for this experiment is contained in a sump which is maintained continuously at 288°C (550°F) by electrical trace heaters. The pump circulates the molten salt through the receiver, which consists of Incoloy 800 tubes arranged in eighteen serpentine passes. As the salt passes through the receiver, the solar flux from the CRTF heliostats is directed onto the tube panel, increasing the salt temperature to 566°C (1050°F). The salt then passes through an air-cooled, finned-tube heat exchanger. This reduces the salt temperature from 566°C (1050°F) to 288°C (550°F) and the salt is returned to the sump.

An artist's concept of the exposed configuration of the test setup as it would be assembled on top of the CRTF tower is shown in Figure III-2. The salt sump is shown to the center right of the elevating module with the vertical cantilevered shaft pump mounted on top. The molten salt is circulated through the interconnecting pipe and enters the receiver in the lower right header. A cutaway view of the receiver header insulation shows the individual header assemblies. The molten salt leaves the receiver at the lower left and flows through the air cooler which is located in back of the elevating module (behind the receiver), protected from any stray solar insolation. The width of the elevating module parallel to the receiver surface is 9.1 m (30 ft) and the depth is 7.6 m (25 ft). The highest point of the receiver is approximately 8.2 m (27 ft) above the elevating module surface.

The cavity configuration of the molten salt solar receiver SRE is shown in Figure III-3. The cavity and support structure assembly is a freestanding unit not attached to the receiver support structure. The assembly in front of the cavity opening includes pneumatically-operated doors, a water-cooled aperture lip, and the Real Time Aperture Flux (RTAF) measuring device supplied by the CRTF. This assembly is supported by a separate lower structure with minimum attachment to the cavity support structure.

1. Detailed System Description

A more detailed system schematic is shown in Figure III-4. This shows a diagram of the receiver SRE as it appears on the control console located in the elevating module. The entire experiment can be controlled and operated from this console. Once the SRE is started and in a steady-state flow condition, the system operation can be transferred to the CRTF main computer system (MCS).

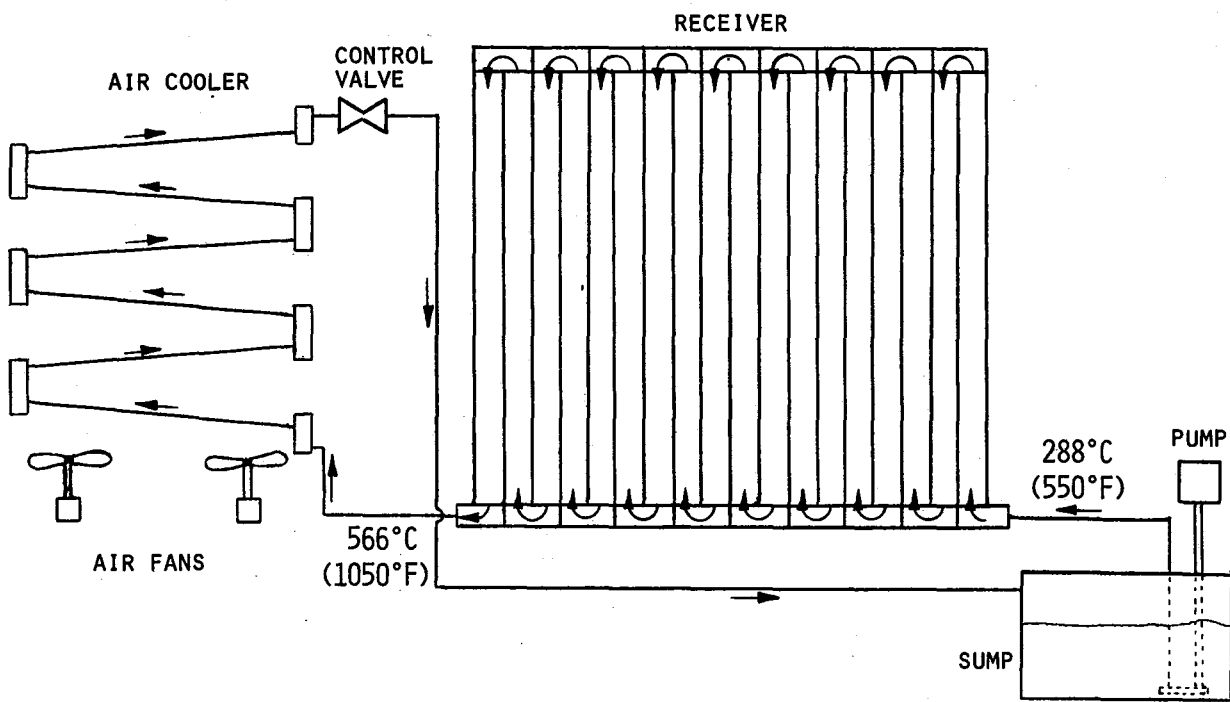


Figure III-1 Simplified Receiver Schematic

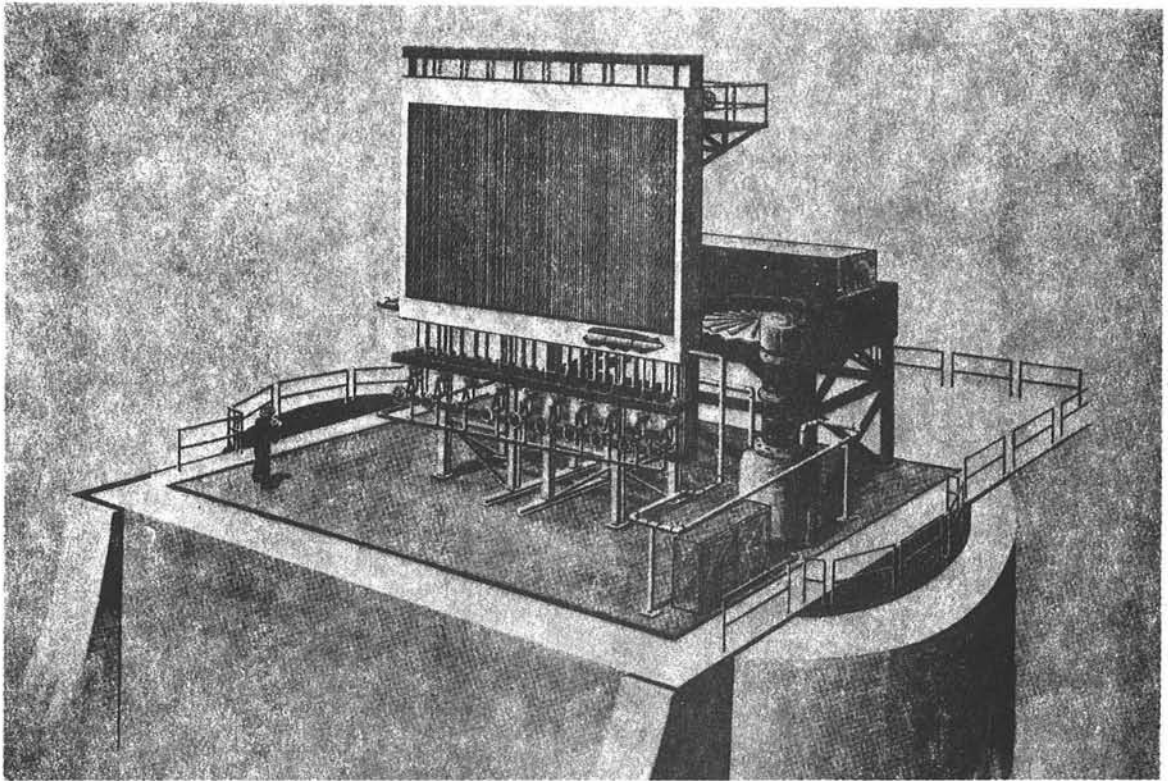


Figure III-2 Artist's Concept of Receiver Exposed Configuration

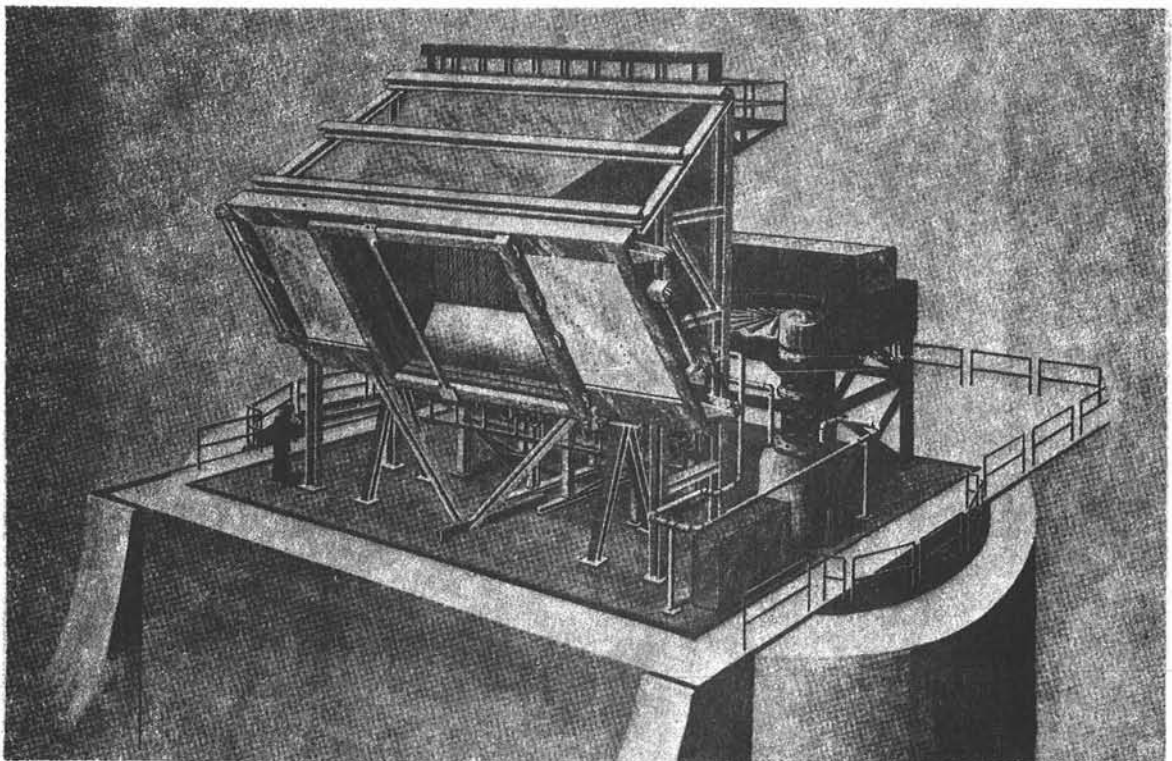


Figure III-3 Artist's Concept of Receiver Cavity Configuration

The sump contains the entire volume of salt when the salt is drained from the system and stored during nonsolar portions of the day. The sump temperature is normalized by thermocouples at various levels on the sump side wall. The pump start and stop switches are located just above the diagram of the sump/pump. The pressure at the outlet of the pump (PT1) is also indicated on the control console. If this pressure drops below a set value, a signal is sent to the annunciator panel shutting the system down.

The line between the sump and the receiver has an insulation valve (IV-1). This valve was installed to isolate the receiver from the rest of the system, to deadhead the pump when necessary, and to provide finer flow control for the SRE. It was locked in the full open position during the test because of the instabilities discovered during pretesting.

During normal SRE operation, the receiver drain valves (DV-1) through (DV-10) as well as the receiver purge valves (PV-1 through PV-9, located above the diagram of the receiver) are closed. This allows the molten salt to flow through the eighteen serpentine flow paths of the receiver to absorb the solar flux. The filling and draining sequence of the SRE will be discussed later.

The salt then flows into the bottom of the air cooler, where two fans force ambient air over the series of finned tubes. The air cooler has a set of louvers between the fans and the finned tubes, which can be opened or closed by the valve positioner on the control console. Movable insulation panels, located on top of the finned-tube bundle, are activated by the on-off switch near the insulation diagram. These insulation panels are used to keep the air cooler warm during initial start-up and during certain emergency situations.

Air cooler fans are controlled by sensing the outlet temperature of the air cooler. A signal is sent from TT6A to the fan controller located in the lower left of the control console. This signal is converted to a control signal that varies the pitch on the fan blades and subsequently adjusts the air flow over the tube bundle. The fan pitch can also be controlled manually.

The flowmeter (FM) is a segmented orifice meter. Its flow measurement is sent to the flow indicator/controller at the top center of the control console. A closed-loop control automatically sets the flow control valve (FCV) to maintain the desired flow rate. The flow indicator/controller also accepts a signal from the fluid temperature thermocouple at the outlet of the receiver (TT5A), which automatically resets the flow rate to maintain the desired outlet temperature. The position of the FCV is indicated on the control console by the valve position indicator.

The calibration pot is downstream of the FCV as a check of the automatic flow meter. When the butterfly valve downstream of the calibration pot (CV-1) is closed, the salt will be retained in the calibration pot, which is suspended on a load cell. This load cell will record the weight of the salt retained for approximately 35 seconds. From a graph of weight vs time, an accurate flow rate can be determined.

The kill button located to the left of the receiver panel sends a signal to the MCS to scram the heliostats off the receiver surface in the event of an anomaly during system operation.

The annunciator panel indicates by flashing lights and a horn six alarm conditions to the operator. These are:

- 1) Low pressure at the outlet of the pump,
- 2) High/low salt temperature at the cooler outlet,
- 3) Low salt flowrate,
- 4) High salt temperature at the receiver outlet,
- 5) High receiver tube temperature, and
- 6) Power off.

Trace heating controls are located on a separate panel. These switches turn the trace heaters on or off remotely. No variable controls are required since the heaters are sized for specific line requirements.

The top "insert" panel on the right side of the control is used to verify signals sent to the MCS for operation by the CRTF computer and also to verify when these same signals are returned to the control console from the MCS.

2. Component-Level Description

a. Receiver - The receiver subassembly, without the support frame, is shown in Figure III-5. It is made of 288 19-mm (0.75-in.) diameter Incoloy tubes arranged in 18 serpentine passes of 16 tubes each. The tubes are welded into headers of 110-mm (4.5-in.) diameter Incoloy 800 tubes. Each tube is welded to the adjacent tubes in nine places by a tungsten inert gas (TIG) welding process to control cracks and open areas between them, and to keep the tubes in a single plane. Figure III-6 is a close-up of the welded receiver tubes.

The receiver header assembly is suspended at the top and allowed to grow downward during solar testing. Vertical and horizontal movement of the receiver during test are measured by linear variable displacement transducers (LVDTs) mounted to the structure.

The receiver tube and header assembly are designed to Section I of the ASME boiler code. Although the code does not specifically outline design parameters for a solar boiler, it does provide basic design and quality control criteria.

b. Main support structure - The main support structure, which supports the receiver as well as much of the interconnecting piping, valves, access ladders, and platforms for the SRE, consists of two welded steel towers which are bolted to the top of the CRTF elevator module. The towers, shown in Figure III-7, were designed to the wind and seismic requirements specified by the CRTF.

c. Air-cooled heat exchanger (air cooler) - The air cooler, shown in Figure III-8, is composed of four major parts: the fan housing, the tube bundle assembly, movable louvers (located under the tube bundle), and movable insulated doors.

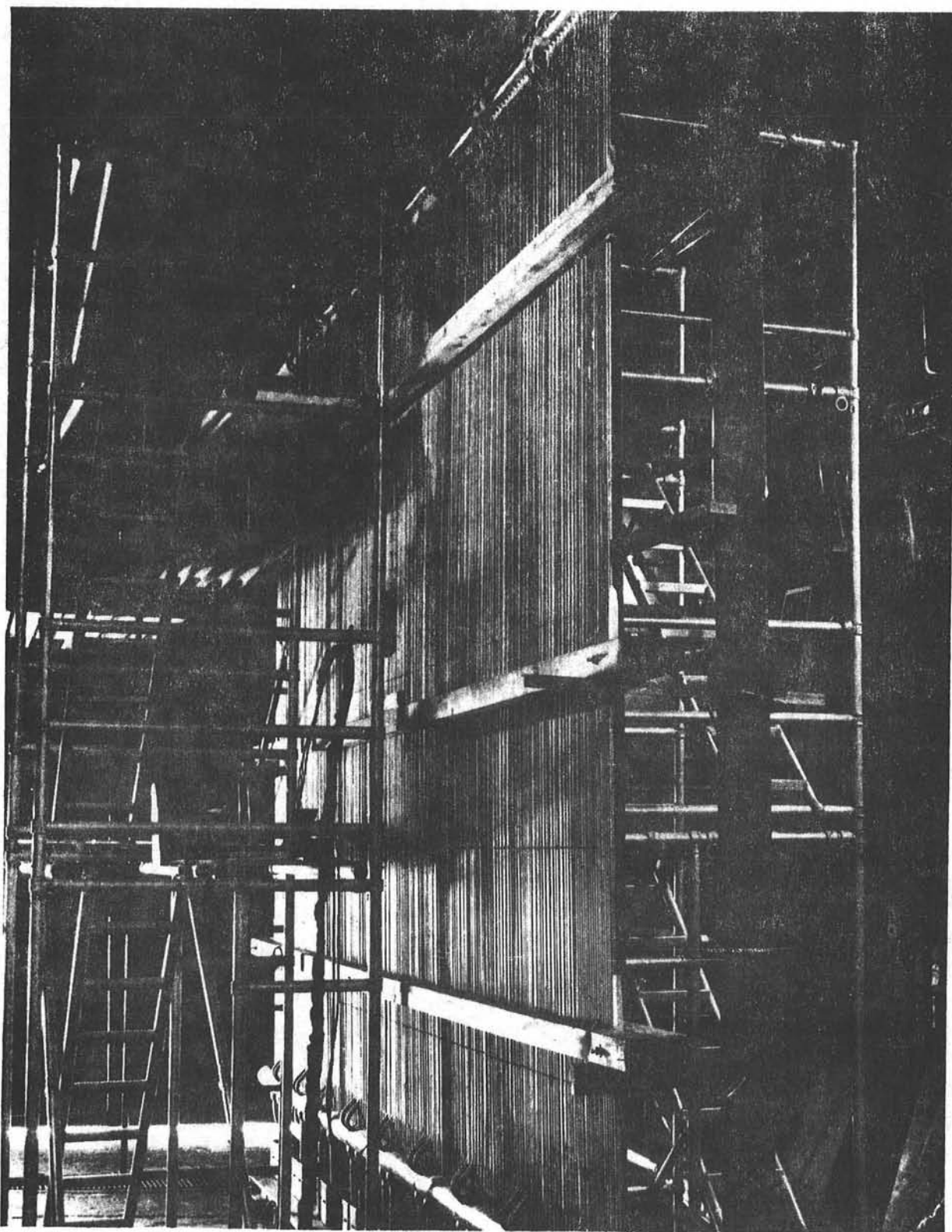


Figure III-5 Receiver Tubes and Headers Subassembly

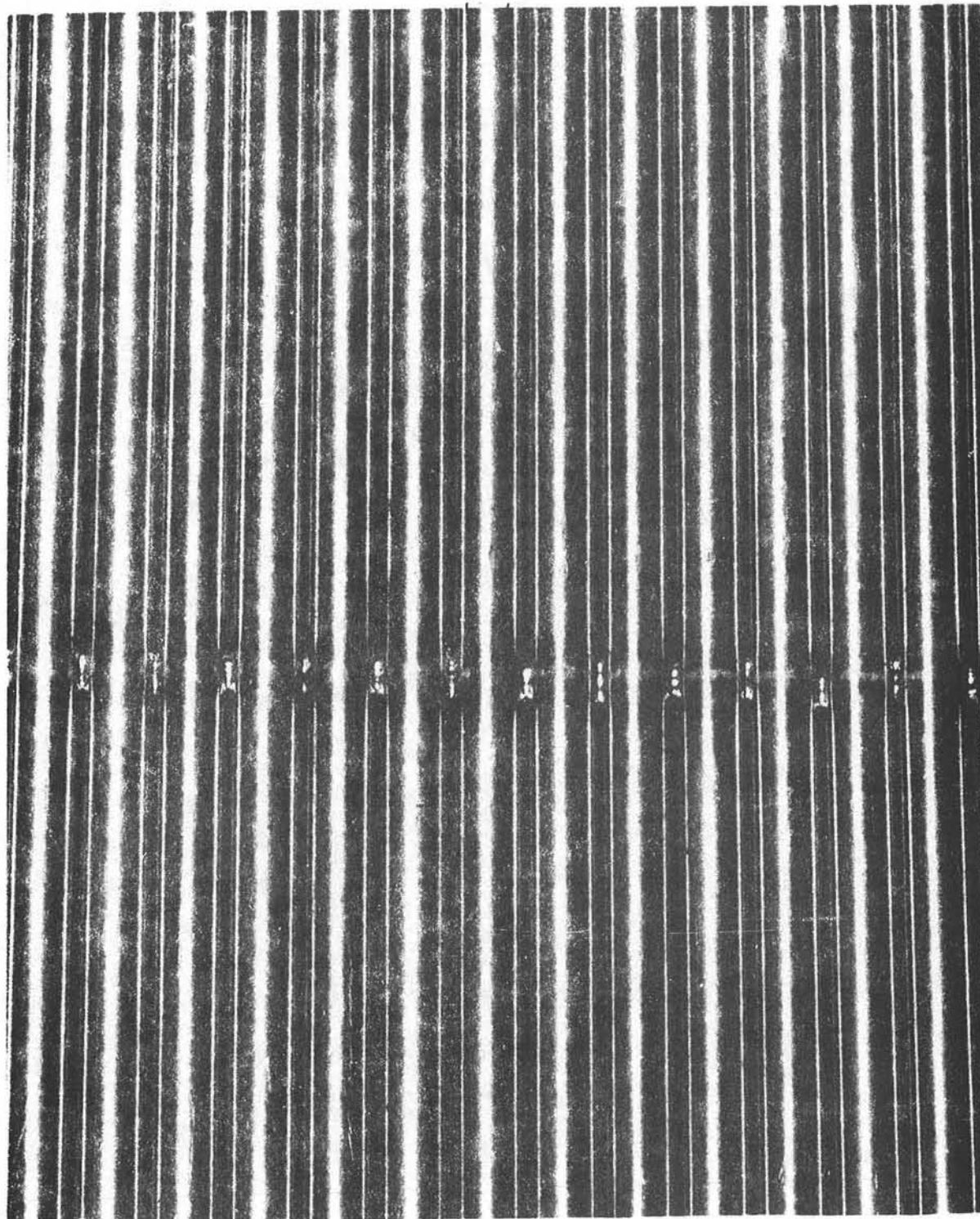


Figure III-6 Close-up of Welded Receiver Tubes

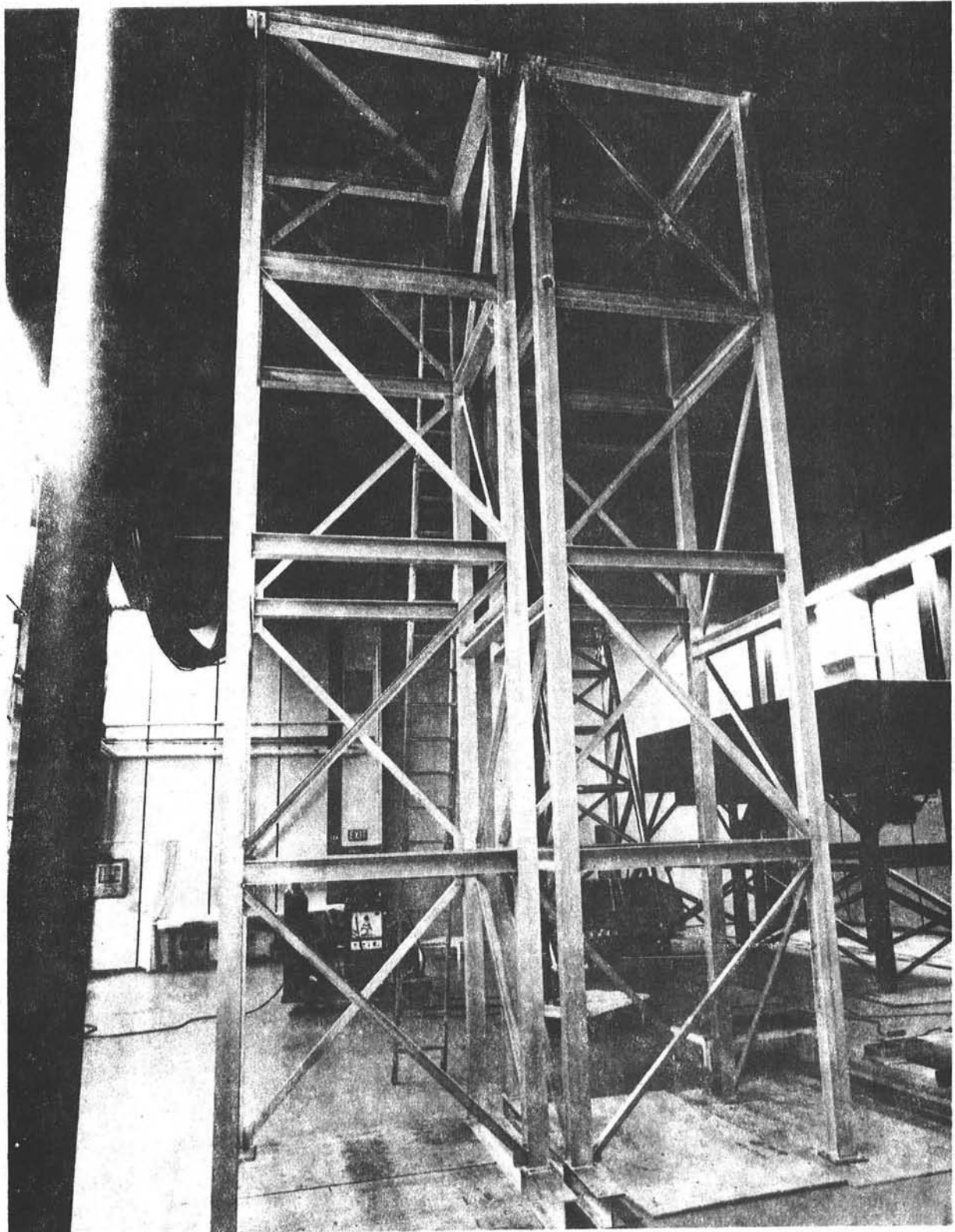


Figure III-7 SRE Main Support Structure

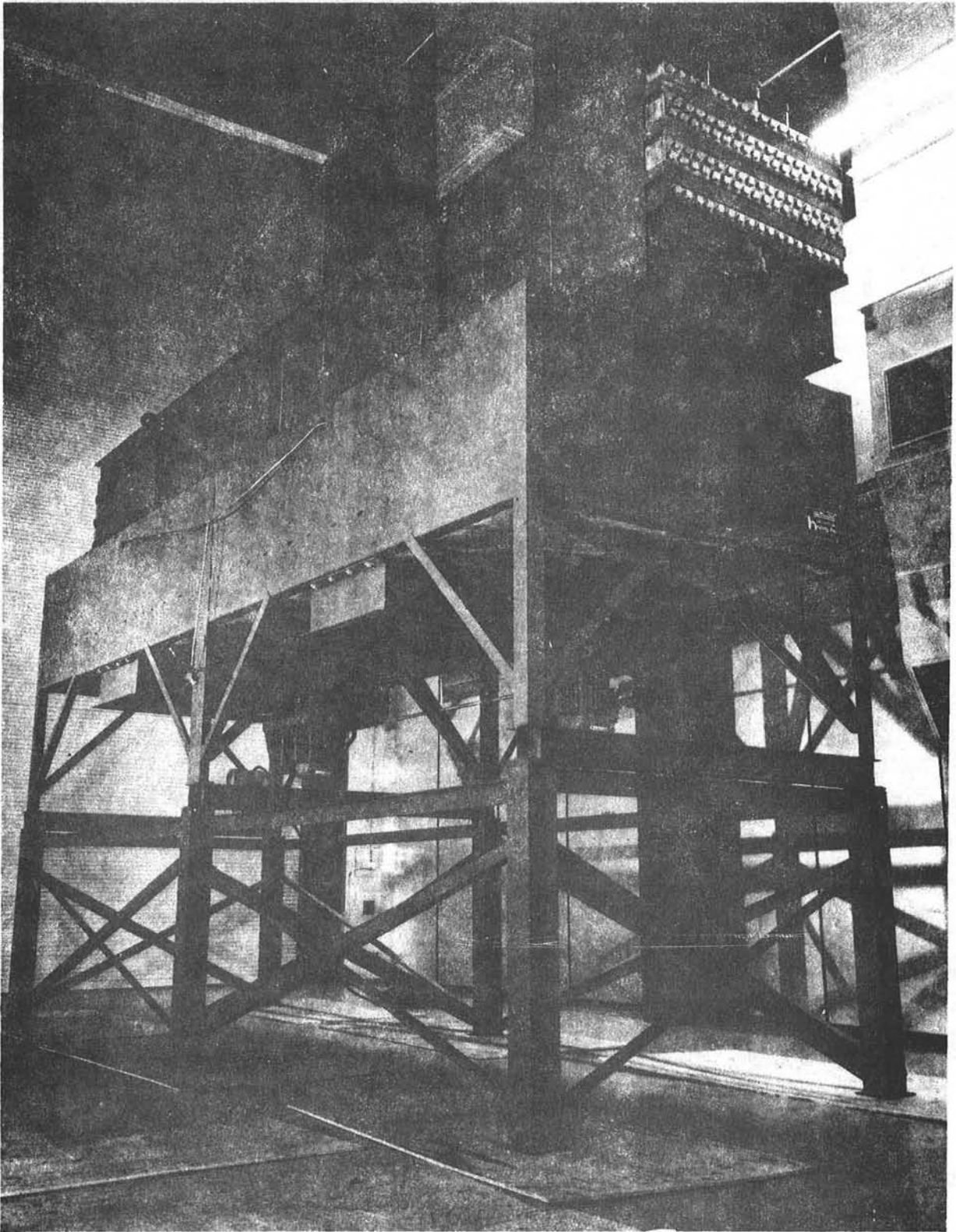


Figure III-8 Air-Cooled Heat Exchanger (Air Cooler)

The tube bundle, which carries molten salt, was designed, fabricated, and certified according to the requirements of Section VIII of the ASME code. Each tube is sloped slightly to aid in gravity-draining the cooler. Controllable louvers, located directly beneath the tube bundle, can be closed to seal the unit during pre-heating, or can be opened to varying degrees during test to regulate the air flow over the tubes. The insulated doors on top of the air cooler tube bundle can be opened or closed as necessary during test and pre-heat. The fan housing contains two fans; their pitches can be controlled remotely from the SRE main control console.

d. Pump/sump assembly - The sump, shown in Figure III-9, is a completely welded assembly of alloy steel. It is not an ASME-coded vessel, but was fabricated by the same processes used for the receiver.

The vertical cantilever pump (also shown in Figure III-9) is similar to the one successfully used in the Phase I contract. The pump is an off-the-shelf item used in the commercial molten salt industry because the pump bearings and seals are not immersed in the molten salt. No new pump development or special user stamps were required for this application.

e. Valves - Salt valves for the system, i.e., PV-1 through PV-9, and DV-1 through DV-10, are all carbon steel body valves with stainless steel internal bellows.

f. Piping - The interconnecting piping for this system was designed in accordance with the ANSI B31.1 Power Piping Code. Because of the extreme wetting characteristics of the molten salt, especially at the higher temperatures, pipe connections were welded to the maximum extent practical.

The piping is heat traced for preheating before molten salt is circulated through the system. The piping is also insulated and wrapped with a sheathing to protect it from the environment.

g. Calibration flowmeter - In addition to the segmented wedge flowmeter, there is a calibration weigh tank designed to improve flow-measuring accuracy. When a flow measurement must be taken, the butterfly valve at the outlet of the calibration tank is closed remotely and molten salt accumulates for about 35 seconds in the tank. The tank is suspended from a load cell and the weight of this device is recorded as it fills with salt. This curve of weight vs time gives an accurate salt flowrate for a portion of the 35-second fill time and can be compared to the reading from the segmented wedge flowmeter. The system can then be drained by opening the butterfly valve and returned to normal flow operation.

h. Cavity assembly - The cavity assembly, shown in the artist's concept in Figure III-3, is a completely independent structure and is not attached to the main support structure. The back of the cavity is open to the full active surface of the receiver and tapers to an opening approximately 2.7 m x 2.7 m (9 ft x 9 ft) in the front.

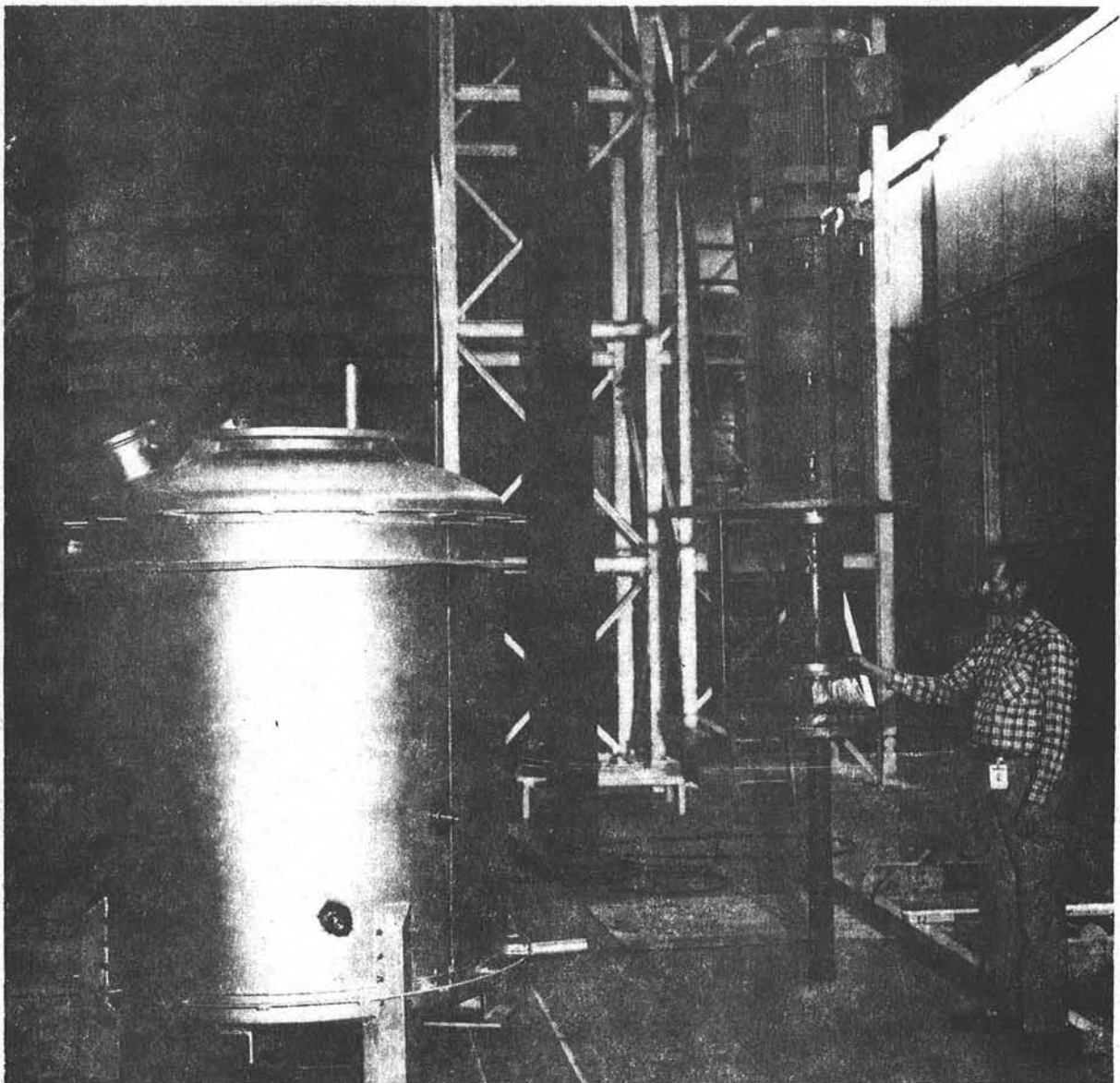


Figure III-9 Molten Salt Sump and Vertical Cantilever Pump

An assembly consisting of two pneumatically-operated doors, a water-cooled aperture, and the RTAF device are located in front of the cavity assembly.

i. Control console - Figure III-4 shows the main control console which was located in the elevator module below the test fixture. All of the primary component controls and readouts are located on this console. Another smaller console held the trace heater controls and secondary temperature readouts.

B. TEST FACILITY

The tests were performed at the Central Receiver Test Facility (CRTF) in Albuquerque, N.M., which is operated by Sandia Laboratories for the U.S. Department of Energy. The facility is described in detail in Reference 1. Only those subsystems and support functions applicable to the SRE tests are outlined below.

1. Heliostat Array Subsystem

The CRTF energy collection field consists of 222 heliostats, of which 207 were used as a maximum during this program, with a predicted maximum power input to the receiver of 5.2 MW. The field was used in its northern distribution configuration, with the first two rows (closest to the tower) excluded because of their unfavorable position with respect to a target located on the top of the tower. The general layout of the heliostat array used during the test is shown on Figure III-10. Each heliostat has 25 individual mirror facets totaling 37.2 m² (400 ft²) of reflective surface per heliostat. The facets are mounted on a structure with azimuth and elevation gimbals to allow aiming the reflected energy at the chosen target.

The heliostat master control system (MCS) sends each heliostat an updated pointing vector once every second, and the gimbal motors respond by re-aiming the heliostat as necessary. The heliostat position signals may be generated by either a programmed sequence or by a facility operator.

2. Real-Time Aperture Flux System (RTAF)

This system measures the flux density near the aperture plane. Circular-foil heat-flux gages are mounted in a water-cooled bar that can be swept through the concentrated beam in front of an experiment.

The gages are mounted in a fixed array on 7.6- to 10.2-cm (3- to 4-in.) spacings. The data that are collected are analyzed by a dedicated computer system and can be used to fine-tune the heliostat beam and provide flux data for the experimenter. The computer also integrates the measurements to give power input to the receiver.

-
1. "Central Receiver Test Facility (CRTF) Experiment Manual" SAND77-1173 (Revised), October 1979.

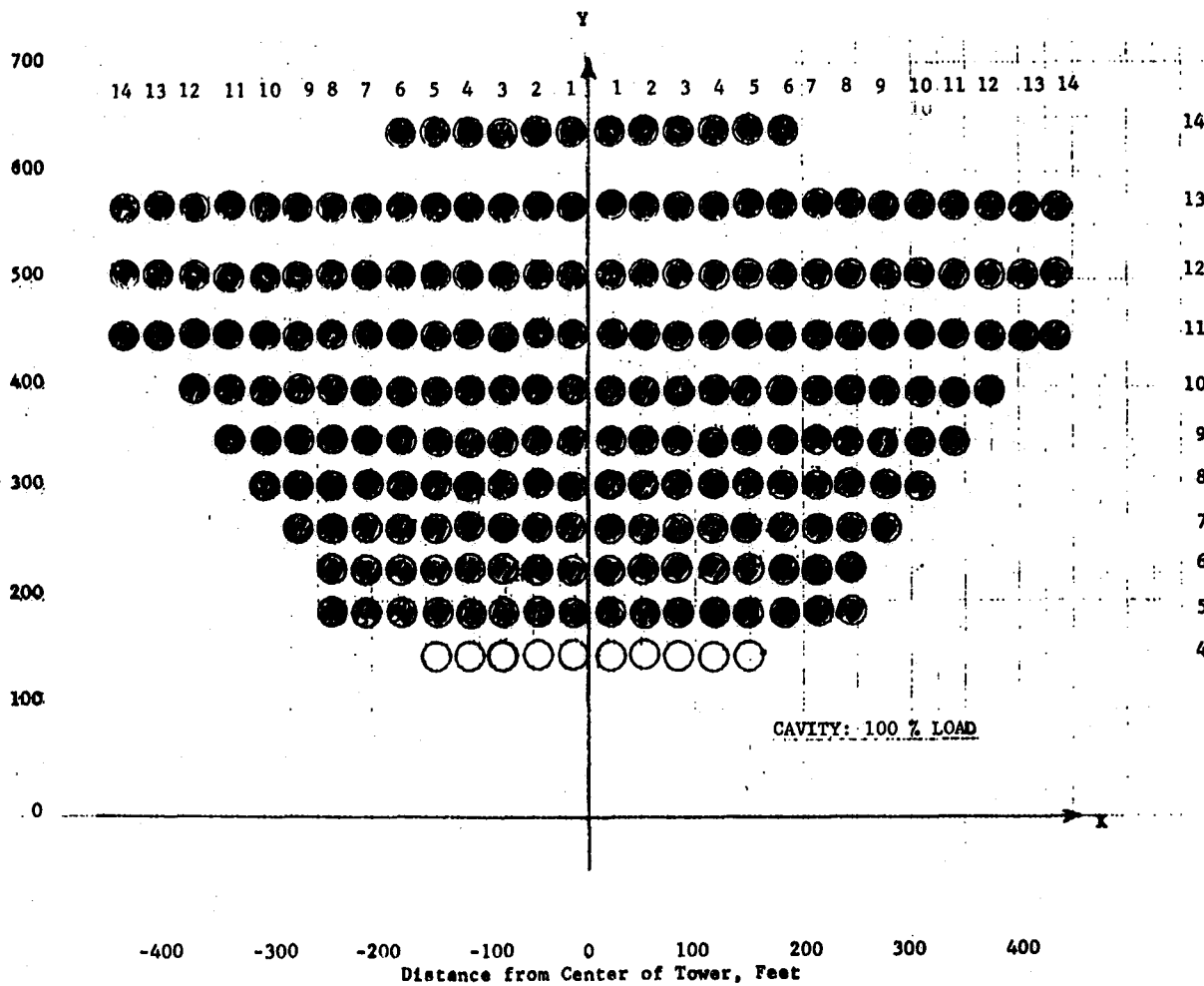


Figure III-10 General Layout of the Heliostat Array

3. Receiver Tower

The CRTF receiver tower rises 61 m (200 ft) above ground and extends 15.2 m (50 ft) below ground. The tower cross section is circular with rectangular projections on the north and south (Figure III-11).

Test bays for experiments are located on platforms at the 36.6-, 42.7-, and 48.8-m (120-, 140-, and 160-ft) levels. Experiments can also be conducted at the top of the tower.

The elevating module is itself an enclosed three-story building in which each story is laid out as a single room. The top room contains instrumentation patch panels, the middle room contains the data acquisition system, and the lower room is a light-machine shop.

4. Control and Data Recording

The Master Control System (MCS) coordinates control of the CRTF operating and data systems. The MCS is an overall command, control, and data system that performs control management and supervision as well as data collection, analysis, and presentation.

5. Backup Systems

Backup systems were provided to allow the receiver system to be shut down safely after failure of the primary electrical or pneumatic systems. Also if the primary heliostat control system failed, there were provisions for defocusing the heliostats off the receiver. Martin Marietta defined the requirements for these systems. The specifics of how these systems were to be switched was coordinated with CRTF and included in the test procedures.

6. Software

The software for the molten salt receiver system is concerned with data that are transmitted to the central control room. Martin Marietta was responsible for defining the software requirements while CRTF was responsible for developing the software itself. The detailed software requirements are defined in Appendix C of Volume II.

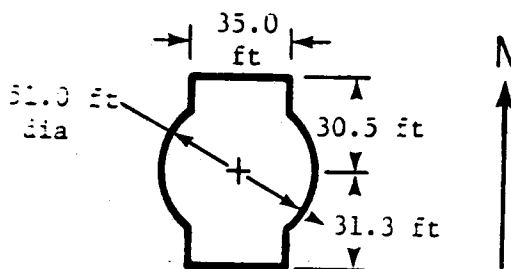


Figure III-11 Tower Cross Section

C. INSTRUMENTATION AND DATA REDUCTION

1. Instrumentation List

The SRE instrumentation is summarized in Table III-1. The multiplexed data were transmitted to the computer control room, where they were recorded on tapes, and/or displayed on CRTs for monitoring purposes. All other data were recorded or displayed in the console control room (in the tower), via data loggers, multipoint recorders, and strip charts.

2. CRT Displays

There were six CRT displays in the computer control room for real time test monitoring purposes, as follows:

Heliostat Control CRT - Located on the heliostat operator's console, this CRT monitored heliostat status, as well as other information such as wind conditions, and tower shadowing.

Basic SRE Parameters - Two CRT's on the SRE operator's console monitored selected performance parameters.

Alarm CRT - Located on the SRE operator's console, this CRT displayed information concerning warnings and alarms, as well as information pertaining to computer keyboard and algorithm control.

Colorgraphic Display - A colorgraphic display of the thermo-hydraulic status of the receiver was available, on command from the computer keyboard, on a separate CRT on the SRE operator's console. The colorgraphs showed valve positions, and salt levels, associated with the basic operational sequences of the SRE (e.g., warmup, fill, establishing flow, recirculation, run at full power, purge, etc), as well as quasi-real time basic data such as flow rate, receiver inlet/exit temperatures and pressures, fan positions, whether the solar fluxes were on or off, etc. An example (in black and white) of a colorgraph showing "run" conditions is depicted on Figure III-12.

Insolation - Digital output from an Eppley pyro-heliometer was displayed on a sixth CRT for monitoring insolation conditions.

3. TV Monitoring

Two close-circuit television cameras, with remote scan and zoom capabilities were used for visual monitoring of the receiver and the heliostat field, respectively. TV screens were installed both in the computer control room, and in the console control room in the tower.

Table III-1 Summary of SRE Instrumentation

<u>Instrumentation</u>	<u>Number</u>	<u>Type</u>
Temperatures		
Fluid	6	Type K T/C in wells
Metal	380	Type K T/C, welded
Flow		
In-Line Continuous	1	Segmented orifice with silicon-filled capillary tubes
In-Line Weight/Flow Check	1	Calibration weigh tank
Pressure	3	Thermally-isolated transmitters with silicone-filled capillaries
Displacement Gages	6	LVDTs (Linear Variable Displacement Transducers)
Solar Flux	19	18 flux gages + RTAF assembly

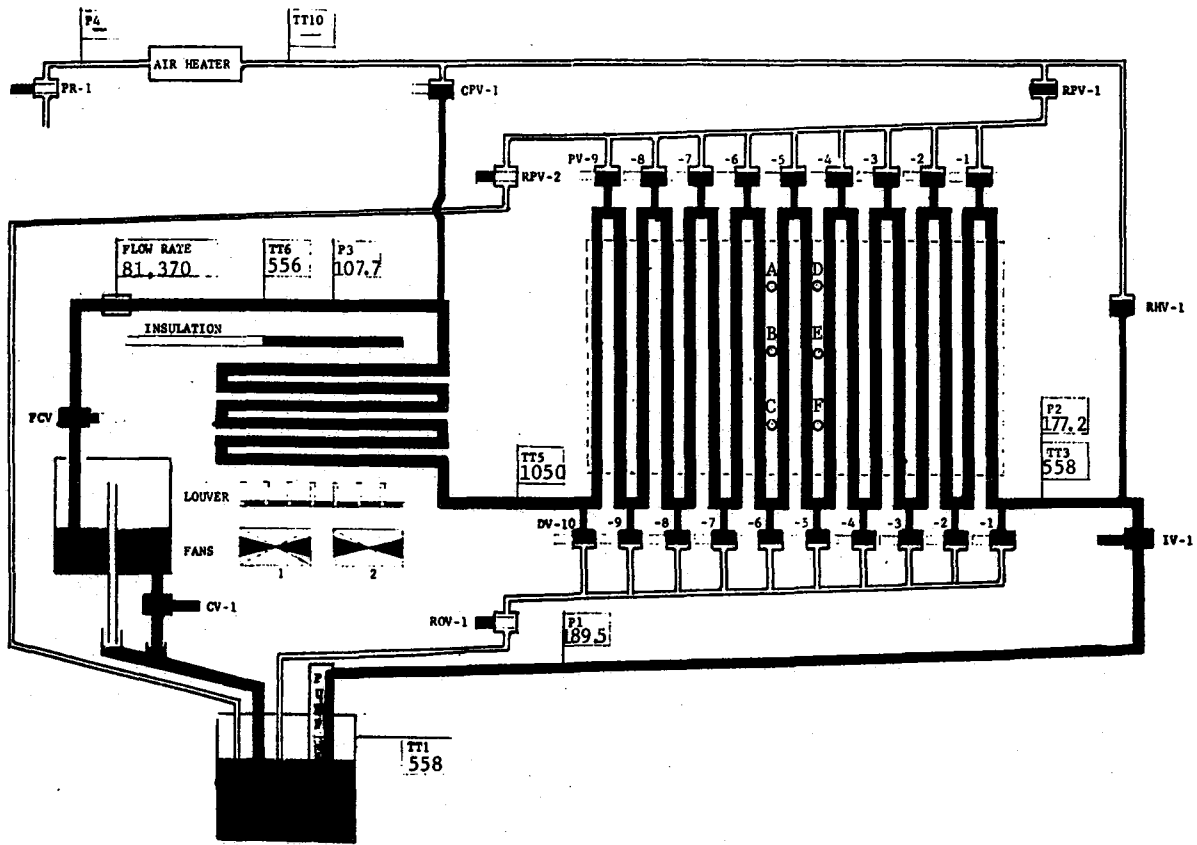


Figure III-12 Typical Colorgraphic CRT Display

4. Data Reduction

Three data tapes were generated for each test on a daily basis. The raw data as obtained through the multiplexer (in mV, V, or mA signals) was recorded on a "raw data file." From this a "floating point tape" was generated, normally during the night following the test. By the use of appropriate computer codes, either a digital printout, or plots, or both, in engineering units, could be obtained from the floating point tape in the morning following the test day. Additionally, a "save file" was generated during each test, from which a digital printout of selected data could be obtained within an hour or so after the termination of the test. The data on the save file was normally recorded at 20-second intervals. This compares with 2-second intervals on the raw and floating point tapes.

Additional data was collected during each test in the console control room from the two data loggers, and from the various strip chart recorders of the SRE.

D. TYPICAL DAILY OPERATION OF THE SRE RECEIVER

1. Clear Day Operation

Figure III-13 is an operational timeline for the receiver SRE during a typical clear day. A "clear day" is one where only a light haze or an occasional swift-moving cloud is encountered, and the system is maintained at "design point" with no trouble. The timeline traces the normal operation of the receiver system through seven phases--pre-warmup, warmup, receiver fill, power ramp-up, design point approach, testing, and shutdown and drain. The approximate time required for each phase is also given. (The timeline assumes no glitches.)

Note that certain operations are peculiar to the test and would not be necessary in commercial solar power systems. These items, primarily during pre-warmup, are also the most time-consuming. The actual time required to warmup the receiver with heliostats, start salt flow, and then ramp-up to and stabilize at design point conditions takes only an hour. Since the entire pre-warmup phase can be completed prior to sunrise, the receiver SRE could be operating at design conditions within an hour after the sun is high enough for the heliostats to preheat the receiver. Because a commercial salt receiver will not require a warmup phase (it will be kept hot through the night), it could be at design conditions within 10 minutes after sunrise.

Three test crew operators are required to run the Martin Marietta receiver: two in the tower control room (directly underneath the receiver test set-up) and one in the main computer control room. The tower control crew is responsible for preparing the receiver for daily operation, monitoring the main control console in the tower control room and securing the receiver after shutdown. The operator in the main control room monitors receiver status on several CRTs and operates the receiver when under keyboard control on computer algorithm control. He also interfaces throughout the test with the CRTF crew operating the heliostats.

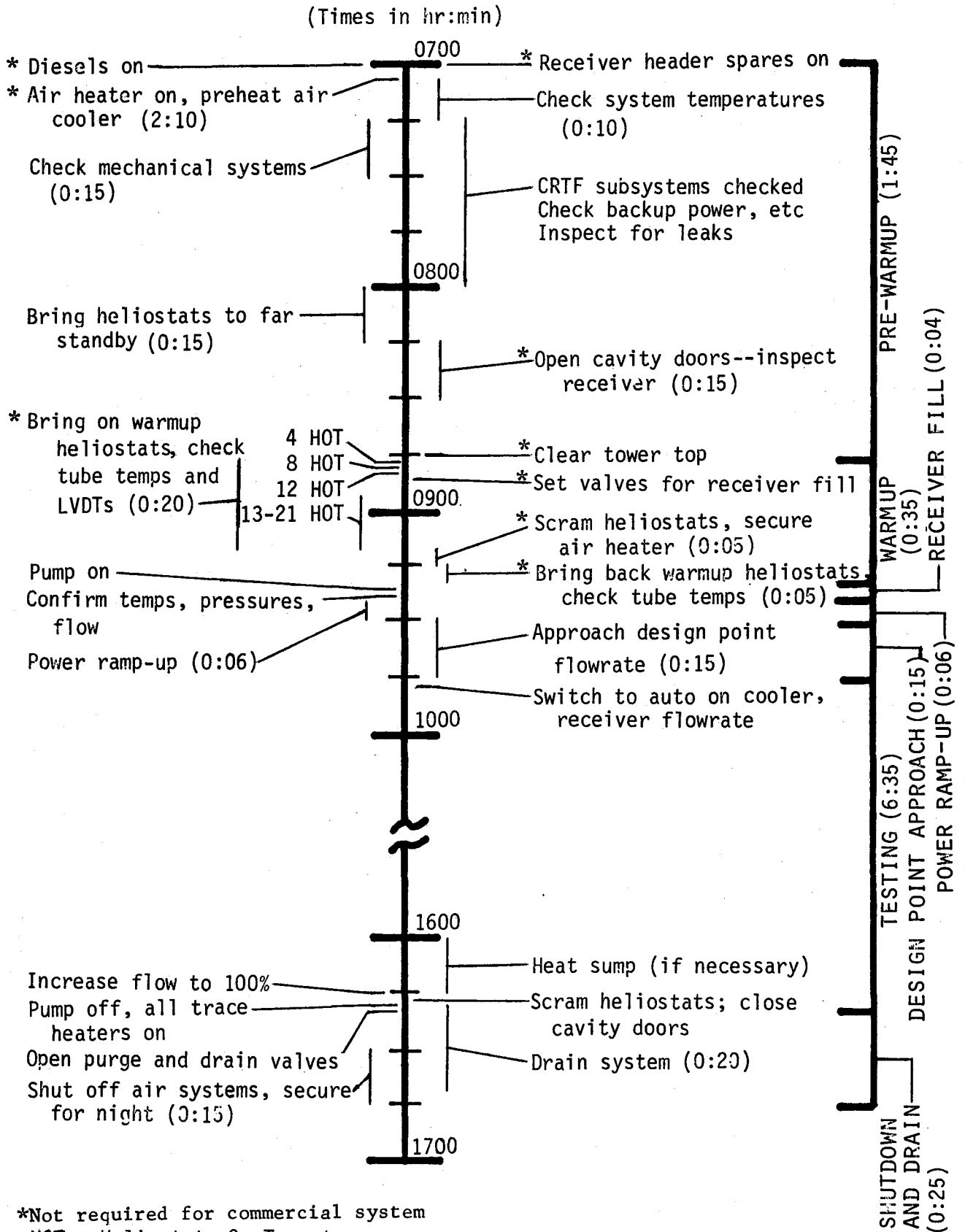


Figure III-13 Typical Clear Day Operational Timeline

2. Receiver Operation on Cloudy Days

The primary goal of the control strategy used during operation of the SRE receiver was to maintain a constant outlet temperature, as long as it did not jeopardize the safety of the receiver. The control strategy that we used and the receiver's response during cloudy day operation depended on the nature of the clouds. From the standpoint of receiver response and control requirements, there were five types of cloudy conditions: heavy haze; an occasional small but fast-moving cloud; continuous passage of sporadic clouds; large slow-moving clouds; and total overcast. There were also combinations of these conditions.

a. Heavy haze - This is usually due to a thick layer of high cirrus clouds, and results in an overall low insolation that changes relatively slowly. The salt flow rate is initially set to maintain the receiver outlet temperature at 566°C (1050°F). The control system (responding to the outlet temperature changes) adjusts the flow rate to keep the outlet temperature constant. Since this is a continuous condition which changes slowly, our analog control system was adequate for controlling to this condition.

b. Occasional small, fast-moving cloud - This is a single small cloud that drops the insolation momentarily. The receiver outlet temperature drops accordingly (but quickly recovers), the loss in temperature is absorbed by the system, and no attempt is made to control to it. Since the time span of the cloud is of the same order as the time it takes the salt to flow through the receiver, and since our control was tuned for slow response, controlling to this condition causes the outlet temperature to overshoot the control set point.

c. Continuous sporadic clouds - The insolation drops from these clouds are similar in nature to those of category (b), except that their number and frequency is such that the receiver outlet temperature never quite recovers from each cloud passage before the next occurs, and the outlet temperature becomes erratic. Although a control system might be capable of handling these clouds, the thermal cycling of the receiver tubes could significantly reduce the life of the receiver. Because of this, we have two alternatives under such conditions: (1) raise the salt flow rate and accept the drop in receiver outlet temperature, in order to reduce the cycle fatigue on the tubes; or, (2) shutdown. In the case of the SRE, we usually raised the flowrate and ran other tests. For a commercial plant, the receiver life is important, so it will probably be necessary to develop guidelines which the plant operator can use in deciding whether or not to shutdown.

d. Large, slow-moving clouds - With clouds like these, the insolation drops to zero or near zero for an extended period of time (several minutes or more) and the receiver outlet temperature drops accordingly if not under automatic control. The drop in insolation is usually slow enough that the control system can lower the salt flowrate and keep the outlet temperature relatively constant. However, if the sun should reappear from behind the cloud and the insolation rise very rapidly, the control system (operating off of the outlet temperature) would not increase the flowrate quickly enough to prevent the receiver from overheating. Therefore, the control system was switched to manual at these times and the flow rate kept constant.

e. Total overcast - We did not attempt to run during total overcast.

E. DESCRIPTIONS OF SPECIAL TESTS

Table III-2 shows each of the tests in the Test Plan and the status of each through 19 Dec 80. The receiver was not tested in its exposed configuration during the test program.

1. Convection Losses (No Solar Flux)

The aim of these tests was to determine the receiver convection losses by doing an energy balance on the receiver during steady-state operation. The tests were done with no solar flux to eliminate the uncertainties associated with the amount of solar input to the receiver. To get true steady-state conditions, we let the receiver outlet temperature stabilize at 371°C (700°F) and waited until the air cooler, sump, and interconnecting piping were all filled with 371°C molten salt. Then the heliostats were scrambled, and the flow slowed to about 2.5 kg/s (20,000 lbm/hr) to extend the time that the receiver inlet sees the slug of 371°C (700°F) salt. The radiation and conductive losses from the receiver can be calculated fairly accurately and subtracted from the total receiver losses ($\dot{m} c_p \Delta T$ across the receiver) to get the cavity convective losses.

Data taken includes receiver inlet and outlet temperature, salt flowrate, wind speed, and wind direction (so that the losses may be correlated to the wind conditions).

2. Receiver Losses as a Function of Temperature

This test was conducted to supplement the convection tests and to determine the effect of the receiver tube temperatures and the hot, inactive cavity walls on the receiver losses during solar operational conditions. The receiver is operated alternately at full-flow and at design-point conditions (roughly 75% flow) and the receiver thermal losses calculated at each flowrate. What is measured is the change in heat absorbed per change in (average) receiver tube temperature at a given solar input. This change is from the increase in thermal losses (radiation and conduction) due to the increase in receiver tube temperature. The convection component can be obtained by subtracting the analytically-estimated radiation and conduction components from the total.

After stabilizing at each flowrate the energy absorbed by the receiver is calculated ($\dot{m} c_p \Delta T$ across the receiver) and an RTAF scan is taken to determine the solar input. The difference between the two constitutes the total receiver losses, from which the convection losses can be calculated.

Table III-2 Test Program Plan

1	PC-1	Partial Load - Tower Console Control	Cavity	Complete
2	PC-2	Partial Load - Central Computer Control*	Cavity	Complete*
3	PC-3	Max. Load - Tower Console Control	Cavity	Complete
4	PC-4	Max. Load - Central Computer Control*	Cavity	Complete*
5	PC-5	Max. Load - Tower Console Control	Cavity	Complete
6	PC-6	Max. Load - Central Computer Control*	Cavity	Complete*
7	PC-7	Partial Load with Emergency Shutdown	Cavity	Complete
8	PC-8	Recovery from Simulated Cloud Passage	Cavity	Demonstrated for actual clouds
9	CC	Convection Loss	Cavity	Continuing
10	PFC-1	Efficiency Tests	Cavity	Complete
11	PFC-2	Max. Load for 20 Hours	Cavity	Complete
12	PFC-3	Recovery from Simulated Cloud Passage	Cavity	Demonstrated for actual clouds
16	SE-1	Cycle Tests	Cavity	Continuing; 153 as of 19 Dec 80
17	SE-2	Endurance Test	Cavity	Continuing; 96.3 Hrs as of 19 Dec 80
19	SE-4	Lateral Support Shadowing	Cavity	Complete
20	SE-5	High Localized Fluxes	Cavity	Complete

*All tests calling for central computer control require that the cooler be put on algorithm control. This has not been implemented. The receiver is run on algorithm--the cooler is run from the console or by manual computer keyboard control.

3. Turbulent-to-Laminar Flow Transition

This test was done to determine the flowrate (or range of flowrates) at which the molten salt flow transits from turbulent to laminar and to better understand the fluid dynamic characteristics of the molten salt at low flowrates. Finding this transition point and the critical Reynolds number is important because the heat transfer characteristics of the receiver change dramatically when the flow transits to laminar (the heat transfer coefficient is reduced by a factor of ten) and the receiver could burn up if permitted to operate below this point.

In this test, only the warmup heliostats are aimed at the receiver and the flowrate is lowered in steps. The sun-side thermocouple temperatures are monitored and recorded for any significant increase which might indicate flow transition. The system pressures are also monitored, as a drop might indicate transition to laminar. The flowrate is lowered to a minimum of about 10%.

4. Accelerated Cycle Fatigue Test

We ran this test to see how sensitive the receiver was to temperature cycling. With the receiver operating at 100% power (200-207 heliostats) and design point conditions [approximately 566°C (1050°F) receiver outlet temperature], the heliostats are scrambled to a special standby position above the receiver, then brought back on target again as quickly as possible (about one minute). When the outlet temperature reaches 549°C (1020°F), the heliostats are again scrambled [the outlet temperature overshoots to about 560°C (1040°F)] and the sequence is repeated. Each cycle takes approximately 3 minutes at midday, slightly longer at other times.

This accelerated cycling is more severe than the receiver would see in normal operation. As of 19 Dec 80, we had completed a total of 153 accelerated cycles (137 from design point conditions) and about 100 other cycles on the receiver.

5. High Flux Test

To show the effect of high localized fluxes on the receiver tubes, we moved in the aim point (towards the receiver tubes) by approximately 1 m (3.2 ft). Another objective of this test was to determine the effect of aim point location on receiver efficiency.

Once the receiver outlet temperature had stabilized at 100% power and 100% flow, the aim point of the heliostats was slowly moved from its position 0.45 m (1.5 ft) in front of the receiver aperture to a position 0.54 m (1.8 ft) inside the plane of the receiver aperture. This increased the flux to a maximum of 0.756 MW/m² (239,780 Btu/hr-ft²).

6. Lateral Support Shadow

Because of the height of the tube panels in a commercial receiver [roughly 15 to 30 m (50 to 100 ft)], there will be lateral supports of some kind to prevent tube failures due to high wind loads. These supports will cast shadows on the receiver tubes during solar operation and create severe thermal gradients across the shadows. We simulated a lateral support shadow on the receiver to evaluate the effect of such a shadow on the receiver tube temperature profile.

A piece of M-board refractory insulation was wired (from the rear) to the face of the receiver near the area of highest flux. Thermocouples were connected to the sun-side and back-side of the receiver tubes. We operated the receiver at design temperature [receiver outlet = 566°C (1050°F)], at 100% flow, and at a point halfway between the two, all at 100% power (204 heliostats). RTAF scans were also taken at each point.

7. Performance Tests (RTAF Scans)

The performance, or efficiency, tests are performed any time it is desirable to know what fraction of the solar energy entering the receiver aperture is absorbed by the receiver (during high flux tests, at solar noon on good solar days, etc). Performance tests were also run at a variety of power levels.

To get good data, solar input has to be essentially constant and the receiver temperatures and flowrate have to be stable. Receiver inlet and outlet temperatures and salt flowrate are recorded, a flowrate calibration is taken with the weigh tank, and then we take a scan with the RTAF.

8. Endurance Test

The endurance test was an on-going test aimed at accumulating as much operating time as possible with the receiver at 100% power (200-207 heliostats) and at design point temperatures [at or near 566°C (1050°F) outlet and 288°C (550°F) inlet]. The endurance test was continued on clear solar days when there were no cloud interruptions and the receiver was on analog or algorithm control.

9. Control Tests

Control tests were performed on the receiver SRE to determine the receiver's response to normal operating transients (such as cloud passage). These tests took the form of step-changes in flowrate and/or power to the receiver, and observation of the outlet temperature while the receiver was under analog or computer algorithm control.

F. TEST HISTORY

Table III-3 is a weekly summary of the receiver SRE testing from the first solar test (8 Aug 80). We tested on 76 of a possible 110 days during the program. Of the 34 days we did not test, 9 were test-related (installation of hardware, etc) and 25 were weather-related.

Table III-3 Weekly Summary of Receiver SRE Testing, 8 Aug 80 - 19 Dec 80

DATE	SUN HOURS WITH FLOW	SUN HOURS AT DESIGN CONDITIONS	MAJOR TASKS AND COMMENTS
8-8	-	-	FIRST WARMUP, HELIOSTATS ON RECEIVER
8-9 to 8-16	-	-	4 DAYS OF RAIN AND CLOUDS; WEATHER PROOFING PROBLEMS; RTAF COOLING SYSTEM PROBLEMS; POWER PROBLEM ON 480 V BREAKER.
8-17	3	-	FIRST SALT FLOW THROUGH RECEIVER
8-18 to 8-23	11.2	1.0	WEATHER PROOFING OPERATIONS; CAVITY DOOR WARPAGE, APERTURE INSULATION; 3 DAYS OF CLOUDS
8-24 to 8-30	19.2	.5	3 CLOUDY DAYS; PURGE VALVE CABLING OVERHEATED; CONTROLLER TUNING
8-31 to 9-6	22.1	15.7	2 CLOUDY DAYS; IV-1 BROKE DOWN; CONCENTRATED ON OPERATING AT DESIGN CONDITIONS
9-7 to 9-13	10.8	3.7	4 COMPLETELY CLOUDY DAYS; 3 PARTLY CLOUDY DAYS; FIRST CONVECTION TEST
9-14 to 9-20	19.9	9.5	3 PARTLY CLOUDY DAYS; INSTALLED RTAF; GOT RTAF DATA, BUT BURNED CABLING; OPERATED AT DESIGN CONDITIONS
9-21 to 9-27	14.1	5.0	2 CLOUDY DAYS; CHILLER PROBLEMS FOR RTAF BAR; RAN LOW POWER FOR COMPUTER CONTROL PREPS AND CHECKOUT
9-28 to 10-4	25.3	-	1 PARTLY CLOUDY DAY; RTAF BAR COOLING PROBLEMS; RAN COMPUTER CONTROL CHECKOUTS AT REDUCED POWER
10-5 to 10-11	35.8	18.8	1 PARTLY CLOUDY DAY; RAN COMPUTER CONTROL STEADY STATE AND POWER TRANSIENTS; MMC AND FRENCH VIPs
10-12 to 10-18	19.3	7.6	3 CLOUDY DAYS; RAN AT DESIGN CONDITIONS; CONVECTION TESTS; TURBULENT TO LAMINAR FLOW TRANSITION TESTS
10-19 to 10-25	-	-	HOT CONVECTION TESTING; RTAF INSTALLATION FOR 3 DAYS
10-25 to 11-1	-	-	PLANNED SHUTDOWN TO ALLOW FOR A.P.L. TESTING
11-2 to 11-8	-	-	PLANNED SHUTDOWN TO ALLOW FOR A.P.L. TESTING
11-9 to 11-15	16.1	9.1	1 CLOUDY DAY; 4 PARTLY CLOUDY DAYS; RAN FCV CALIBRATIONS AND ENDURANCE
11-16 to 11-22	12.8	.7	2 CLOUDY DAYS; 4 PARTLY CLOUDY DAYS; RAN FLOW CALIBRATIONS, REVIEWED LOAD CELL SYSTEM, RAN ENDURANCE AND CONVECTION TESTS
11-23 to 11-29	8.8	2.6	HOLIDAY; 1 CLOUDY DAY, 1 PARTLY CLOUDY DAY; RAN CONVECTION; ENDURANCE AND PERFORMANCE AT 75% POWER, AND 100% POWER
11-30 to 12-6	18.0	6.9	1 CLOUDY DAY; 4 PARTLY CLOUDY DAYS; RAN ENDURANCE, CONVECTION, PERFORMANCE AT 50% POWER, STEP FUNCTION TESTS AT 100% POWER
12-7 to 12-13	16.7	.2	*3 CLOUDY DAYS; 2 PARTLY CLOUDY DAYS; RAN LATERAL SUPPORT SHADOWING, DEVELOPED CYCLING PROCEDURE AND STARTED RUNNING CYCLES; TRIED TO GET A HOT SALT SAMPLE
12-14 to 12-19	17.4	3.6	3 PARTLY CLOUDY DAYS; RAN MAX FLUX TESTS, CYCLES, HOT SALT SAMPLES AT 100% AND 50% POWER AND 1050°F; SECURED SYSTEM FOR HOLIDAYS

IV. RECEIVER PERFORMANCE AND TEST RESULTS

A. THERMAL PERFORMANCE

1. Receiver Efficiency

Because of the direct effect of receiver efficiency on heliostat requirements - and cost - of commercial solar thermal power plants, the development of techniques for its accurate (within one or two percent) determination by direct measurement is highly desirable. Our experience with SRE and other programs of similar nature have clearly indicated, however, that this goal is not attainable within the current state of development of available instrumentation and measurement techniques. It appears that certain aspects of thermal performance, including radiation losses through the aperture, can be more accurately estimated by analyses than from measurements, and that such estimates can be effectively used to detect a possible bias in the results of the tests. In the case of the SRE, partial reliance on analyses was also necessary during input measurements, which were obtained by converting the power directly measured at the plane of the RTAF (approximately 0.3 meters from the aperture) into the actual input to the cavity, via a "transfer function."

To best utilize the blend of available analytical and experimental information generated during this program, the efficiency of the SRE was determined by two alternate approaches hereon referred to as the "input-output" method (IO), and the "input-loss" method (IL), respectively. The IO-efficiency is defined as the ratio of measured output to input; the IL-efficiency is obtained by subtracting the ratio of losses to input from unity. The latter relies on analytical techniques, since the determination of losses involves modeling, but with utilization of applicable empirical data such as the results of the convection tests and radiation measurements.

As shown by an uncertainty analysis in Section IV.D of Volume II, the IL is somewhat more accurate than IO, even when liberal allowances are made for the individual uncertainties of the analytical and empirical data that enter into its determination.

The two methods just described were applied to four efficiency determinations: (a) The IO-efficiency at design conditions, from 37 1/2 to 100 percent power, using the molten salt specific heat data originally supplied by Sandia; (b) the IO-efficiency at design conditions using specific heat data developed by Martin Marietta; (c) the IL-efficiency at design conditions and 100 percent power; and (d) the IO-efficiency from 50 to 100 percent power, at design temperatures, but with the aim point moved inside the cavity for the high flux tests.

The efficiencies at the design point as determined by (a) and (b) above are 82.5% and 85.7%, respectively, with an uncertainty interval of 7.6 and 7.9 percent, respectively. These compare with $85.3 \pm 5.0\%$ determined by the semi-empirical IL method. The latter was based on

conservative estimates of losses and liberal allowances for the individual uncertainties of those estimates, and it is believed to best represent the true efficiency of the receiver.

The output vs input data correlation is shown on Figure IV-1. The straight line through the data was determined by least squares fit, which indicated very little scatter in the data, i.e., a correlation coefficient of $r^2 = 0.996$.

The efficiency vs input as determined from this correlation is shown by the lower curves on Figures IV-2 and IV-3.

The efficiency based on the revised value for the specific heat as determined by Martin Marietta (Volume II, Subsection D.6) is plotted as a function of input on Figure IV-3. The output vs input relationship with the heliostat aim point data on Figure IV-4, and the corresponding efficiency curve is shown on Figure IV-2.

A comparison of the two curves on Figure IV-2 indicate an increase in efficiency of approximately 7% at design point as a result of moving the aim point inside the cavity. Although the absolute values of the IO efficiencies are questionable, the 7% difference is probably correct, in view of the lower percentage of incident fluxes on uncooled walls with the closed-in aim point.

The IL method differs from the IO method only in that we calculate the output by subtracting the losses from the input. The principal heat losses from the receiver include convection, conduction, and radiation losses due to reflection and infrared emission. These losses cannot be measured directly, but they can be estimated with reasonable accuracy by analytical modeling, with inputs, such as temperatures, solar absorptivities, and convection data, from the tests. This analysis, discussed in IVA-6, yielded the following estimated losses:

Reflected Radiation	=	6.0%*
Emitted Radiation	=	5.7%
Convection	=	2.8%
Conduction	=	0.2%
Total	=	14.7%

Using these values, the efficiency at 5 MW input is $85.3 \pm 5.0\%$. This efficiency is believed to best represent the actual performance of the receiver. The 5.0% uncertainty interval associated with this efficiency was determined by a detailed uncertainty analysis as described in Section IVD-3, Volume II.

As indicated above, the input-loss method of efficiency determination is a semi-empirical method dependent in part on empirical data, and in part on analyses. Included in the former category are convection, radiation, and conduction loss measurements, which are outlined below. This is followed by a brief description of the analytical model.

*This 6.0% reflection loss includes an estimated 3.0% reflected from the inside of the aperture "lip." This loss is test-peculiar and would not exist in a commercial receiver design.

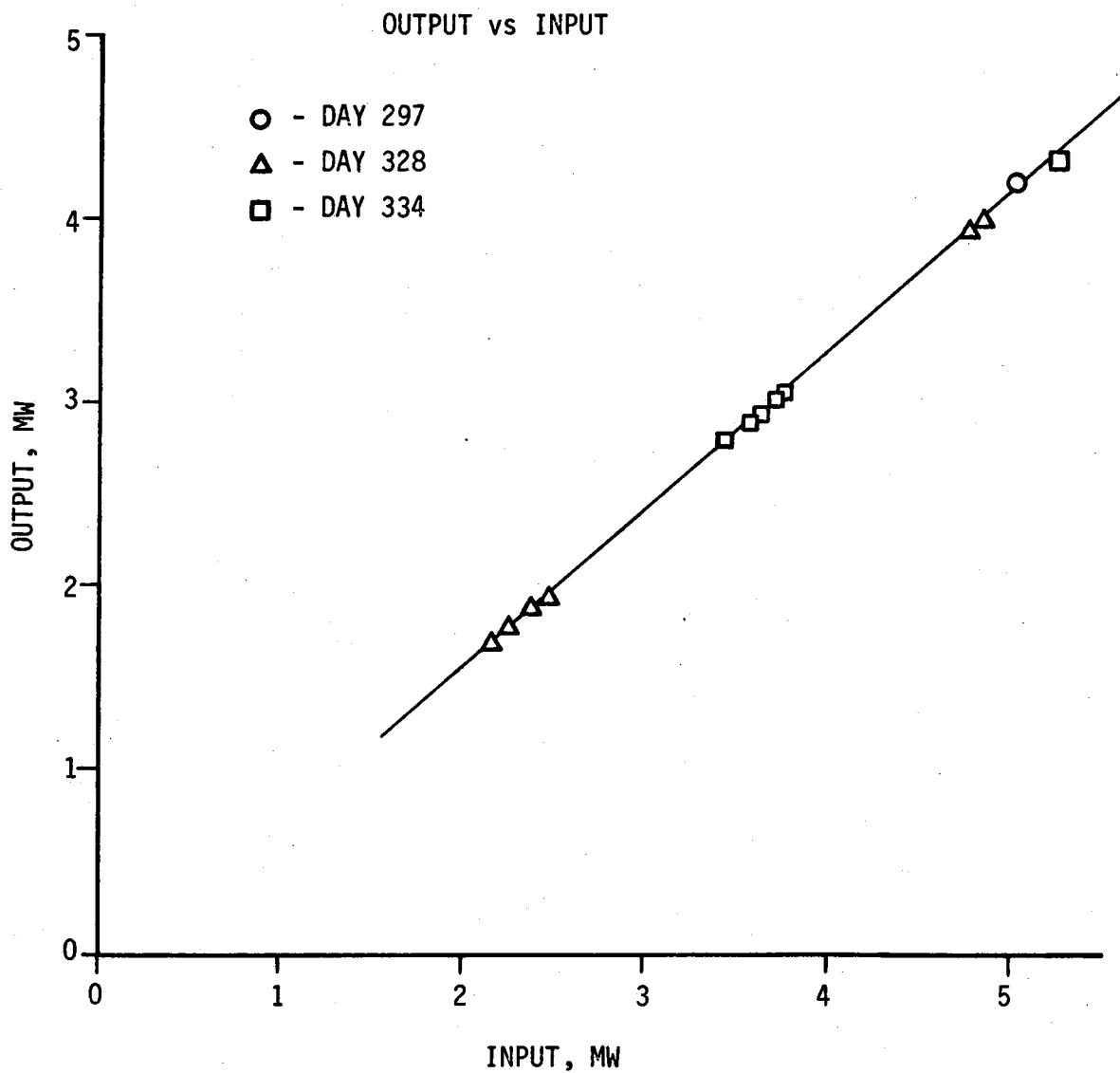


Figure IV-1 Output Vs. Input Plot

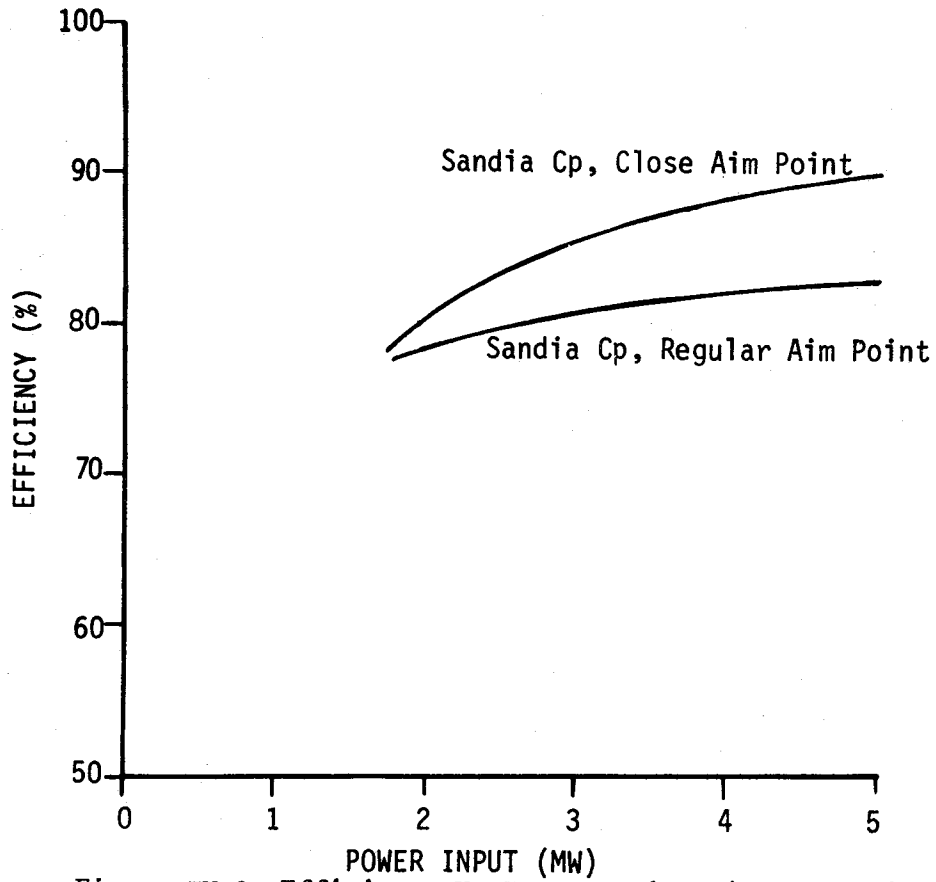


Figure IV-2 Efficiency Vs Input - Aim Point Comparison

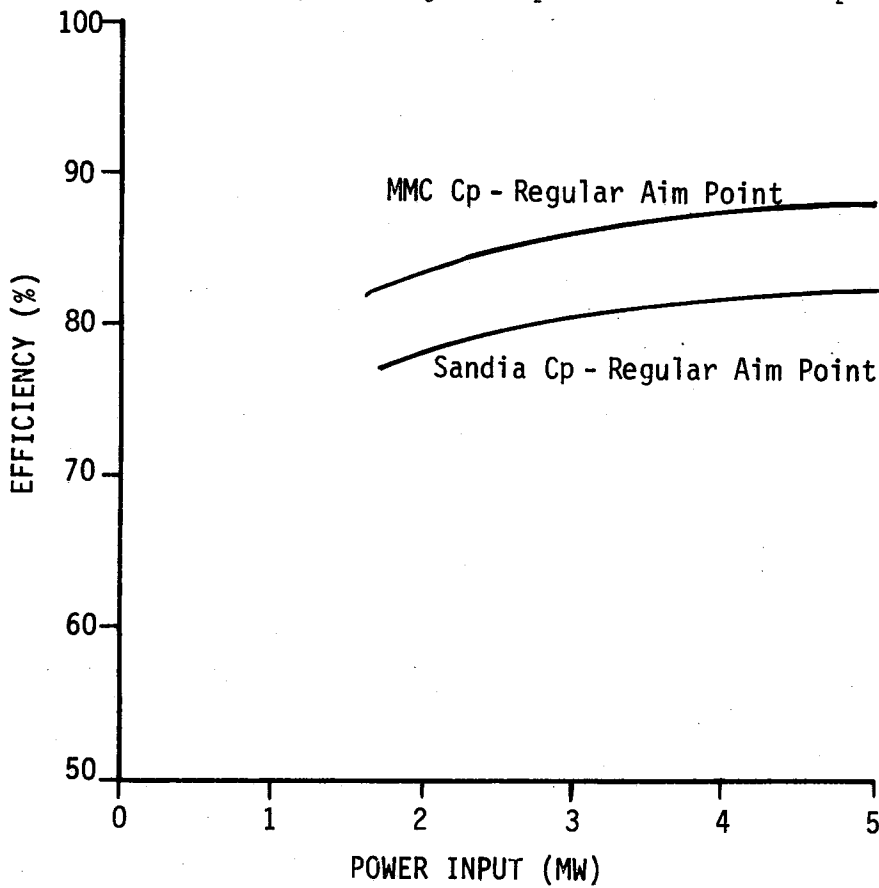


Figure IV-3 Efficiency Vs. Input - Cp Comparison

2. Convection Tests

The convection tests were performed by bringing the entire receiver system to a temperature of approximately 345°C (650°F) with a small group of heliostats supplying the thermal energy. After the system was thermally stable the heliostats were removed and the test was continued until the receiver inlet and outlet temperatures were constant with time. The total receiver loss is then computed by multiplying the working fluid flow rate times the specific heat times the temperature drop across the receiver. This total loss is made up of emitted radiation, conduction, and convection. It is relatively straightforward to account for the radiation and conduction losses analytically. Therefore the convection loss at the test temperature can be estimated.

The results of the tests in the Nusselt/Grashof-Prandtl plane is shown as a simple (average) point on Figure IV-5. On this same figure several correlations are plotted for free convection on a vertical flat plate for comparison.

Referring to Figure IV-5, it is observed that the average Nu from the tests is 16.4% lower than the corresponding Nu based on Sieber's correlation. Sieber's equation is based on an analytical study for natural convection from an exposed receiver, i.e. an open flat plate with no cavity and no forced convection components. The development of this equation accounts for temperature variations across the boundary layer and appears to be the best correlation to date for free convection from exposed solar receivers.

Based on the limited test data available, it is impossible to determine the effect of wind direction on the convection losses. Additional testing might resolve this problem; however, it may be that the effect of the wind is so minor, for a cavity receiver, that it is lost in the accuracy of the experiment. This thought is somewhat supported by the fact that the experimentally determined average loss with forced convection present is considerably less than the prediction by Sieber's for free convection only.

The convective loss from the absorber panel at design conditions as determined from the data is 1.43% of the 5 MW input energy. It must be recognized that this loss is based on the active (absorber panel) surface of the receiver only. Under solar load conditions there is also a substantial convection loss from the inactive receiver surfaces (cavity interior walls). Also the convection currents associated with the walls will interact with the absorber surface and tend to increase the losses from the absorber. The net result is that the total convection loss at design conditions (active and inactive walls) is higher than the extrapolated value for the absorber surface. Estimates of the total convective losses at solar load design conditions were made using a thermal model of the entire receiver including the radiation effects. The results of this computer study indicate a total convective loss of 2.75% and a total receiver efficiency of 85.3%. This model was based on the convection test results and coupled the convection between the active and inactive walls of the receiver.

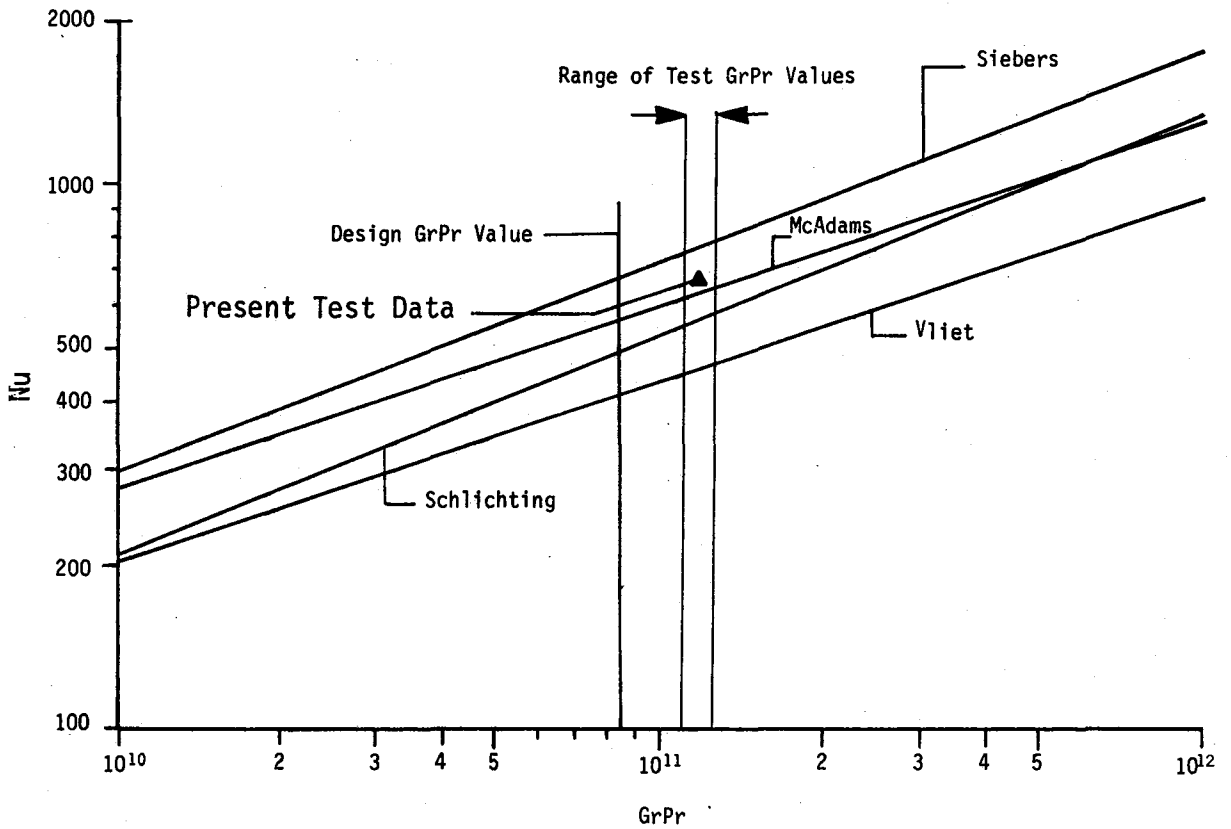


Figure IV-5 Existing Free Convection Correlations

3. Radiation Measurements

In an attempt to provide independent checks on the estimated radiation losses and per request by Martin Marietta, Sandia has performed three sets of measurements pertaining to the radiation characteristics of the cavity. They include: Solar absorbtivity measurements of the receiver tubes on days 197 and 351; net radiometer measurements of directional intensity of cavity radiation on Days 282 and 353, and pyrometer measurements of the cavity on day 282. The absorbtivity measurements closely agree with pre-test measurements (by Martin Marietta) and the values used in the analysis. The radiometer and pyrometer measurements, however, show inconsistencies that cannot be reconciled with either the absorbtivity measurements, or with the physics of cavity radiation as presently understood. Accordingly, no attempt was made to use them directly in radiation loss analyses.

4. Salt Specific Heat Determination

The specific heat of the molten salt used as the working fluid in the receiver must be known in order to accurately establish the efficiency of the system. Also this specific heat is required to perform the calculations involved in the special convection tests.

Several attempts have been made to determine the specific heat of the 60% NaNO_3 , 40% KNO_3 (by weight) salt mixture. The results of these measurements are shown on Figure IV-6. In each case the curve illustrates the temperature range of the specific heat measurements, i.e., the curves are not extrapolated beyond the measured temperature ranges. A linear extrapolation of the Sandia data has been used for all of the SRE receiver test data reduction. Using the Sandia expression for specific heat, the receiver efficiency is low relative to the expected values based on other analyses. Whereas it was expected that the receiver at maximum load would exhibit an efficiency in the range of 90 to 92%, the test results are about 82% when the Sandia specific heat data is used. Because of this, tests were performed by Martin Marietta, and Rensselaer Polytechnic Institute (RPI) was contracted to measure the specific heat of salt from the SRE receiver system. Both RPI and Sandia used a Perkin-Elmer Model DSC-2 Differential Scanning Calorimeter, considered by physical chemists to be the best apparatus available for specific heat determination. The specific heat tests performed by Martin Marietta were conducted using a simple insulated container which was specially designed and built for this purpose and were based on comparing the temperature decay rates of the container with and without salt in the container. A comparison of the two decay rates allows for an estimate of the salt specific heat. Referring to Figure IV-6 it is obvious that results from the Perkin-Elmer DSC produce considerable scatter. Except for the fact that the RPI-4 data set is based on placing the salt sample in open gold container, all the other RPI and Sandia experiments were identical in that gold capsules were employed to contain the salt. The salt samples used by RPI were taken from the receiver system as was the Martin Marietta test sample. Sandia did not use samples from the receiver system; however, all samples were 60% NaNO_3 and 40% KNO_3 mixture. One possible explanation for the DSC scatter is the size of the sample used which is typically 10 milligrams. Martin Marietta has

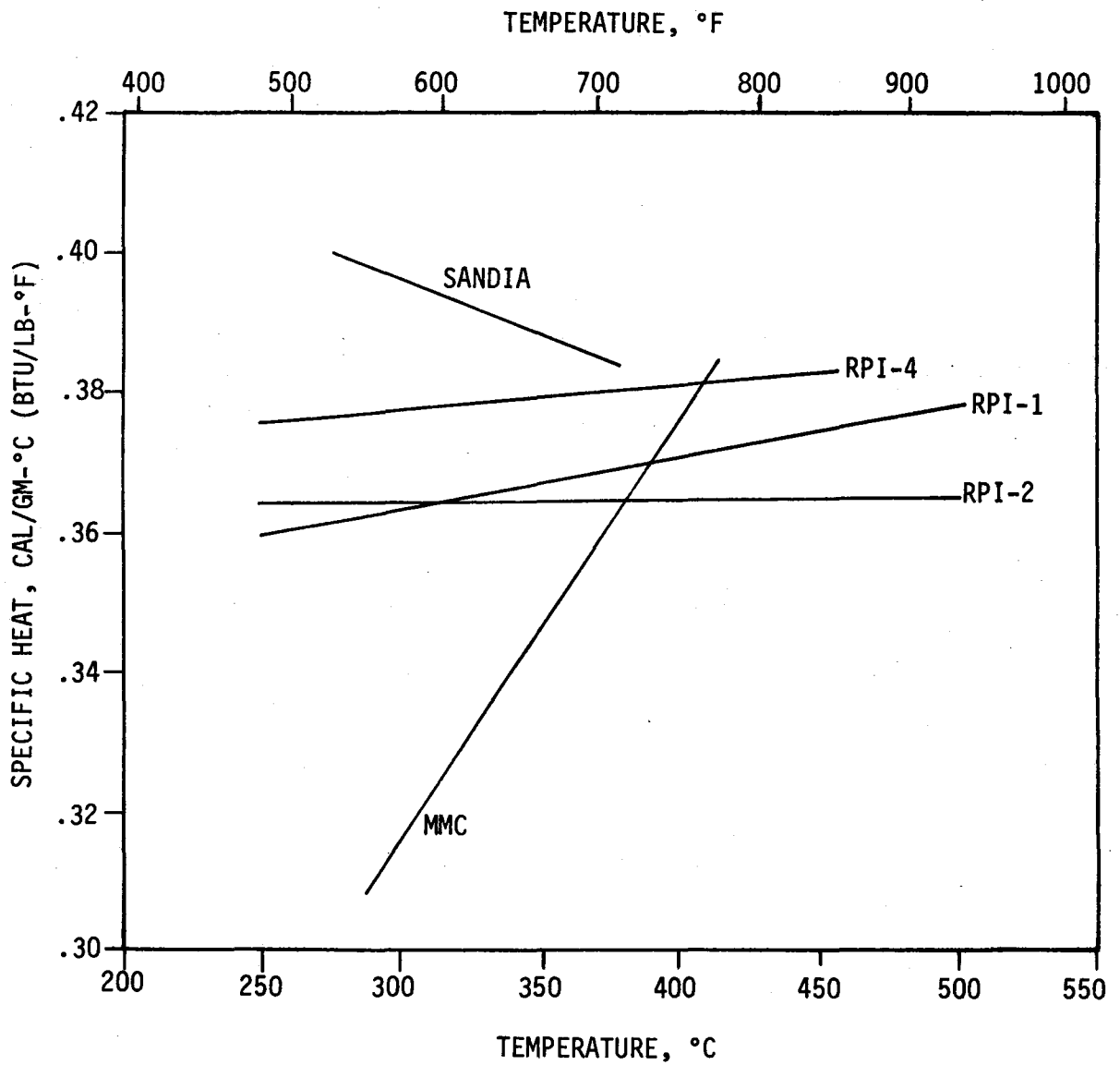


Figure IV-6 Molten Salt Specific Heat vs Temperature

observed in the past that if small samples are taken from as-received salt shipments there will be a large variation in the composition of the mixture. As for the RPI samples, it is likely that the salt was well mixed since the sample was taken from the receiver system pump after several months of operation. However, it is possible that on freezing the components of the mixture may have separated slightly and then, because the sample size is so small, they were not representative of a 60% NaNO_3 , 40% KNO_3 mix. Since the Martin Marietta test specimen was orders of magnitude larger than the DSC specimen, it should not have been affected by a composition variation.

It is obvious that the specific heat of the salt is uncertain at this time. Since this value is so important relative to establishing the receiver efficiency, further work must be performed to establish accurate values of the specific heat vs temperature. As far as this report is concerned, the Sandia specific heat data was used for the majority of the analysis and data reduction. An extrapolation of the Martin Marietta data was also used for the efficiency calculation.

5. Cavity Wall Conductive Losses

The thermal losses through the cavity walls during design point receiver operation, were determined by measuring the temperature drop across the insulated cavity walls.

The cavity wall conductive losses so determined are approximately 0.15-0.17% of the total solar power absorbed by the receiver.

6. Analytical Modeling

An analytical model of the SRE receiver was devised in order to estimate the system efficiency and identify the magnitude of the various losses. The Martin Marietta Interactive Thermal Analysis System (MITAS) computer program was used to model the receiver system. The radiation exchange between surfaces and the absorbed solar radiation on the exterior surfaces were defined using the Thermal Radiation Analysis System (TRASYS). Like the MITAS program, TRASYS has been used for a number of years by Martin Marietta.

The first step in the analysis was to force the thermal model to match the thermal behavior of one of the special convection tests. This was accomplished by imposing the experimental boundary conditions on the model, i.e., inlet salt temperature, salt flow rate, and ambient temperature. (Note that there was no solar input during the convection tests.) Then the convection film coefficient values were varied until the salt outlet temperature from the model matched the experimental value.

With the film coefficients set, the model was then used to analyze a solar load design point condition. The experimental data used for this activity was on day 328 at 11:50 a.m. For this analysis the receiver inlet temperature, salt flow rate, ambient temperature, and incoming solar flux were set to match the test data. The value for the salt specific heat was varied until the receiver outlet temperature predicted by the model matched the experimental value. Since the model was being used to calculate losses only, varying the C_p does not affect the final answer (as it would in, say, calculating the output).

With the model tuned to match the test conditions, the losses were then calculated by the model. The IR radiation loss was determined by summing all the energy flow to the radiation sink temperature. Likewise, the total convection loss was defined by the energy flow to the ambient temperature. The solar reflected loss was estimated by TRASYS to be 6.0%. This energy was not involved in the MITAS calculations, which consider only the absorbed solar on the various receiver surfaces and the IR energy exchange. The result of this analysis is as follows: IR loss 5.7%, convective loss 2.8%, reflective loss 6.0%, conduction loss 0.2%, for a total loss of 14.7%.

It is felt that the approach used here is a reasonable method of estimating the losses. First of all it is based on experimental results, both convection tests and the solar tests at the design point. Also, the IR radiation and convection are coupled in the program. Further, the convection from the cavity walls is coupled with the convection from the absorber panel.

The reflective loss for the SRE is significantly higher than that expected in a commercial receiver. We believe that the higher loss is due to the fact that in the SRE there is about 13% of the solar radiation incident on the uncooled walls of the cavity which is much more likely to be reflected out than is the radiation which is incident on the active surfaces. In the commercial design there is expected to be about 2% of the incident solar energy on uncooled surfaces. Also, in the SRE about 6% of the incident solar energy strikes the inside surfaces of the aperture (the 0.3-m [1-ft] wide aperture lip) as a result of the sharp angles of the incident radiation, which is unique to the SRE. Since most of this 6% reflected energy is very close to the aperture, it is reasonable to assume that about half, or 3% would be lost. This loss is included in the overall 6% reflected losses.

B. THERMO-STRUCTURAL PERFORMANCE AND DESIGN DATA

The design operating conditions on the SRE produce a widely varying set of temperature profiles both across the total array of tubes and also across the individual tube cross-sections. These temperatures in turn induce tube deflections and tube stresses. The thermally induced stresses are associated with three primary mechanisms:

- 1) The non-linear distribution across the tube cross-sections results in compression stresses on the front and back tube faces, and tension at the tube sides necessary for each section taken through the tube to remain plane.
- 2) The higher front face tube temperatures cause the tubes to bow toward the heat flux. Since the upper ends of the tubes are fixed, a moment reaction is induced at that location. This moment varies linearly from a maximum at the upper end to zero at the lower lateral support reaction. Therefore the induced stresses are compression on the front faces and tension on the back faces.
- 3) The difference in average tube temperatures from one pass to the adjacent pass results in induced longitudinal tube stresses, some tension and some compression.

Additionally, there are secondary stress effects such as at the tack welds and at the intersection of the tubes and headers. However, since stresses were not measured during the tests, this analysis primarily addresses the temperatures, deflections, weld failures, and permanent tube deformations. The results of the lateral support shadowing test and considerations for future design, and analytical and test work in the thermo-structural area, are also included.

1. Tube Deflections

Deflections were predicted by using a NASTRAN finite element model of a typical tube and applying an equivalent thermal loading to simulate the non-linear temperature gradient across the tube.

The maximum measured deflections from day 286 are tabulated in Figure IV-7 together with the values which were predicted. Considering that temperatures were close to predicted, the measured data is approximately twice predicted. The reason for this discrepancy lies in the assumed temperature distribution in the tubes, which will require correction in future analyses, as discussed in Section IV.E of Volume II.

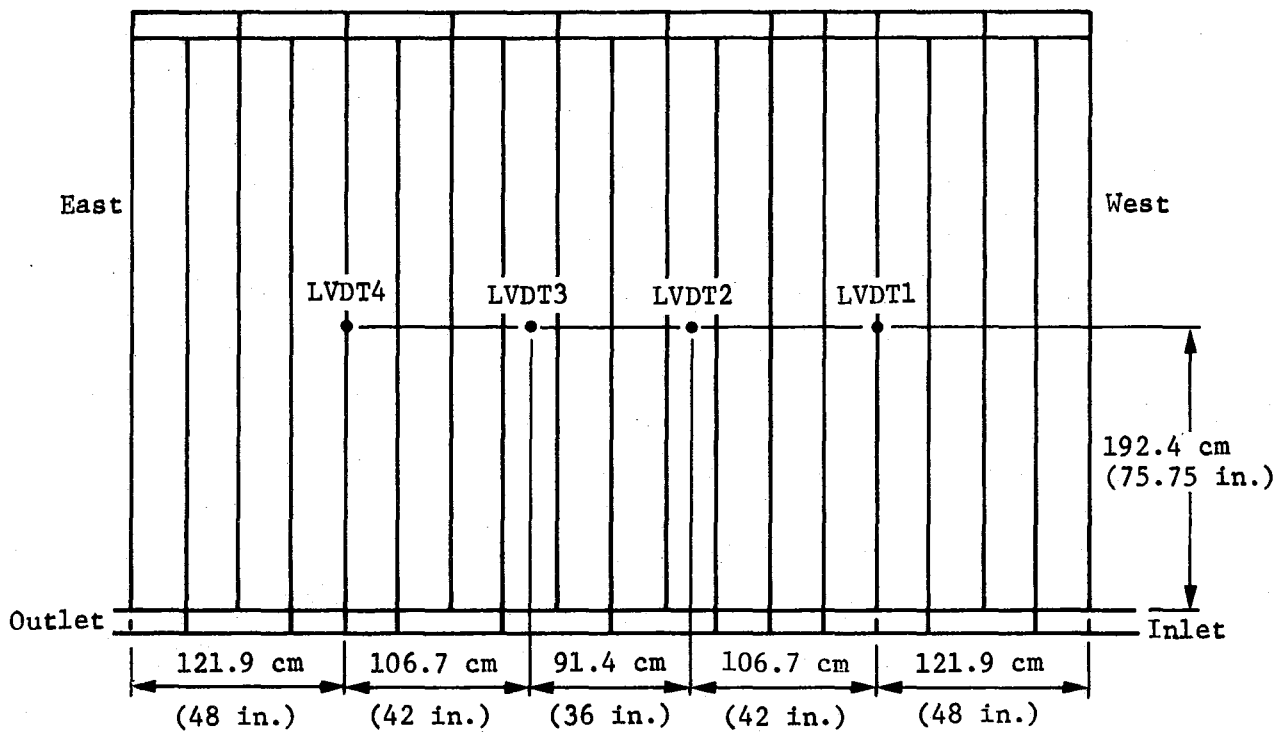
2. Weld Failures

Many of the tack weld-joints failed during testing, but on different days. Figure IV-8 shows the locations of the weld failures together with the failure dates. Only the front face welds are shown since in most cases those on the back face are not visible. The phenomenon which caused these weld failures was primarily the transfer of longitudinal shear loads necessary to equalize the tube lengths. The large majority of failures occurred in those welds which joined adjacent passes where tube temperature differentials were maximum. It would be expected that the welds closest to the tube ends would be the first to let go assuming equal strength welds, and in particular, the tubes which enter the manifold ends (rather than at the manifold mid-length point). An examination of the diagram and dates shows this to be the situation. The failures then progressed toward the other ends of the tubes on successive days (zippering effect). The number of successive failures that occurred was a function of weld strength at temperature (including cyclic damage), the differential temperature between passes, and the remaining length of tube between the last unfailed weld and the manifold at the other end.

A review of data from the warm-up mode (a few heliostats operating with no salt flow) shows that temperature differentials of 3-4°C (5-7°F) occur between adjacent tubes [156°C (280°F)] over a width of three passes). This condition has not been analyzed; however, it appears to be a possible source for the weld failures.

3. Permanent Tube Deformations

Permanent tube deformation occurs when areas of the tubes are stressed above the yield allowable of the material at the particular operating temperature level. When the applied load (differential temperature between front and back faces) is removed, residual stresses of opposite



Instrument	Max Measured Deflection (Day 286, mm/in.)		Predicted Deflection, mm/in.	
LVDT 1	81.3	(3.2)	38.1	(1.5)
LVDT 2	87.6	(3.45)	43.2	(1.7)
LVDT 3	81.3	(3.2)	38.1	(1.5)
LVDT 4	63.5	(2.5)	27.9	(1.1)

Figure IV-7 Out-of-Plane Tube Deflections

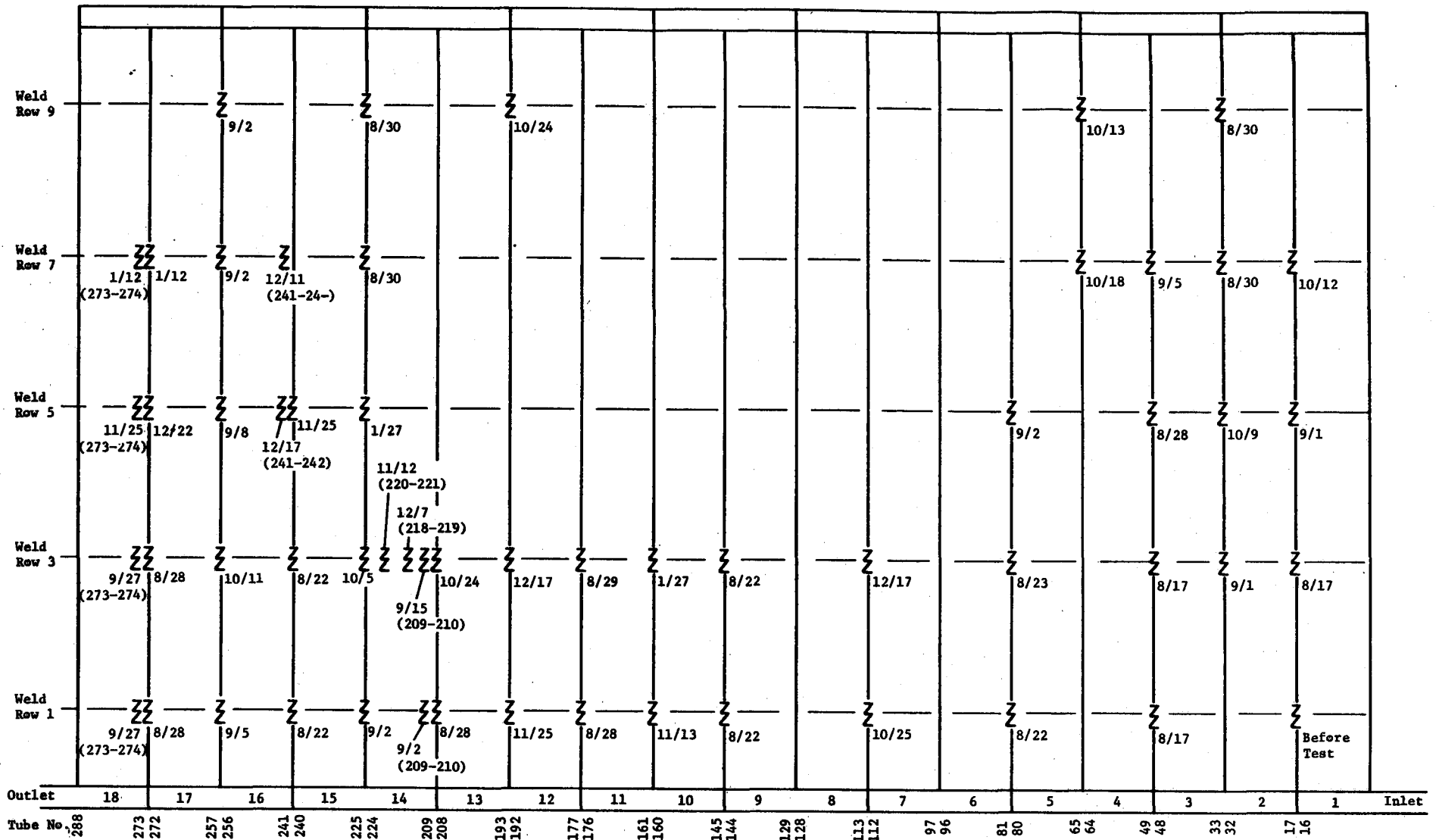


Figure IV-8 Weld Failure Locations with the Failure Dates

sign usually result, together with the residual deflection (permanent set). The highest predicted stresses for the SRE tubes are compression on the front face about 70% of the way up from the lower header. Since the local permanent strain is compressive, the unloaded position should be such that a local concave curvature exists on the front side of the tubes. Since the upper ends of the tubes are clamped against rotation, the lower support will end up pushing against the front face and inducing additional front face residual tensile stresses. Therefore the predicted permanent deflected position would be similar to that shown in Figure IV-9.

The actual permanent deformations are depicted in the same figure. The largest deformation occurred in the end tube of pass 18 and is very much like the predicted shape. The end tube of pass 16 bowed more in the middle portion of its length rather than near the lower end since it is restrained by tack welds to the adjacent tube. Other less severe deformations are also shown. Directions of permanent set are not always obvious, particularly since many of the tubes are beam columns and initial eccentricities could dictate which way they deform.

4. Lateral Support Shadow Test

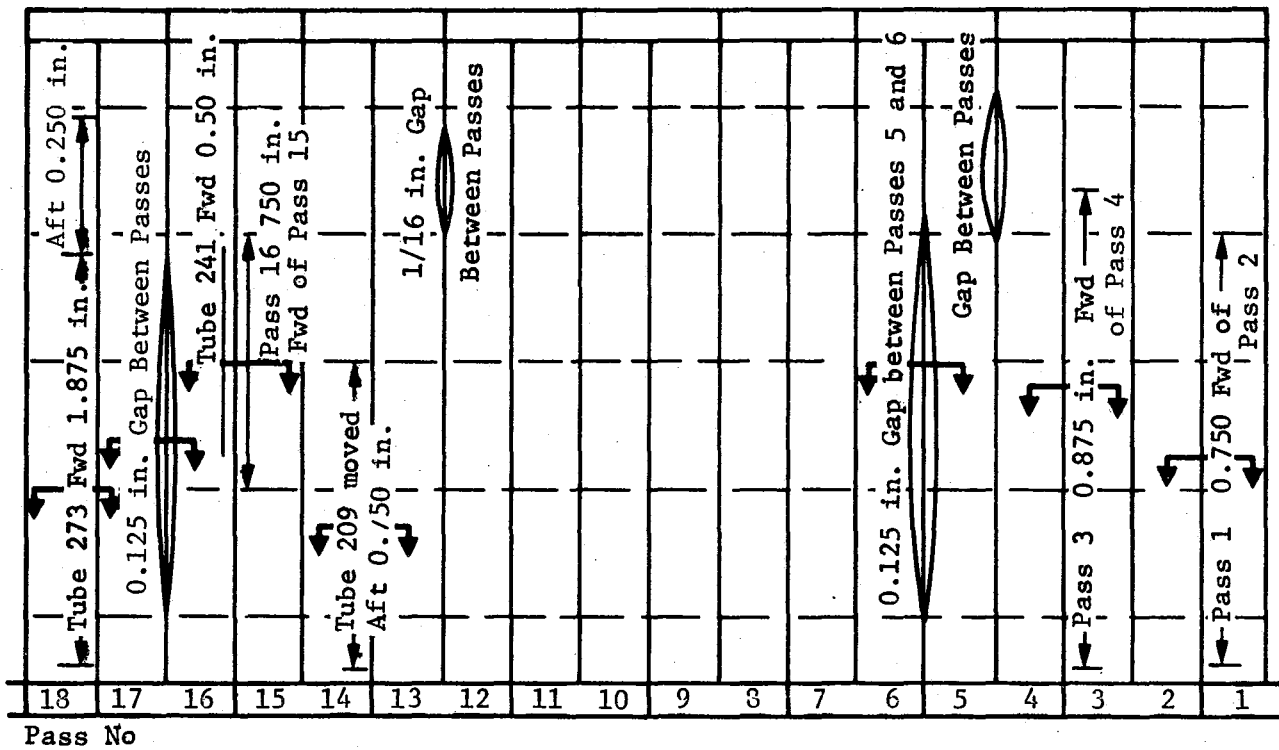
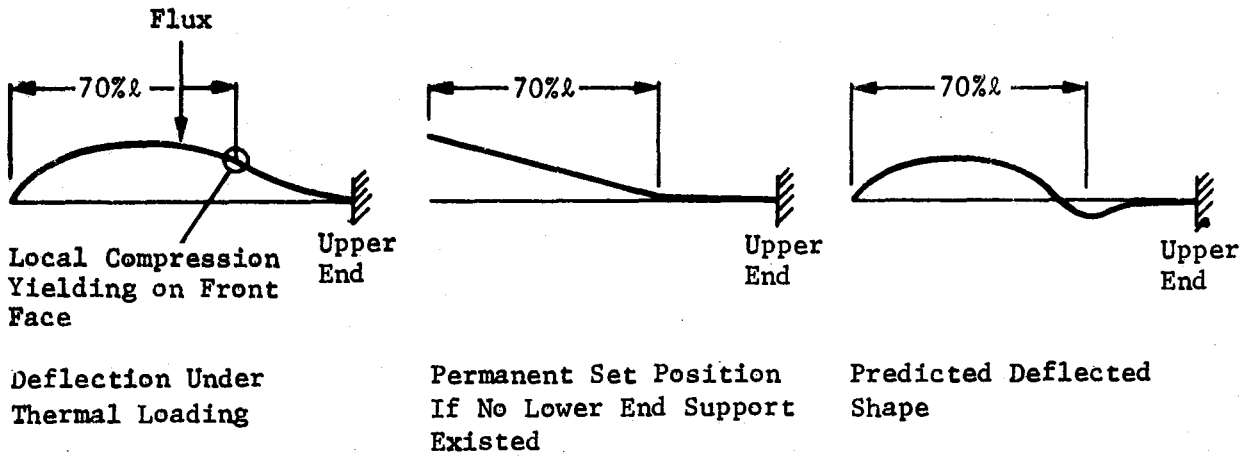
The special test to simulate the effect of shadowing from a lateral support member showed a maximum front face local temperature change of approximately 139°C (250°F) per inch in the axial direction. The back face temperature was essentially constant over the same distance. This type of gradient will produce local shearing stresses to balance out the varying levels of thermally-induced longitudinal stress.

The shearing stress is a function of the amount of material that is acted upon by the unequal axial stresses an inch apart. As an approximation, assume one-fourth of the front face circumference experiences an induced compression stress varying from the maximum value to zero. This gives a shearing stress of 19,513 kPa (2830 psi). This stress is well below the allowable and also it occurs at a different location on the periphery of the tube than the maximum axial stress.

5. Recommendations for Future Work

Several areas should be considered for future work efforts.

- 1) The design should be configured so that tack welds do not fail and at the same time so that they do not induce excessively high local tube stresses. We suggest that the tubes and headers between passes not be welded.
- 2) The deflection prediction errors will be corrected in future work. Deflection and stress prediction are closely interrelated and we would propose that much more extensive use be made of non-linear finite element modeling. The existence of non-linear deflections should be accounted for since portions of the tube arrays are effective beam columns.



Sections



Figure IV-9 Permanent Tube Deformations

- 3) A more detailed analysis should be made of typical temperature distributions at a tube cross-section to generate a set of design data to quickly predict induced stresses to maintain plane cross-sections. This would be a combined thermal-stress analysis.
- 4) A test program to check combined creep and fatigue damage should be defined. Since the compression stresses are usually larger than tension, we need to develop a criteria for acceptable levels of compression above yield. Acceptable tension levels should also be validated by test.

C. THERMO-HYDRAULIC PERFORMANCE

The test results have shown that pumping requirements (pressure drops) and heat transfer coefficients can be predicted by available standard correlations, and that their levels are consistent with projected commercial-scale receiver designs. The need for improvement is indicated primarily in the area of available thermo-physical property data for this particular mix of salts.

1. Pressure Drop Correlations

The pressure drop through the receiver and cooler was predicted by the use of the D'Arcy-Weisbach formula, with friction factors obtained from the Moody chart, and with molten salt properties varied as a function of temperature. Because of the temperature-dependence of salt properties--especially viscosity, which decreases by a factor of four from receiver inlet to receiver outlet at design conditions--the pressure drop through the receiver was predicted by a small computer model via step-wise integration along the flow path. The result of this calculation is shown by the lower curve on Figure IV-10. Also shown in this figure, by the upper curve, is the measured pressure drop through the entire system comprising receiver, cooler, and interconnecting piping. Note that the pressure drop through the receiver alone could not be measured directly due to the unavailability of suitable pressure instrumentation that could withstand the temperature environment at the receiver exit during molten salt operation. The receiver pressure drop was measured, however, during the water-flow checkout tests, and the data have confirmed the prediction that the receiver played the dominant role in the system pressure drop.

The upper curve on Figure IV-10 represents a "best fit" through a relatively large number of data points. An examination of these data does not reveal any significant effects due to either temperature or flux rates on the overall pressure drop of the system. A more detailed examination of data obtained during fast ramp-up (from warmup power to 100% power in less than six minutes), the high-flux tests, and the cycle tests, indicated small changes in pressure drop due to heating that were consistent with the effects of changes in bulk viscosity on the Reynolds number, and hence, on the friction factor. Typically, during a fast ramp-up, the flow rate (at constant flow control valve position) would increase by approximately two percent, with a corresponding increase in the pressure drop of approximately 4%.

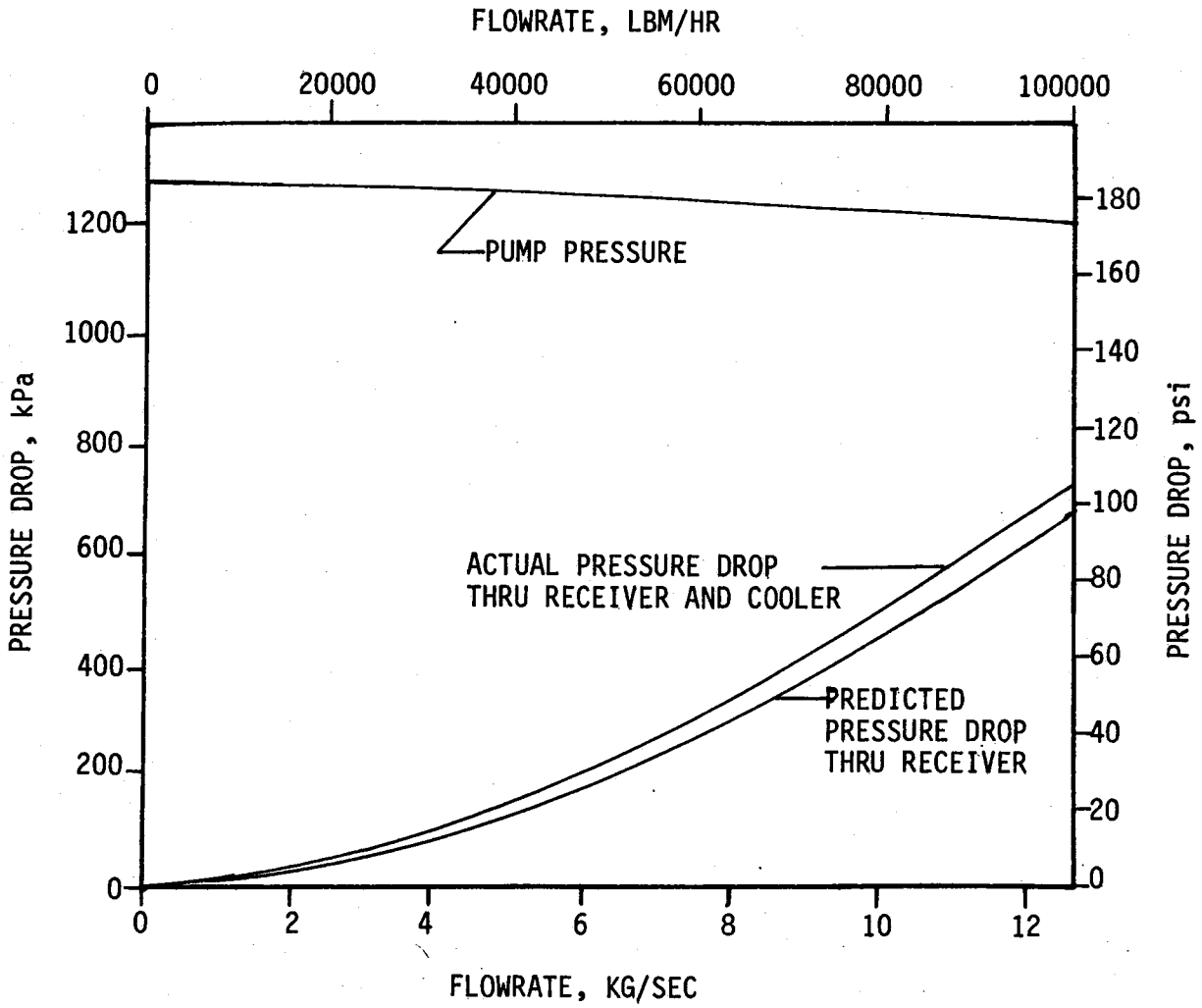


Figure IV-10 Pressures Vs Flow, Receiver SRE

It is instructive to compare the above results with the pressure drops obtained with water (during the water flow checkout tests) in the same system. The water flow and salt flow data are presented on Figure IV-11, a more generalized presentation of all of the pressure drop data in the form of the (non-dimensional) friction factor vs Reynolds number. The following observations are made: (a) the scatter in the data is significant but not unusually high considering the size and complexity of the system; (b) the salt data shown more scatter than the water data, which is not surprising; (c) throughout their common range of Reynolds numbers, the salt and water data overlap each other, as predicted by theory; (d) there is no evidence of "trip-over" from turbulent to laminar flow, or gradual approach to laminar flow, above a Reynolds number of about 4000; and (e) the "best curve" fitted through the data (by inspection), shown as a dashed line on Figure IV-11, follows the prediction by the Moody chart for turbulent flow in rough tubes, with a roughness factor of $e/D = 0.008$ (approximately). Although consistent with available data on commercial tubing, this number is probably higher than actual due to the fact that the L/D values in the friction factor calculations were based on the receiver tubes alone. (The actual roughness of the SRE tubing has not been determined by measurement.)

2. Flow Distribution Within the Receiver Passes

The SRE is an 18-pass receiver with a single control zone and 16 parallel tubes per pass. Consecutive passes are connected by headers, which act as flow distributors. The axial velocities in these headers were calculated to be small when compared to tube velocities, and no flow distribution problems were expected. However, since a plugged tube or uneven flow distribution through a pass could lead to failure of a tube, it was deemed necessary to provide special instrumentation to ascertain the flow distribution through each of the 18 passes. This instrumentation consisted of 288 differential thermocouples that measured the temperature rise between the upstream header and the discharge end of each tube. An analysis of the data showed that the temperature rise in the 16 tubes in a given pass were very close. Since the heat flux does not vary much from tube to tube in a pass we are confident that there was very good flow distribution from tube to tube.

3. Metal Temperatures

Acceptable limits on tube metal temperatures were measured at five locations, including high flux areas, on the receiver. While some of these thermocouples had to be replaced periodically, four out of five remained operational during a sufficient number of tests to provide meaningful data on peak metal temperatures. The measured peak metal temperatures and their comparison with predictions are discussed below.

The metal temperatures were predicted for design conditions by a thermal-hydraulic computer model. The temperatures were determined at 11 locations along each flow pass (total of 98 locations) with four values predicted at each location, viz. (a) local peak temperature on the sun-side of the node; (b) semi-circumferential average of the sun-side temperatures; (c) the average inside metal temperature; and

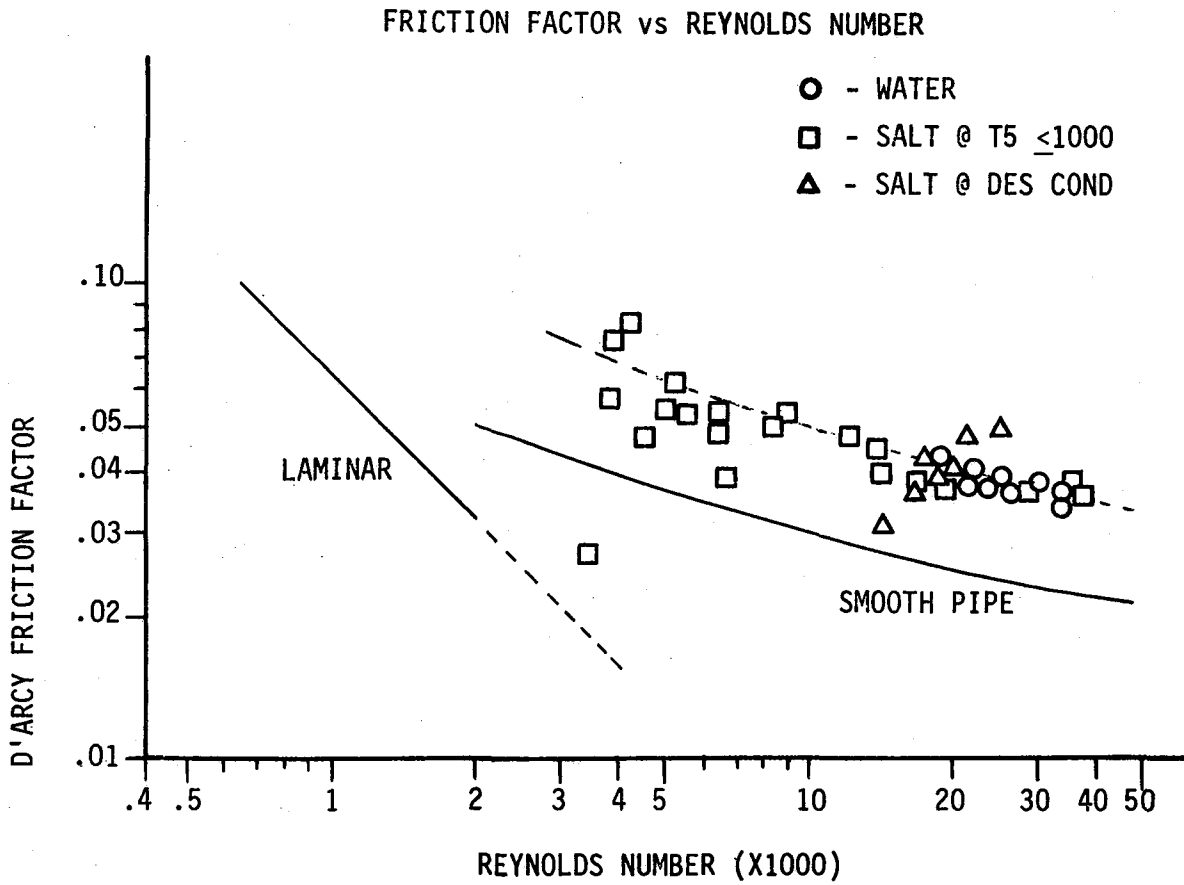


Figure IV-11 Friction Factor Vs Reynolds Number, Receiver SRE

(d) salt bulk temperature. By selecting the maxima of (a), for each of the 19 passes, and plotting them against the corresponding values of (d), the curve of Figure IV-12 results. This represents the loci of maximum metal temperatures in each pass. The 45° tangent to the maximum local temperature curve determines the point where the maximum front-to-back temperature gradient occurs (i.e., maximum metal temperature minus salt temperature).

Superimposed on these predictions is the data obtained with the sun-side thermocouples during typical operation at design conditions. The peak values exceed predictions by a small amount, and the temperature pattern indicates a dip around the area where the maximum front-to-back temperature gradients occur. Since adequate margin was used in the thermo-structural design of the SRE, and since the temperature measurements are subject to some error, the slightly-higher-than-predicted maximum front tube temperatures are not a concern.

Figure IV-13 shows typical traces of front tube and corresponding back tube temperatures during the cycle tests. Also indicated on the figure are the approximate times when 0% and 100% power was reached during each cycle. The maximum front-to-back temperature differences were approximately 11°C (20°F) higher than during normal operation at comparable peak temperatures. This indicates that the cycle tests represent a valid approach to accelerated life testing.

Since the peak front tube temperatures are closely related to the distribution of incident fluxes, the flux levels at the front tube thermocouple locations (which are the same as the flux gauge thermocouple and back tube thermocouple locations) were checked to compare actual values with predictions. A close agreement between test and predictions was obtained.

4. Operational Observations

a. Pump performance - The vertical cantilever shaft molten salt pump supplied by Lawrence Pumps, Inc., performed within specifications and without problems throughout the program. Pump outlet pressures, with flow, slightly exceeded predictions (by 3 to 6 percent), and power requirements were below those expected; typically, 39.6 kW measured vs 57.6 kW by specifications at design flow conditions.

b. Fill operations - A necessary condition for a successful fill operation is that the receiver tubes, headers, and all interconnecting piping be preheated to temperatures exceeding the melting point of salt by a comfortable margin. A desirable condition is to maintain metal preheat temperatures as close as possible to the temperature of the salt to be introduced into the system, in order to minimize thermal stresses near the inner surfaces of the tubes and due to pass-to-pass temperature differentials during the initial contact of the salt with the metal. The first condition was fulfilled by a combination of trace heating of the headers and of the interconnecting piping, and by the use of "warmup heliostats" to heat the receiver tubes. The second condition could only be marginally fulfilled because of the incident flux and tube temperature gradients associated with the heliostat warmup operation. This was expected on the basis of pre-test studies of flux distributions at the warmup power level.

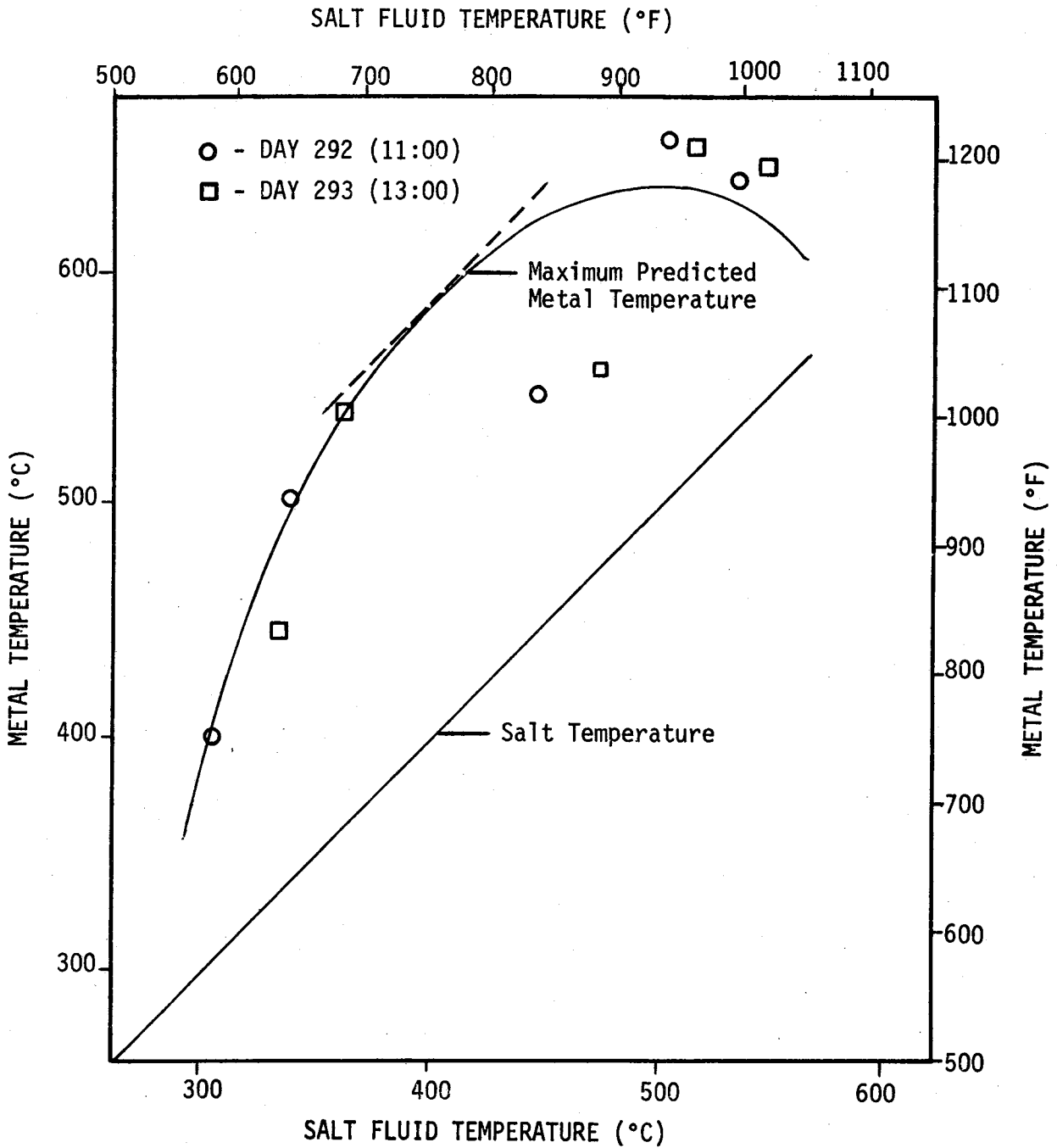


Figure IV-12 Predicted and Actual Metal Temperatures Vs Salt Temperature

TEMPERATURE vs TIME

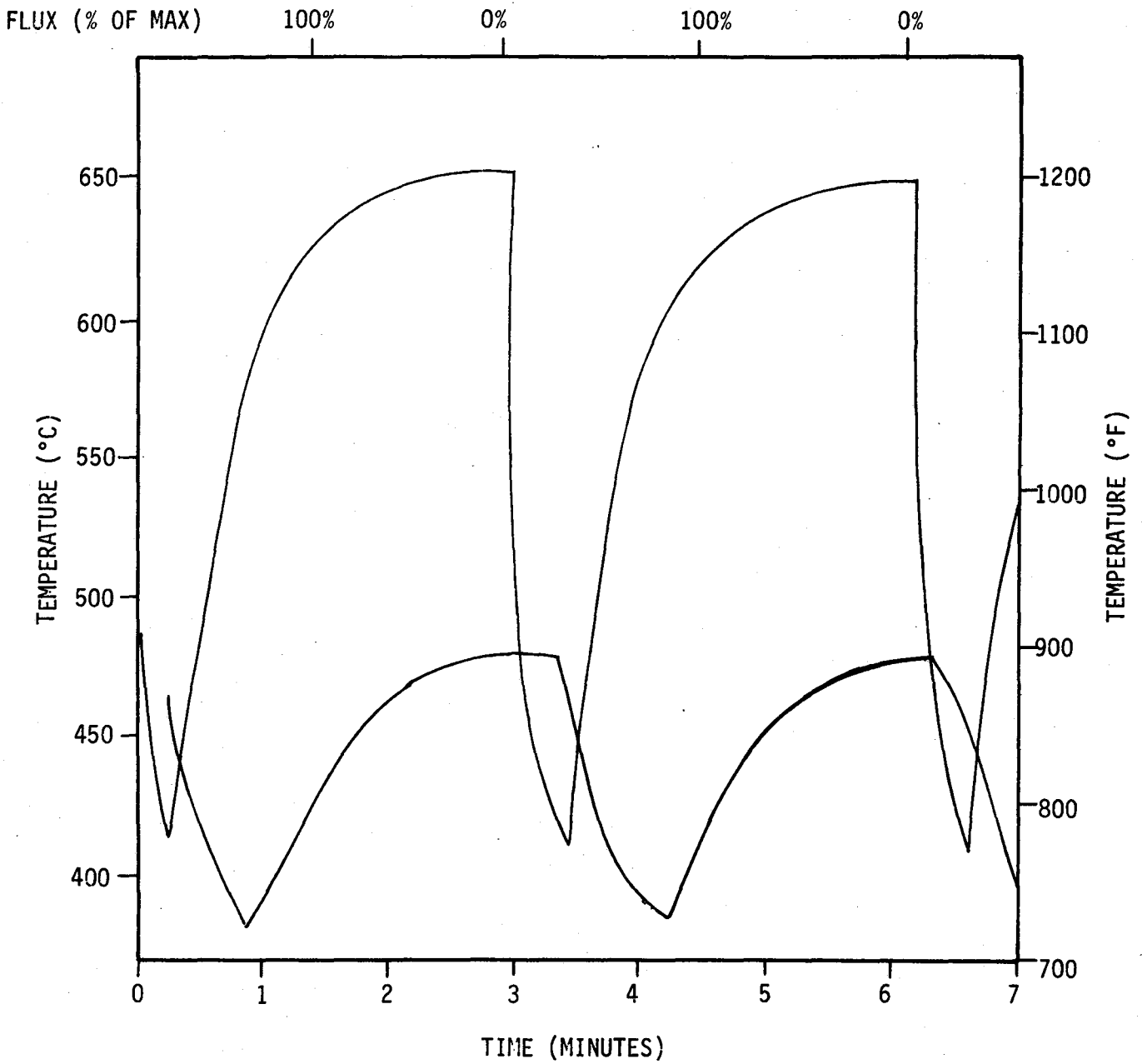


Figure IV-13 Temperature Profiles for Accelerated Cycles

In order to minimize pass-to-pass temperature differentials, the passes were filled in parallel, from lower headers to upper headers, through the drain valves, with overflow provided by the purge valves.

After flow was established throughout the system - approximately one minute after starting the pump - the drain and purge valves were closed, and the system was checked for air entrapment, by comparing the pressure drop and flow rate with "standards" established earlier in the program during the salt flow checkout tests. This method of checking is very simple and seemed to work very well.

c. Drain operations - Two methods of draining the system were provided for in the design of the SRE, and were tried out during the tests. These were gravity drain and purge-assist drain. The idea behind the latter was to accelerate the draining process by using high pressure (and temperature) purge gas to force the molten salt out of the system and into the sump. This did not prove very effective during the test: the purge gas had a tendency to break through the salt in certain portions of the flow system, essentially leaving the other portions to gravity drain. Gravity drain (without purge), on the other hand, proved to be entirely satisfactory.

d. Flow fluctuations - A yet unexplained phenomenon that becomes somewhat of a nuisance during test operations was the appearance of a low-amplitude (3 to 5%) low-frequency (12 to 15 cycles per minute) fluctuation of the flow rate, within the range of flows from 6.3 to 8.8 kg/sec (50,000 to 70,000 lb/hr). This instability was observed most of the time - but not every time - in that flow range, in both manual and automatic control. It had an adverse effect on the flow control valve (FCV) which had a tendency to gradually drive itself closed in this environment. A similar effect was observed on the isolation valve (IV-1) during the water flow checkout tests, and as a result, this valve was deliberately kept in the fully-open position for the remainder of the test program. (The FCV and IV-1 are of similar design and construction, made by the same manufacturer).

As a consequence of these fluctuations, some of the partial-power and laminar-flow tests were conducted with FCV blocked in a fixed position.

D. RECEIVER CONTROL

The receiver SRE was equipped with three types of controls; manual, analog, and algorithm. Manual control was used extensively during startup, shutdown, and special test operations, as well as in an override capacity when erratic behavior of the automatic control systems so warranted. The analog and algorithm control approaches are potential candidates for commercial receiver applications, and were evaluated on a comparative basis during this program. These are outlined in the paragraphs below. Also included in the discussion is the analytical simulation of the SRE control dynamics, and some limited test results with an improved control algorithm incorporated into the SRE as a result of the simulation studies.

1. Manual Control

Of the three control approaches used, manual control is the simplest to visualize and to build. However, it requires training for the operators to be able to control well. Manual control of the SRE involves only control of two input variables: salt flow rate and cooler fan blade pitch. The two dependent variables being used for feedback are: receiver outlet salt temperature and cooler outlet salt temperature.

The man/machine interface equipment used for this type of control is on the main control console in the CRTF tower (Figure III-13). The salt flow control equipment is shown a little to the right of the top center of the figure. The black box displays receiver outlet salt temperature and has a dial for setting flow control valve position. Valve position is displayed on the meter to the right of the temperature indicator. Air cooler outlet temperature is displayed on the dark box shown in the lower left hand part of the figure. This same box has separate dials for setting the pitch of the two fans. Fan pitch angle is also displayed on the controller.

This arrangement of controls and displays was best operated by two people: one operator for the receiver and one operator for the cooler. Control action followed the "adjust-and-wait" approach because of slow system response and the interactions discussed above.

SRE operational experience has indicated that manual control is not accurate enough for even small disturbances. While manual control is very useful in a test situation, it is not viable for a commercial installation, except in emergency situations.

2. Analog Control

The analog control approach was applied to both the receiver and the cooler. The analog equipment used involved electronic components for control logic and pneumatic elements for valve and fan blade actuation. Analog control techniques have been used for heat exchanger control for many years. The various gains were selected (the controller was tuned) based on system response after the equipment was operating.

There were three nested controllers used. Control valve (FCV-1) position was fed back through a proportional-only controller to mitigate valve load characteristics. Salt flow rate was fed back through a proportional and integral controller to obtain good correspondence between desired salt flow rate and actual salt flow rate. The integral term was used to eliminate any steady state salt flow rate error while sending a non-zero valve position signal to the valve controller. The third loop feeds back receiver outlet salt temperature through a proportional, integral, and derivative controller. Again, integration is used to reduce the steady state temperature error. The derivative term was added to stabilize the loop.

The salt cooler analog control system was much simpler than the receiver analog control system. A single PID controller was used for each fan. The output of each controller was fed to a pneumatic motor that set the fan blade pitch angle. Both controllers used the same cooler outlet salt temperature and the same temperature set point. Separate controllers were used for redundancy.

Representative transient response data for the receiver analog control system is shown in Figures IV-14 for receiver outlet salt temperature. The first 16 minutes show the response to a 28°C (50°F) decrease in receiver outlet temperature setpoint. The second disturbance was a 25% decrease in solar power input to the receiver. During this second response, the receiver temperature oscillates about the desired set point. The initial temperature undershoot was 33°C (60°F), a deviation that is too large for a commercial receiver. The third disturbance, at 41 minutes, was a 25% increase in the solar power input to the receiver. When the receiver outlet temperature reached 574°C (1065°F) control was returned to manual and the salt flow rate was increased significantly. As the receiver outlet salt temperature decreased, the salt flow rate was manually brought back to the normal level.

Generally it can be concluded that the analog system used for receiver control left much to be desired. It is certainly possible to improve analog control through elimination of unnecessary time lags, using intermediate factors to reduce the effect of salt flow rate on receiver gain, but it seems doubtful that cloud cover effects can be properly controlled.

3. Algorithm Control

The term "algorithm" is used only because the computations and logic were to be processed in a digital computer. The algorithm control system used the CRTF data system to collect and process measured data and then used the CRTF RTAF computer to perform the control calculations to obtain a salt flow rate. The desired salt flow rate was sent back over CRTF lines for decoding and input to the SRE receiver.

As the CRTF data collection and computing systems have other priorities (e.g., heliostat scram), the algorithm computations involved some time delays. Two related, but different, control algorithms were used. The first, called the energy balance approach, used measurements of receiver temperatures and salt mass flow rate to calculate the energy being absorbed by the receiver. The desired steady state salt flow rate is then computed based on calculated absorbed energy and desired temperature gain. This value of desired steady state salt flow rate is sent to the test receiver. The second algorithm, called the ramp rate approach, starts out like the Energy Balance approach up to the point of computing a desired steady state salt flow rate. The ramp rate approach sends enough of the desired steady state salt flow rate change in each computation interval so that the total effect will be accomplished in a selected time interval called the ramp time. For most test data cases the ramp time was 20 seconds. An algorithm for air cooler control was mathematically developed but never implemented in software because the analog control worked very well.

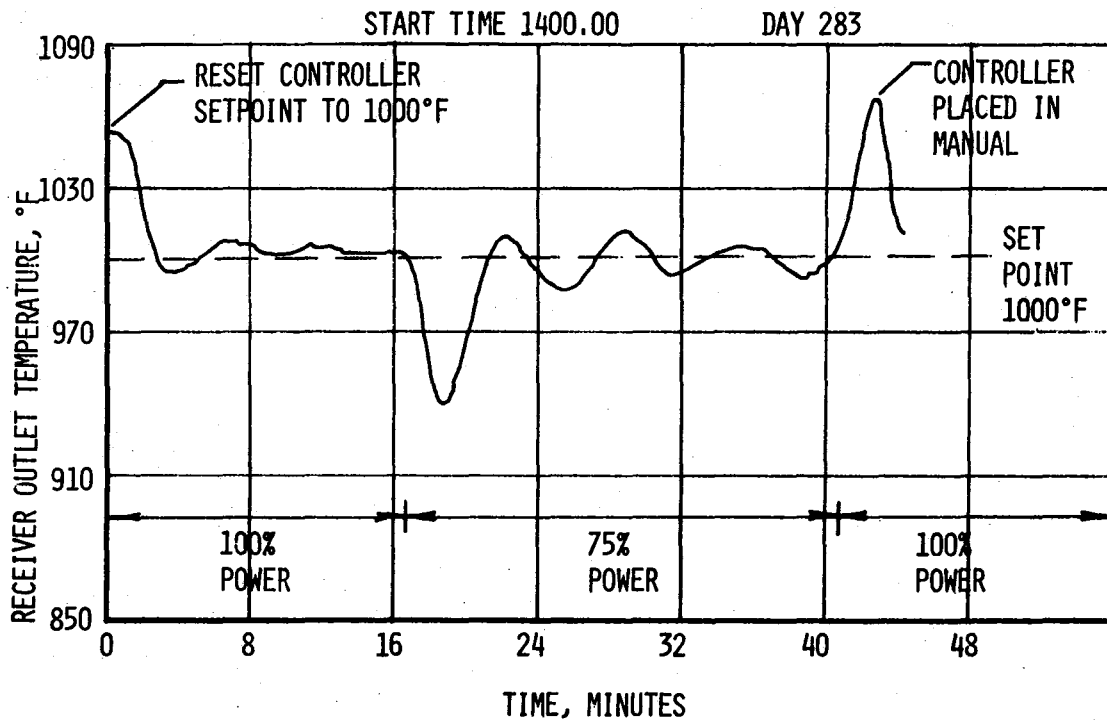


Figure IV-14 Analog Receiver Control - Outlet Temperatures

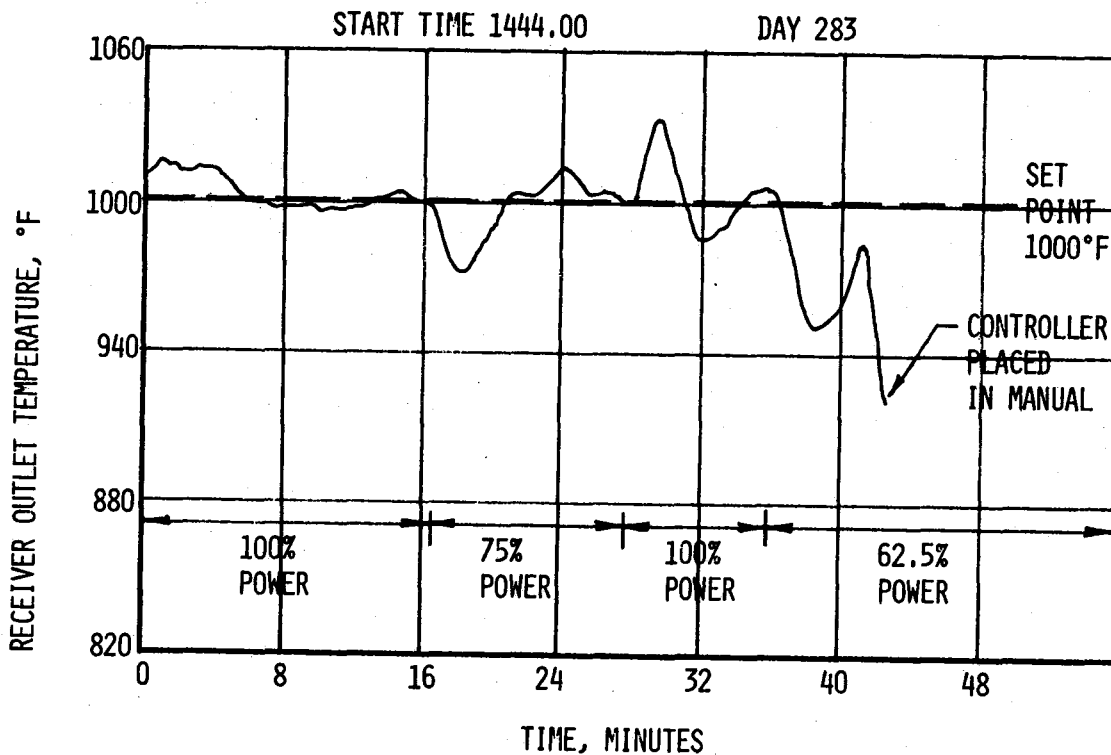


Figure IV-15 Computer Algorithm Control - Outlet Temperatures

Representative transient response data for the receiver ramp rate algorithm control is shown in Figures IV-15 for receiver outlet temperature. The first 17 minutes of the record are for constant solar power input at 100% level. The period between 17 minutes and 27 minutes represents the response to a 25% decrease in solar power. The 16°C (28°F) deviation in receiver outlet temperature is less than half of the temperature deviation for a comparable disturbance when under analog control. At the 40 minute point, control was switched to manual with a sharp decrease in salt flow rate and then an even sharper increase in salt flow rate to a level consistent with 85 to 90% of maximum solar power. As the solar power input was only at 62.5% of maximum, the salt outlet temperature started to decrease starting at 41 minutes. It appears that algorithm control is better than analog control for solar power step changes between 100 and 75% of maximum solar power. However, algorithm control was lost for larger steps in solar power. The temperature deviations were larger than a desired $\pm 6^{\circ}\text{C}$ ($\pm 10^{\circ}\text{F}$) and greater system damping is desirable so that the system will accept successive disturbances.

4. Control Simulations

As part of the ongoing Martin Marietta solar system development work, a receiver control system analysis was started. In particular, a computerized model of a multi-panel molten salt receiver was built. It was decided to modify the receiver model to represent the SRE receiver and the algorithm control with ramp rate. The new model would then be exercised to determine if there were any major deficiencies in the SRE receiver or the control algorithm. It was found that the simulation was a reasonable representation of the SRE receiver, and that the algorithm control could be used for further testing. A block diagram of the simulation is shown in Figure IV-16.

Several simulation runs were made with input conditions that were expected to result in good correspondence between the SRE and simulation data. All of the simulation runs for steps in salt flow rate that were run with the correct input conditions resulted in good correspondence between the simulation and SRE data. An example is shown in Figure IV-17. The lower two curves are the SRE salt flow and the representation of that salt flow used in the simulation. The upper two curves show the response of header 19 temperature.

5. Experience with Modified SRE Receiver Algorithm

In parallel with the verifications of the simulation model, it was decided to modify the SRE receiver control algorithm. The most important parts of the change were to use a different set of multiplexers and to use absorber tube temperature thermocouples instead of interconnecting header temperature thermocouples. These modifications decreased the computation and measurement delays. The result has been a significant improvement in controlled response. A representative flux transient is shown in Figure IV-18. Power was reduced from to 100% to 37-1/2% and then increased to 100%. The

receiver outlet temperature is controlled with a maximum deviation from set point of 18°C (32°F). (However, it must be noted that 1) the front tube surface temperature reached 682°C (1260°F), prompting a switch to manual control, and 2) the tube temperature would have gone higher had it not been for the unintentional delay in adding the last 12.5% of the heliostats.) The low frequency variation is due to the use of manual control on the salt cooler. As the size of the flux steps was increased, it became increasingly difficult to control the salt cooler manually.

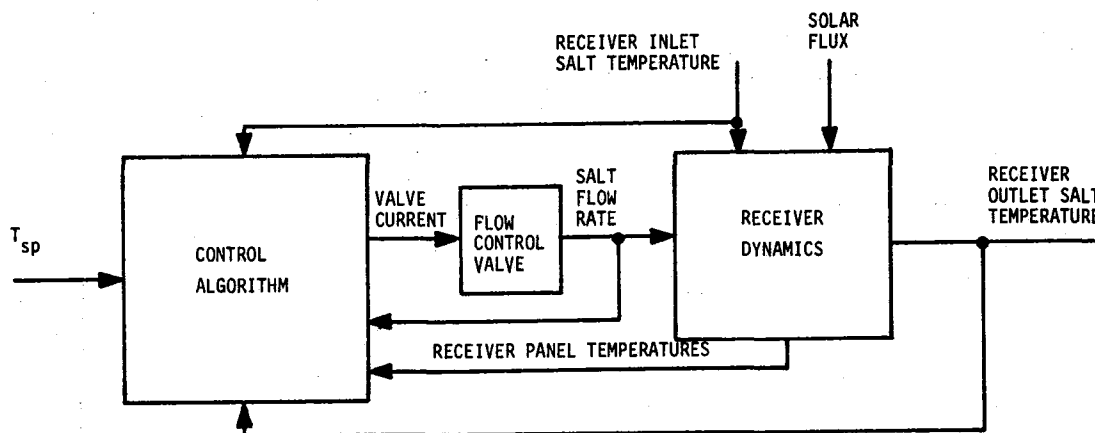


figure IV-16 Block Diagram for Receiver Control Simulation

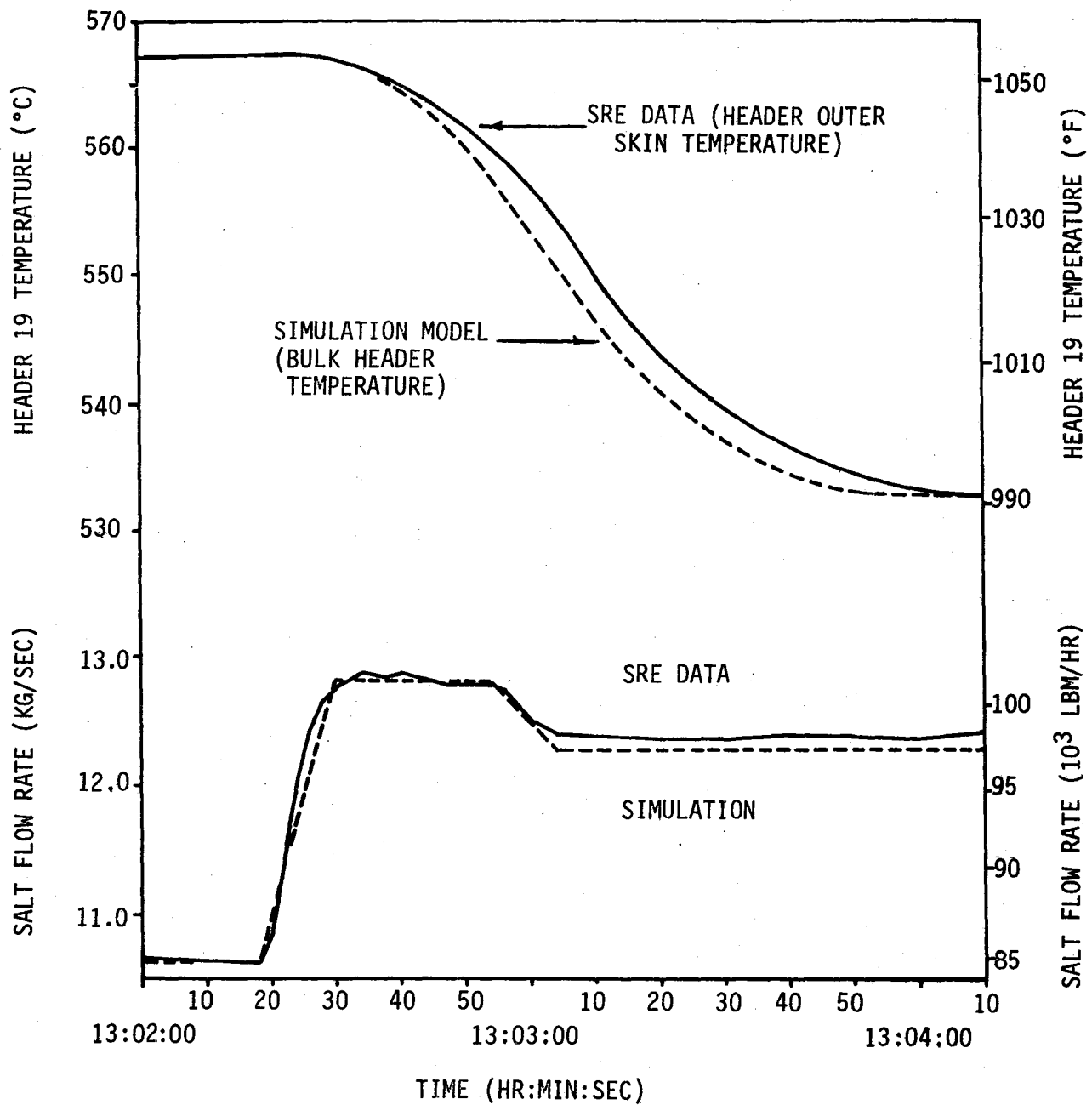


Figure IV-17 Temperature Response to Step in Salt Flow Rate

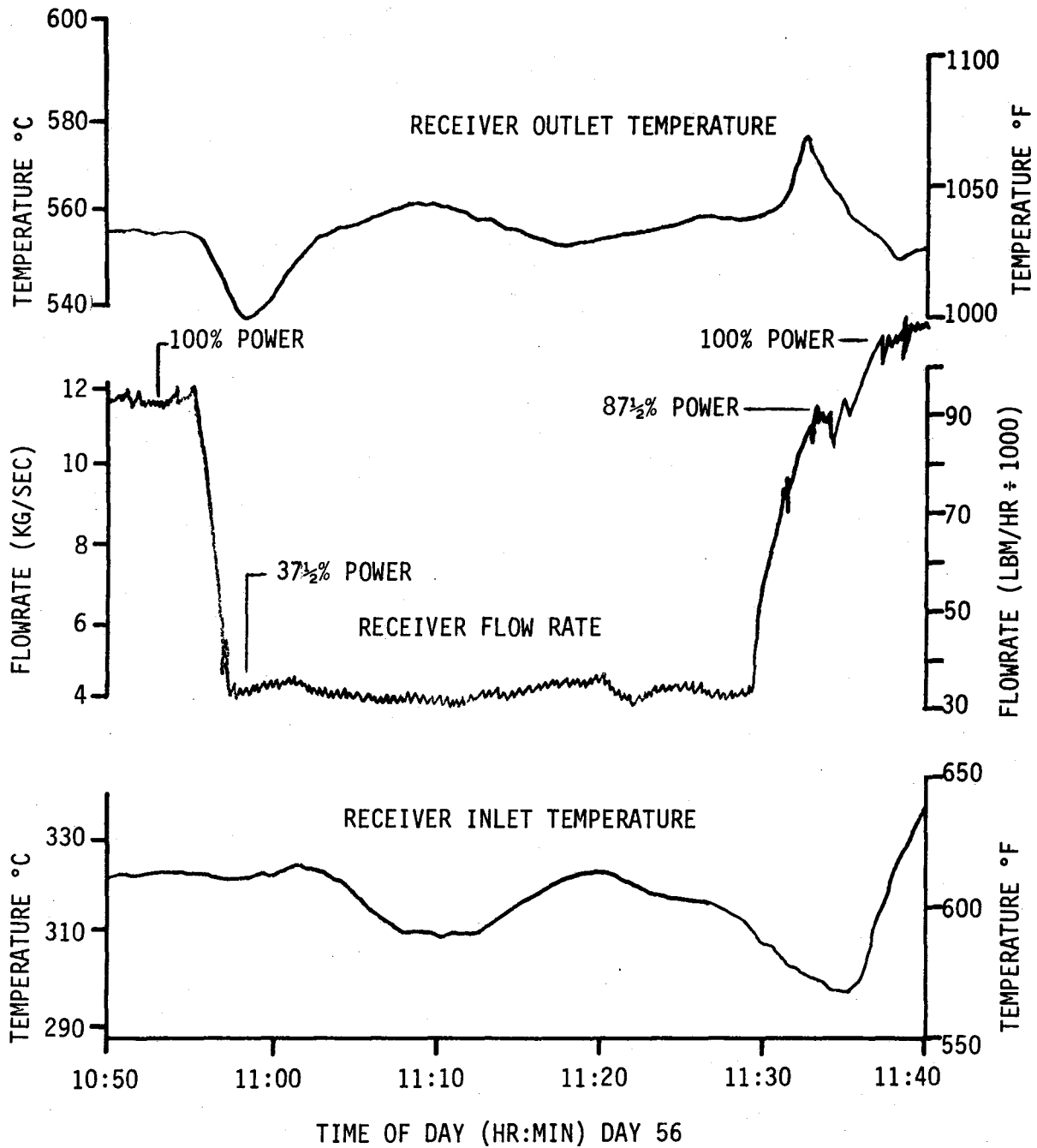


Figure IV-18 Modified Algorithm Response to Flux Transient

In addition to the ability to handle up to 67-1/2% step changes in flux, the modified algorithm also controlled the receiver well on days with intermittent cloud cover. A fifteen percent drop in flux due to clouds resulted in a deviation of less than 3°C (6°F) in receiver outlet temperature. During one cloud disturbance, the control algorithm was able to maintain control while reducing salt flow to the minimum limit and then back up to a normal level again as the clouds went away. The modified algorithm is thus adequate for the range of variations in cloud cover that have been experienced.

6. Recommendations

The following recommendations are made:

- a) Sampling and computation lags should be reduced by use of alternative multiplexers at CRTF and by modification of the algorithms.
- b) The algorithm should be modified to avoid use of tube temperatures and to reduce the number of header temperatures involved.
- c) Sensing element time lags should be avoided or reduced.
- d) The algorithm gains should be made functions of salt flow rates.
- e) Further analyses should be conducted to obtain an understanding of why the receiver outlet temperature responds differently to flow and flux changes.
- f) The simulation activity should be expanded to alternative control laws and to examine the effects of various cloud transients.

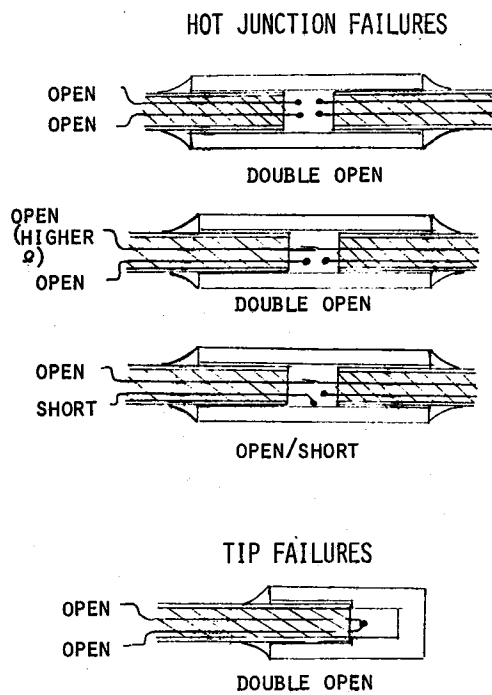
E. HARDWARE RELIABILITY

In general, the system performed very well with a minimum number of problems. All of the components and subsystems through which salt flowed remained leak-free throughout the program. There were some subsystem problems that caused delays during buildup and checkout but never for more than a few days at a time. Most of the subsystem problems which occurred during test operations were fixed on a non-interference basis with testing. The following paragraphs outline most serious of the system hardware problems and the approach taken toward solving them.

1. Trace Heaters

The trace heating system produced by far the greatest number of operational hardware problems and were the most serious in nature. Heater failures started to occur almost immediately when power was first applied to them. The failure modes are shown in Figure IV-19.

The small diameter heater wires were not made from nichrome wire and that was causing them to break down at operating temperature, particularly in the tips and hot junctions. After the small diameter



FAILURE %	
HOT TRANSITIONS	75%
TIP	15%
RANDOM	10%

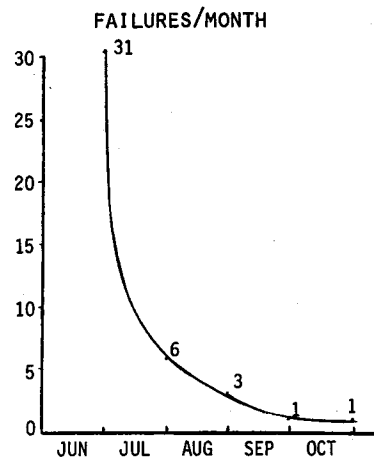


Figure IV-19 Trace Heater Failure Modes and Failure Rate

heaters were replaced with ones made from nichrome wire and of single-conductor construction, the failure rate dropped off dramatically and took on somewhat of a random pattern.

It was discovered that some form of vapor was being driven off of the paste flux used to solder the electrical connections. The vapor was getting into the magnesium oxide powder and causing a partial breakdown of its insulating properties. Accordingly, all heater repairs since then were done with semi-dry flux and successful repairs resulted in every case.

It was also discovered that the hot junctions on the trace heaters did not have an adequate heat sink, so steps were taken to provide air cooling of those joint through "tunnels" in the insulation.

2. System Welds

All welding in the system was done manually and all welders were certified to ASME. The welded system was soap-bubble leak-checked at 390 and 714 kPa (60 and 110 psig) and several weld leaks were found. After these leaks were repaired, the system was pressurized to 1624 kPa (250 psig) and found to be leak-free.

The tube-to-tube welds (3500 total welds) on the front and back side of the receiver were all manual TIG (tungsten inert gas) welds. Throughout the course of the program the receiver was inspected on an almost daily basis for new weld failures. There were 60 front-side weld failures and some unknown number of back-side weld failures; The total estimated number was between 60 and 100 weld failures, or less than 3% of the total.

3. Receiver Paint

After its arrival at CRTF the receiver was cleaned and painted with two coats of Prymark 2500 black paint. No attempt was made to cure the paint until the salt checkout tests at ground level. These tests provided several hours of bakeout at temperatures around 316°C (600°F). Just after the salt checkout tests at ground level, some crazing of the paint was evident in the upper right corner of the receiver. The loose paint was brushed off and new paint was applied with a brush.

About a week after solar testing had started there was more evidence of paint deterioration in the form of crazing and flaking. This deterioration spread very quickly across the face of the receiver and took on an oxidized appearance. By mid-September the situation had not deteriorated any further, so all the loose paint was removed, the tubes were cleaned, and new paint was applied with a brush. The new paint was immediately baked out by using the heliostats for the correct length of time and at the proper temperature. The newly-painted areas as well as the areas which were not repainted held up well from this point on and by the end of the program there was only a slight discoloration of the painted surface.

4. Air Cooler and Cavity Doors

Both of these door assemblies experienced problems due to thermal distortion. Manual assistance for both doors was used extensively throughout the program.

The cavity doors were subjected to unexpected heating due to spillage around the aperture. This area was to have been protected by the RTAF assembly, but it was not mounted on the cavity until later in the program. The doors were moved by cables from air cylinders and were on rollers that moved back and forth in a deep channel. When parts of the system expanded, friction developed between the rollers and the channel. Some manual assistance was required to overcome this problem. The worst problem was that the doors would not open without manual assistance after having been closed with the receiver hot because the heat from the receiver would cause the door panels to bow inward and jam in their channels. We recommend that in future designs the doors be designed to be less rigid, with more room for thermal expansion to prevent excessive warpage. Better shielding from heliostat spillage when the doors are open, and a counterweight system to help counter balance the door should also be considered.

5. Flux Gages

The fragileness of the flux gages was not given proper consideration during the design of the system, and several of them were damaged upon installation because of interference with the support structure and fluid lines. Flux gages are not recommended for use in commercial receivers.

V. COMMERCIAL RECEIVER DESIGN UPDATE

Commercial-scale conceptual designs of molten salt solar receivers were presented in two recent studies: "Saguaro Power Plant Solar Repowering"¹, and "Solar Central Receiver Hybrid System"². The purpose of this design update was to provide further refinements to the design approach represented by these two studies, and to re-evaluate them in the light of the results of the receiver SRE build and test program.

A. MODULARITY STUDY

The reference studies have indicated that the optimum (economic) size of a solar power system (constrained by factors such as atmospheric attenuation, length of cabling and piping, tower height, etc.) is from 300 to 400 MW thermal; power plants larger than these should be built in modules, preferably with a common storage facility. For example, a 300-MWe (net), 12-hour storage solar power plant requires 1800 MW solar thermal output, or 5 to 6 modules.

The result of the module optimization study is shown in Figure V-1, in the form of energy cost vs. plant size, with number of modules as a parameter. The preferred module size for the Saguaro Power Plant study, as well as for the present study, is 315 MWth (net output) with four-cavity molten salt receivers. There are 10,500 heliostats per module field. Each heliostat has 49.02 m² (528 ft²) of reflective surface area and the total collected energy delivered to the receiver is 342 MWth with a receiver efficiency of 92%.

B. CONTROL ZONE OPTIMIZATION

The parameters analyzed to find the optimum zone configuration were the average receiver film coefficient, the average fluid velocity, and the receiver pressure drop. For each zone configuration, the parameters were plotted against the physical receiver characteristics (the number of tubes per pass and the number of passes). From these plots an "optimum" design was chosen for further analysis. Optimization was performed by choosing the design with the best compromise between film coefficient and pressure drop. One-, two-, four-, and eight-control zone configurations were examined.

The four-zone configuration shown in Figure V-2 was selected as the preferred configuration. The criteria for this selection included: (1) minimizing tube metal peak temperatures by designing for lower peak

-
1. Saguaro Power Plant Solar Repowering Project, Final Technical Report, Contract DE-AC03-79SF10739, July 1980.
 2. Solar Central Receiver Hybrid Power System, Final Technical Report, Contract DE-AC03-78ET21038, September 1979.

MODULARITY ANALYSIS

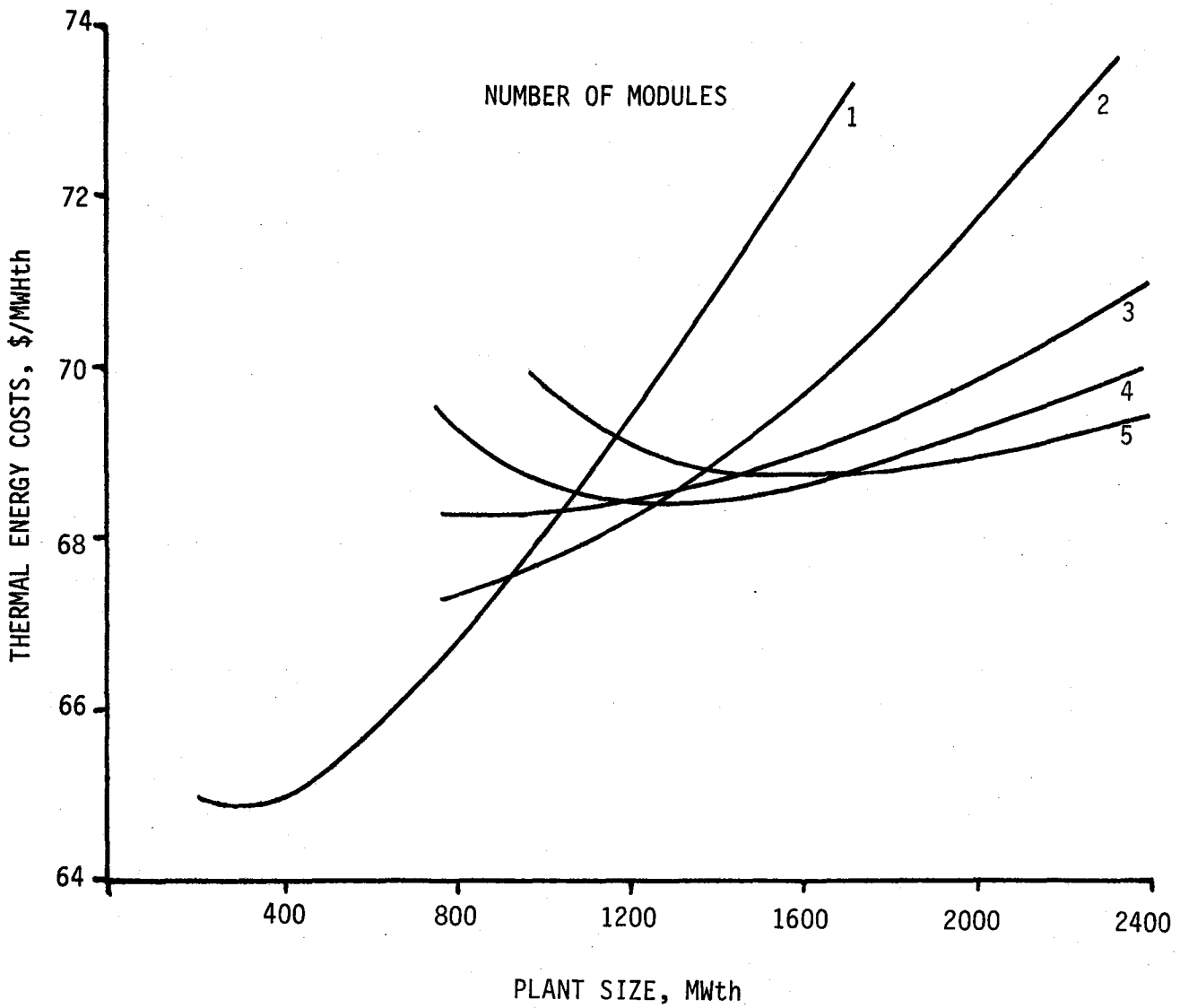
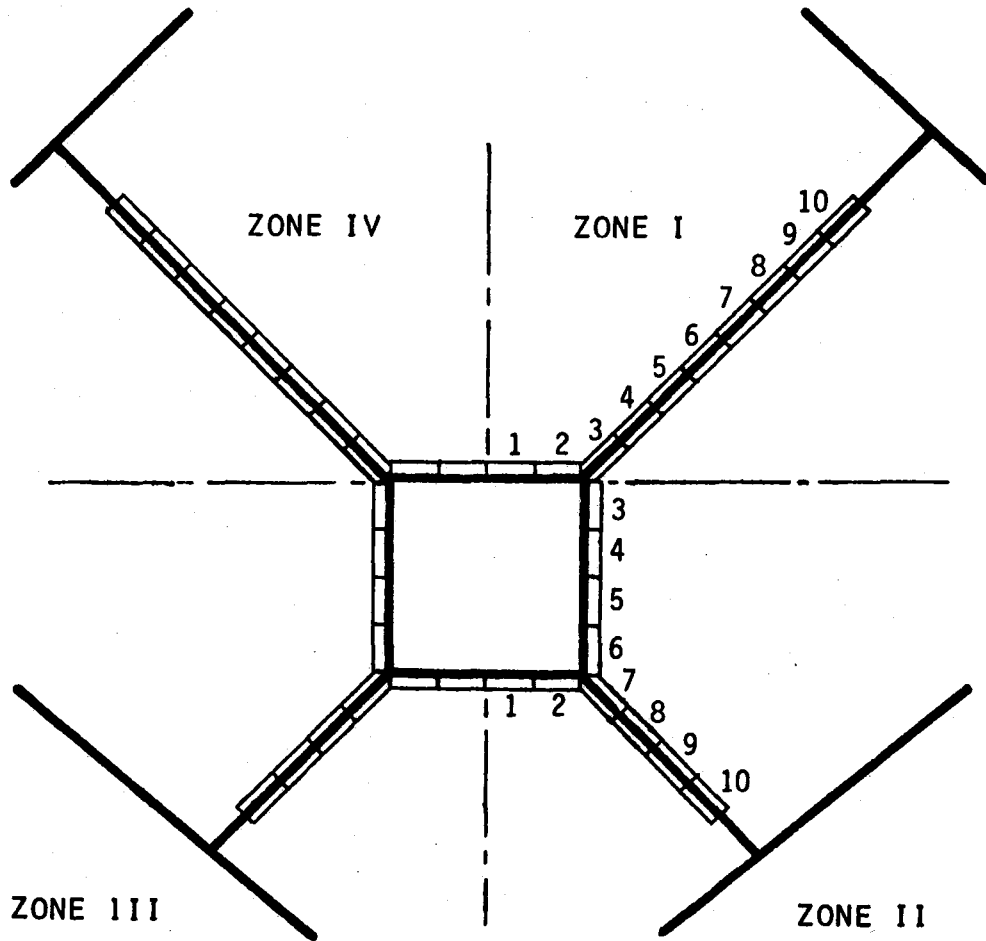


Figure V-1 Receiver Modularity Analysis



ZONES: I, IV

24 TUBES PER PASS

10 PASSES

5.08 cm (2.0 in.) OD,

4.65 cm (1.83 in.) ID

ZONES: II, III

32 TUBES PER PASS

10 PASSES

3.81 cm (1.5 in.) OD,

3.48 cm (1.37 in.) ID

Figure V-2 Preferred Receiver Configuration

fluxes, and thereby maximizing creep-fatigue life; (2) minimizing tube-to-tube temperature gradients within a single pass, by reducing the number of tubes within a pass; and (3) providing an optimum trade-off between operation and requirements during cloudy conditions and the number of control zones required to implement such conditions. Note that this configuration requires two different tube sizes to optimize performance.

C. DETAILED ANALYSIS OF PREFERRED CONFIGURATION

1. Cavity Design

The aperture size, shape, and cavity depth for the Saguaro receiver were determined using the TRASYS program. The field was divided into north, south, east, and west quadrants, and separate TRASYS models were constructed for each quadrant. Figure V-3 shows the TRASYS-generated plots depicting the north, east, and south cavities of the receiver. (Because of symmetry the west cavity is excluded.)

2. Detailed Flux Maps

Martin Marietta's TRASYS computer program was used to develop flux distributions on the receiver surfaces on a per-pass basis.

TRASYS runs were made for the design point day 172, solar noon, and for the peak input point of each cavity. North cavity peak point is on day 356, solar noon; west and east cavity peak points are on day 172, two hours before and after solar noon, respectively; south peak point is the same as design point, day 172, solar noon. The total heat input through the aperture is 130.6 MWth for the north cavity at the design point. The percentage of energy which actually passes through the aperture is the aperture efficiency. This efficiency is 98.5% for the north aperture (assuming a field-average atmospheric attenuation of 0.935). The east and west cavity input is 81.9 MWth each with an aperture efficiency of 98.5% (design point). The power input for the south aperture is 45.3 MWth and has an aperture efficiency of 98.9% for the design point.

3. Salt and Tube Temperature Profiles

A MITAS thermal computer model was constructed to calculate the salt and absorber tube steady-state temperature profiles in the receiver passes. One absorber tube per pass was modeled to represent all of the tubes in that pass. This representative tube was divided into segments containing front and back outside surface nodes, front and back inside tube surface nodes, and a salt node. The incident flux on the front and back outside tubes was input directly from the TRASYS detailed flux maps. These fluxes were divided into ten segments per pass, the same as the thermal math model.

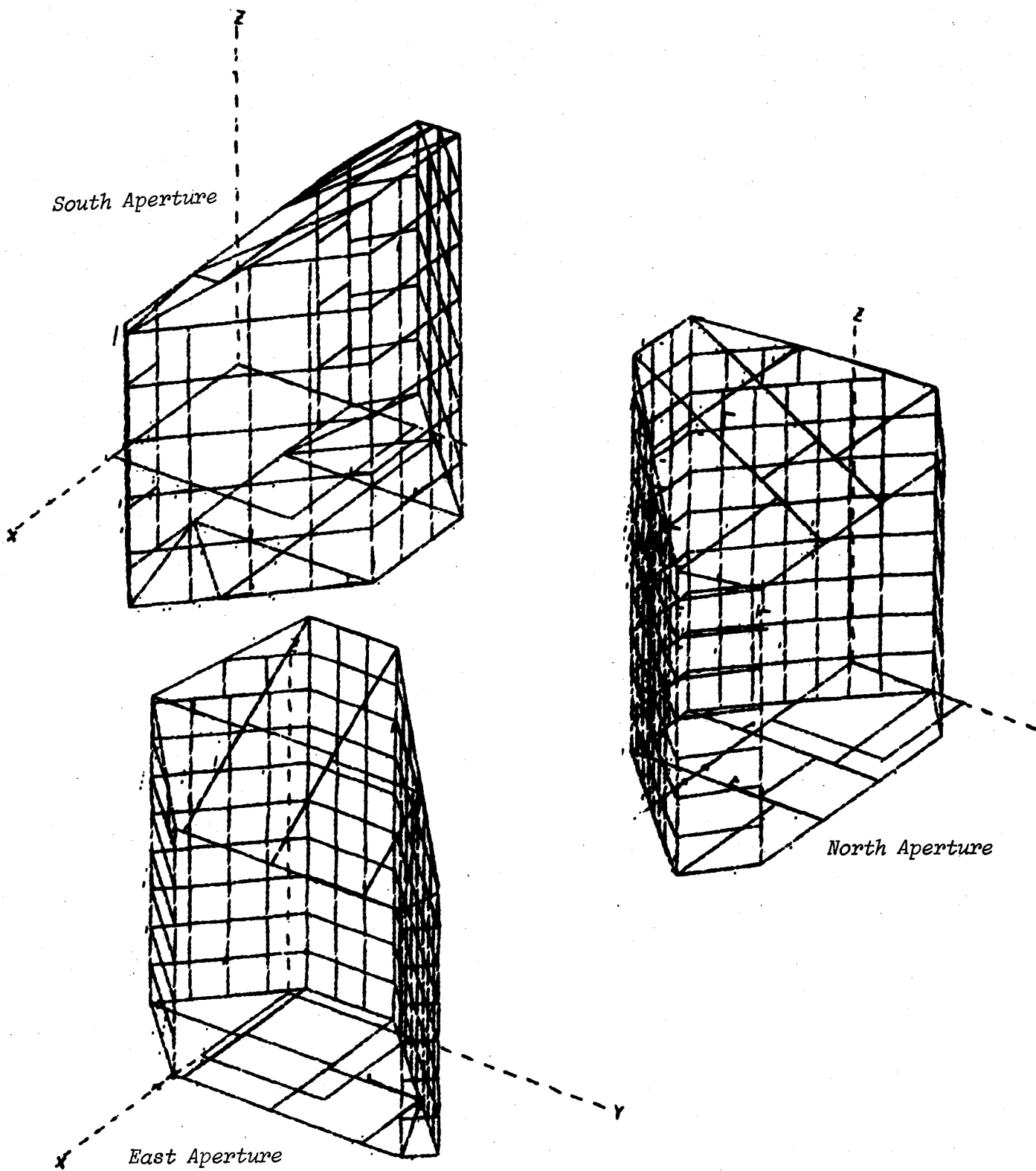


Figure V-3 Cavity Layout

The peak tube metal temperature for the northeast zone (Zone I) is 598°C (1108°F) on pass number eight where the salt temperature is 530°C (986°F) (refer to Figure V-2 for pass designation). The peak tube metal temperature for the southeast zone (Zone II) is 589°C (1092°F). This occurs on pass number ten where the salt temperature is 563°C (1046°F). All of the temperature profiles are well within acceptable limits of design.

4. Tube-to-Tube Temperature Gradients

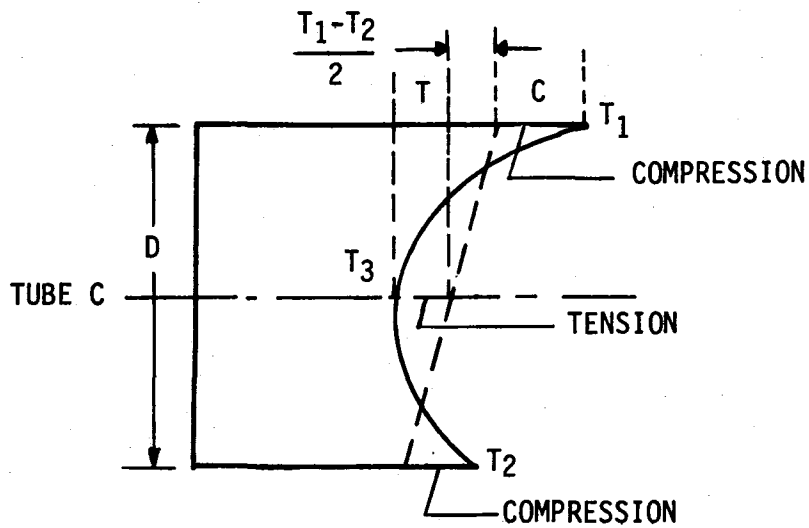
In our commercial design, the pass width is 1.2 m (4 ft), which is one tenth of the exposed area for that zone. Analyses performed during the present study indicate that the greatest temperature difference between adjacent tubes in a pass is 12°C (21°F). By plotting the power per pass versus pass number, the highest variations in power were determined. Only the passes with flux on both the front and back tubes were plotted as the passes with one-sided fluxes are at lower temperatures and present no problems. Based on the varying power levels, calculation were made of the maximum and minimum salt outlet temperatures for the three worst locations on the receiver: pass numbers eight (8), nine (9), and ten (10). Zone I, the north east zone, was the zone analyzed because the power variations are the greatest. The maximum, minimum, and average salt outlet temperatures for these three passes are presented in Table V-1. This investigation shows that no problem with high single tube temperatures exists.

5. Stress Considerations

The analysis of the commercial receiver design considered the same major stress contributors as the SRE design:

- 1) The non-linear temperature gradient across the tube cross-section;
- 2) The front-to-back temperature differentials; and
- 3) The bending due to wind loads and the shadowing effect of the lateral support tubes.

The two most critical locations which were evaluated in detail were the northeast Zone #1 and the southeast Zone #2. The typical temperature distribution across tubes away from the shadowing of the lateral support tubes is illustrated in Figure V-4. The approximate maximum induced compression stress is derived on the figure using the neutral axis tensile stress as 60% of the maximum compression. In locations where the lateral support shadows the tubes, $T_2 = T_3$. From the equation for the maximum compression stress it can be seen that as T_2 decreases (approaches T_3), the maximum compression stress will decrease. The maximum wall temperature at the critical location in the northeast Zone #1 is 580°C (1076°F). Using the total stress combination of 266 MPa (38,600 psi) a minimum margin of safety of 0.30 results. A combined creep-damage ratio of 0.385 was calculated, well below an allowable ratio of 1.0. The analysis of the southeast Zone #2 showed higher load bending stresses due to wind and bending introduced by the differential front-to-back face temperatures. The worst



o UNRESTRAINED ANGLE OF ROTATION $\approx \frac{\alpha(T_1-T_2)}{D}$

o FROM THE FIGURE:

$$T_1 - C - \left(\frac{T_1-T_2}{2}\right) - T = T_3$$

Using $T = .6C$

$$T_1 - C - .5T_1 + .5T_2 - .6C = T_3$$

$$- 1.6C = T_3 - .5T_2 - .5T_1$$

$$C = .312 (T_1-T_2) - .625 T_3$$

∴ MAX COMPRESSION STRESS $\approx \alpha E [.312(T_1+T_2) - .625T_3]$

Figure V-4 Stress Considerations

Table V-1 Tube-to-Tube Salt Temperatures

TABLE V.D.4.1			
SALT TEMPERATURES			
	T Inlet °C (°F)		T. Outlet °C (°F)
Pass #8	514 (958)	Max.	547 (1017)
		Min.	536 (996)
		Ave.	542 (1008)
Pass #9	542 (1008)	Max.	563 (1046)
		Min.	553 (1028)
		Ave.	558 (1037)
Pass #10	558 (1037)	Max.	569 (1057)
		Min.	561 (1041)
		Ave.	566 (1050)

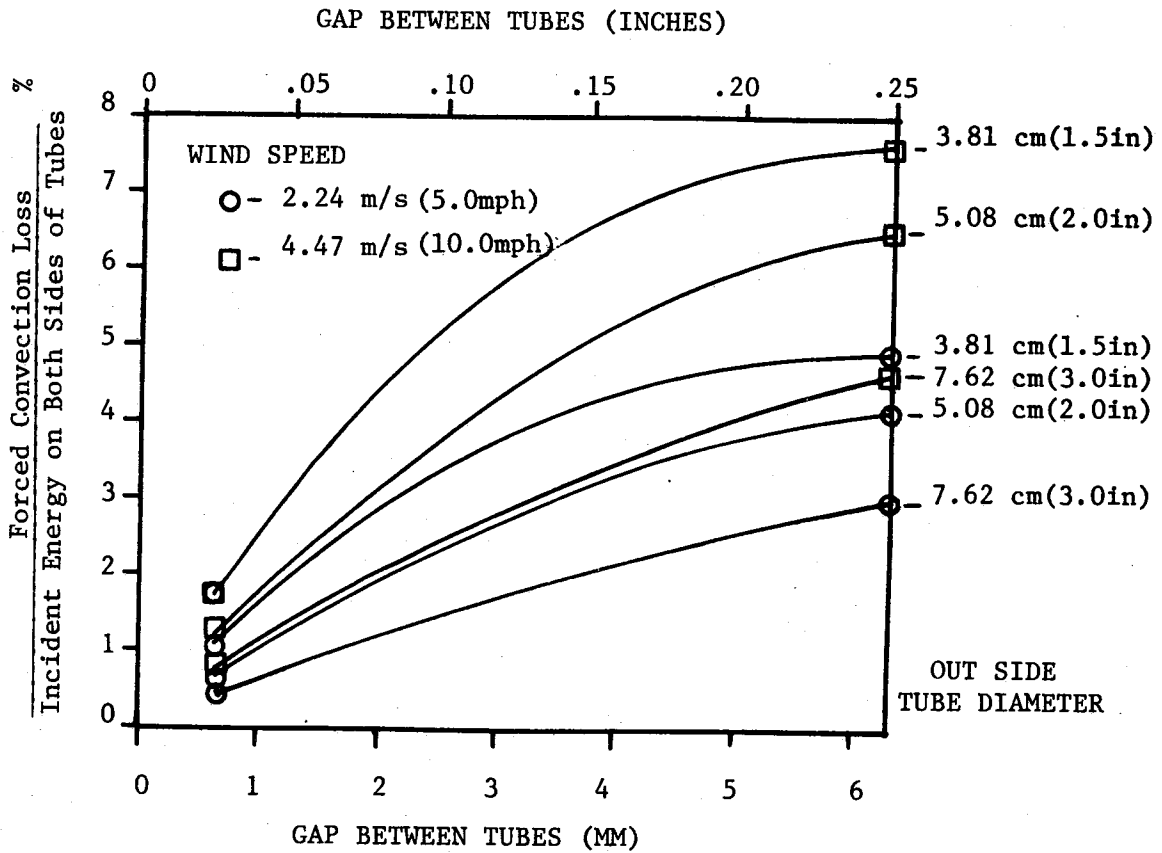


Figure V-5 Percent Convection Loss Curve

condition occurs at a location of maximum face temperature of 420°C (789°F) which has a higher basic material allowable than for the 580°C (1076°F) location the calculated margin of safety was 0.31 for the maximum combined stress of 294 MPa (42,700 psi). This stress at a maximum temperature of 420°C (789°F) presents no creep-fatigue problem.

The analysis of the lateral support tube itself showed relatively high induced stresses due to a non-linear temperature distribution across the tube cross section. Differentials as high as 143°C (290°F) occur between the fluid temperature and the front face of the support tube.

This situation could be alleviated by painting the support white instead of black. The out-of-plane deflections (and resultant induced stresses) are a function of the complex interaction of the lateral supports and the vertical tubes stiffnesses and temperature differential distributions; however, the analysis done to date shows no significant problems.

6. Special Studies

a. Convection loss through tube gaps - In cavity receiver designs for commercial application there is a heat loss due to wind blowing through tube gaps. For a multi-cavity design the tubes which are illuminated on both sides will have air flow through the tube gaps under most conditions. For example, a north wind would enter through the north cavity aperture and then pass through the gaps in the absorber panels on the northwest and northeast.

The results of this study are given in Figure V-5. Here the percent loss is expressed as a function of tube gap, tube diameter, and free stream wind velocity. It is interesting to note that as the tube diameter increases the percent loss decreases. Even though the analysis is somewhat conservative, the results indicate that the loss due to flow through the tube gaps is significant and must not be overlooked in designing a commercial receiver.

b. Lateral support tube section thermal analysis - A lateral tube support technique was analyzed to determine stress-related problems. A MITAS program was used to determine the temperature profile for this support tube. The detailed analysis included lateral heat conduction as well as conductors to the molten salt coolant. Parametric analyses with flux levels comparable to the worst conditions of the commercial design were performed. A stress analysis based on this temperature distribution indicated stress levels that were too high to assure acceptable receiver life. A possible solution to this problem would be to paint the absorber white to decrease the temperatures along the support. Future analyses will consider alternative lateral support designs.

D. COMPARISON WITH SRE RESULTS

Efficiencies - The predicted thermal efficiency of the commercial receiver at the design point is 92%. This compares with 85.3% determined for the SRE by the input-loss method. The difference is believed to be primarily due to the more unfavorable incident flux distribution inside the SRE cavity when compared to its full-scale counterpart. That fraction of solar input incident on non-active surfaces in the SRE is approximately 13%, compared to 2.2% for the north cavity, 3.0% each for the east and west cavities, and 3.1% for the south cavity of the commercial receiver at the design point (day 172 at noon). This argument is substantiated by the fact that a 6% increase in efficiency was noted when the aim point was moved inside the cavity during the hi-flux tests (resulting in less flux on the non-active surfaces). Also, 3% of the incident solar energy is reflected and lost from the aperture due to the sharp flux incidence angles on the SRE; this loss will not exist in a commercial receiver.

Thermo-structural considerations - The SRE experience indicates that tubes and headers on adjacent passes should not be welded together in order to minimize stresses due to temperature differentials between passes. More extensive use of non-linear finite element modeling, and test evaluation of combined creep and fatigue damage are recommended.

Operational considerations - Draining by gravity is adequate. Warm-up of the receiver tubes by heliostats is not recommended; other approaches, such as salt recirculation, should be investigated. The feasibility of rapid rampup of power (with maximum salt flow) has been shown. In establishing control strategies for commercial receivers, consideration should be given to the effect of cloud transients on the life expectancy of the receiver.

Development status - There were no major unresolved problems discovered during the SRE program; full-scale demonstration appears to be the next logical step in the development of molten salt solar receiver technology.

VI. DESCRIPTIONS OF MATERIAL COMPATIBILITY AND SALT CHEMISTRY TESTS

This chapter contains descriptions of each of the tests conducted during the Phase II Alternate Central Receiver Program. The test program was divided into four areas of investigation: compatibility of materials with molten salt, mechanical properties of salt-immersed materials, dynamic testing of materials in flowing molten salt, and salt chemistry. The results of each test, as well as a discussion and conclusions, may be found in Chapter VII.

A. MATERIALS IMMERSION TESTS

1. Trace Contaminants Effects Test

The purpose of this test was to gain a better understanding of corrosion effects for trace amounts of anionic contaminants present in commercial nitrate salt. Such tests indicate if there is a need to control certain impurities in the commercial-grade salts.

Test coupons were suspended in reagent-grade molten salt (60% NaNO₃, 40% KNO₃) that had been doped with the maximum concentrations of chloride ion, sulfate ion, hydroxide ion, and carbonate ion specified for commercial salt.

A test matrix for the trace contaminants tests is shown in Table VI-1. Each test vessel contained three welded sample coupons and three regular coupons. Coupons were removed every 1000 hours for weighing and examination. Salt and dopant were replaced with a new solution 2000 hours into the test. Salt samples were analyzed for anion concentration at 2000 and 4000 hours.

Table VI-1 Trace Contaminants Test Matrix

Temperature Sample		593°C	593°C	593°C	593°C	399°C
		Incoloy 800	RA330	316L SS	347 SS	A516
Dopant	Wt %					
NaOH	0.50	X	X	X	X	X
Na ₂ CO ₃	0.20	X	X	X	X	X
Na ₂ SO ₄	0.35	X	X	X	X	X
NaCl	0.25	X	X	X	X	X
NaCl	0.50	X				X
Blank	--	X	X	X	X	X
All of above		X	X	X	X	X

X Three with Welds and Three Without.

2. Extended Immersion Tests

These on-going tests evaluate selected construction materials under longer periods of molten salt exposure than was possible in Phase I. Selected sample coupons from Phase I testing were exposed for an additional twelve months to molten salt. Weight-change data was collected every 2000 hours, and the coupons were microsectioned and optically analyzed at the end of the test.

The test matrix is shown in Table VI-2.

Table VI-2 Extended Immersion Test Matrix

Alloy	Test Hours	Temperature	
	Phase I	Phase I	Phase II
I-800	5500	593 C (1100°F)	579 C (1075°F)
RA 330	2300	593 C (1100°F)	579 C (1075°F)
SS 347	2000	593 C (1100°F)	579 C (1075°F)
SS 316	9600	621 C (1150°F)	579 C (1075°F)
A516	7200	399 C (750°F)	399 C (750°F)

3. Surface Preparation Effects Test

This test was done to characterize the nature and degree of metallic oxidation on carbon and low alloy steel specimens immersed in molten salt as a function of their surface condition.

Four carbon steel test coupons were used in this test. On each coupon, one face was surface machined, leaving the opposite face in the as-received (rolled) condition. Six A387 alloy test coupons were machined on both faces. Alloy coupons were suspended from nichrome wire into molten salt at 399°C (750°F) and exposed for 1000 hours. After removal, the coupons were weighed, and surfaces were studied, with particular attention paid to the coating condition and thickness.

4. Special Purpose Materials Immersion Tests

The objective of these immersion tests was to determine the compatibility of limited-use materials like seals, gaskets, packing, and valve trim with molten salt.

Selected seal, gasket, and packing materials were suspended from nichrome wire into Incoloy 800 trays containing molten salt. The temperature of the test oven was maintained at 399°C (750°F). Materials were weighed periodically and were examined visually after each 1000 hours of test. Materials were exposed to the molten salt environment for a total time of 5000 hours.

Table VI-3 is a list of the materials tested.

Table VI-3 Special Purpose Materials Tested

Gasket Material

- Crane IX 187

Valve Trim and Seals

- Stellite #6
- Tungsten Carbide, Co Binder
- Tungsten Carbide, Ni Binder
- Silicon Carbide
- Mica Asbestos Valve Stem
- Asbestos with Rubber Binder

Packings

- Aluminum, Crane 100 Al
- Copper, Crane 100 Cu
- Graphite, Crane GF
- Nickel, Crane 100 Ni

B. MECHANICAL PROPERTIES OF MATERIALS IN MOLTEN SALT

1. Intergranular Corrosion/Tensile Tests

The purpose of these tests was to assess the susceptibility of candidate materials to intergranular corrosion. Tensile specimens (both parent metal [PM] and weld) were placed in trays of salt in a test oven at 593°C (1100°F). An equal number of samples (both PM and weld) were held at 593°C in air for reference testing at the end of the tests. Three salt-immersed PM samples of each alloy and three each of the air samples were removed from test after 6 months and exposed to ASTM A262 accelerated intergranular corrosion (IGC) solution before analyzing. The rest of the samples remained in test for a total of 12 months. Table VI-4 is a list of the materials tested.

Table VI-4 Intergranular Corrosion/Tensile Test Materials

Materials - 593°C (1100°F)

Incoloy 800
RA330
347
316
316L

Both parent metal and weld samples were tensile tested at ambient temperature, microsectioned, and metallographically examined for IGC. A 180° bend test was also performed on the weld samples.

2. Stress Corrosion Test (Creep)

The stress corrosion test was done to determine the susceptibility of candidate materials (both parent metal [PM] and welds) to corrosion cracking under stressed conditions. Stress conditions are those required to produce a 1% deformation in three different time frames.

Dog-bone specimens were contained in a vessel of molten salt maintained at 593°C (1100°F). A standard creep test machine was attached to both ends of the specimen to maintain a constant load throughout the test. Table VI-5 shows a test matrix for the stress corrosion specimens.

Table VI-5 Stress Corrosion Test Matrix

Material	Approximate Creep Rates		
	0.001%/hr	0.01%/hr	0.1%/hr
I-800 PM	3	3	3
I-800 Weld	6	6	6
RA330 PM	3	3	3
RA330 Weld	6	6	6
SS-347 PM	3	3	3
SS-347 Weld	6	6	6

Total creep strain was determined by measuring the cross-sectional areas of the specimen before and after testing. Each PM specimen was tensile tested and metallographically analyzed. In addition to this, the weld specimens were tested by a standard 180° bend test.

3. Thermal Cycling Tests

The purpose of these tests was to demonstrate the tenacity of the oxide passivation layer of sample coupons during severe thermal shock.

Three coupons each of Incoloy 800, 316L, 347, RA330, and carbon steel were given a 2000-hour passivation layer and then heated in an oven to 593°C (1100°F) for the stainless steels and 399°C (750°F) for the carbon steel. They were then immediately quenched in ambient temperature water. This cycle was repeated 50 times. The coupons were checked for weight change after each ten quench cycles and the passivation layer was optically analyzed at the end of the test for any degradation.

C. DYNAMIC TESTING - MOLTEN SALT FLOW LOOP

1. Objectives

The purpose of the molten salt flow loop is to simulate the thermal and fluid flow characteristics of a full-scale solar central receiver power system to permit the study of materials compatibility and salt stability in a dynamic system. Specifically, the loop simulates:

- 1) Fluid velocity - 3.5 m/s (11 ft/s) in the vicinity of the material samples,
- 2) Temperature profile - 566°C (1050°F) at the hot end of the loop, 288°C (550°F) at the cold end, and
- 3) Materials - the loop is constructed of Incoloy 800 at the hot end and carbon steel at the cold end.

The loop is designed to allow for the insertion and removal of sample coupons at various points in the flowing salt stream for analysis at 1000-hr intervals during the test. This dynamic testing permits the investigation of:

- 1) Mass transport phenomena from the high to the low temperature part of the loop;
- 2) Materials compatibility and erosion in a flowing molten salt system;
- 3) Chemical stability of the molten salt in a flowing, thermally-cycled system; and
- 4) Electrolytic corrosion phenomena (if any) in a flowing molten salt system.

2. System Design

Figure VI-1 shows a schematic of the molten salt flow loop. The sump contains molten salt maintained at 288°C (550°F). A cantilever pump pumps the salt through the inside tube of a counterflow heat exchanger where it is heated to 482°C (900°F). The salt is heated to 566°C (1050°F) in a three-stage electric resistance heater tube, then cooled to 371°C (700°F) as it passes through the outer tube of the counterflow heat exchanger. It then flows through a finned-tube forced convection air cooler and is returned to the sump at 288°C (550°F). Seven sample ports are located at various points along the test loop to permit insertion and removal of metal coupons and salt sampling.

Figure VI-2 shows the assembled flow loop. The pump and sump are located at the lower left. The three long legs of the counterflow heat exchanger can be seen at the left and the heater, located about 8 m (25 ft) from the floor, is at the top left. The air cooler is near the center of the photo and the control console is at the lower right.

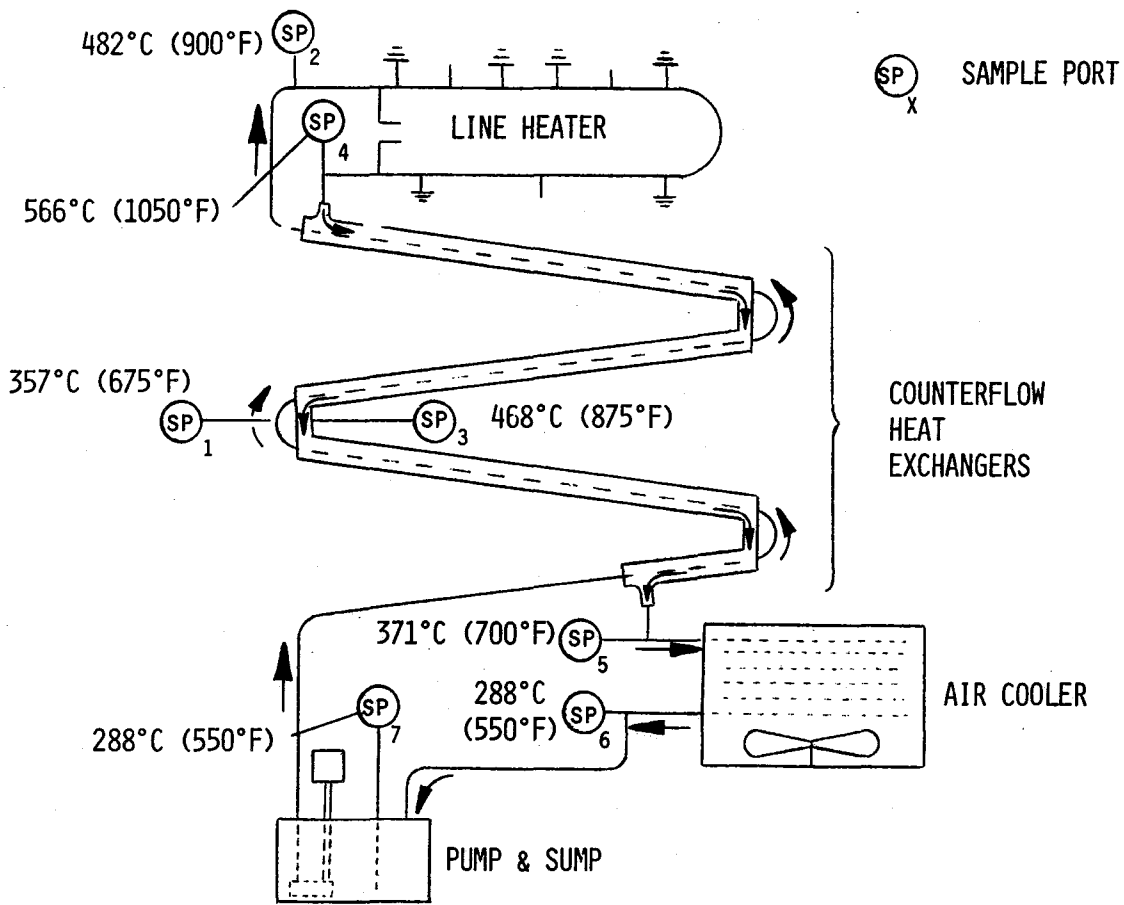


Figure VI-1 Molten Salt Flow Loop Schematic

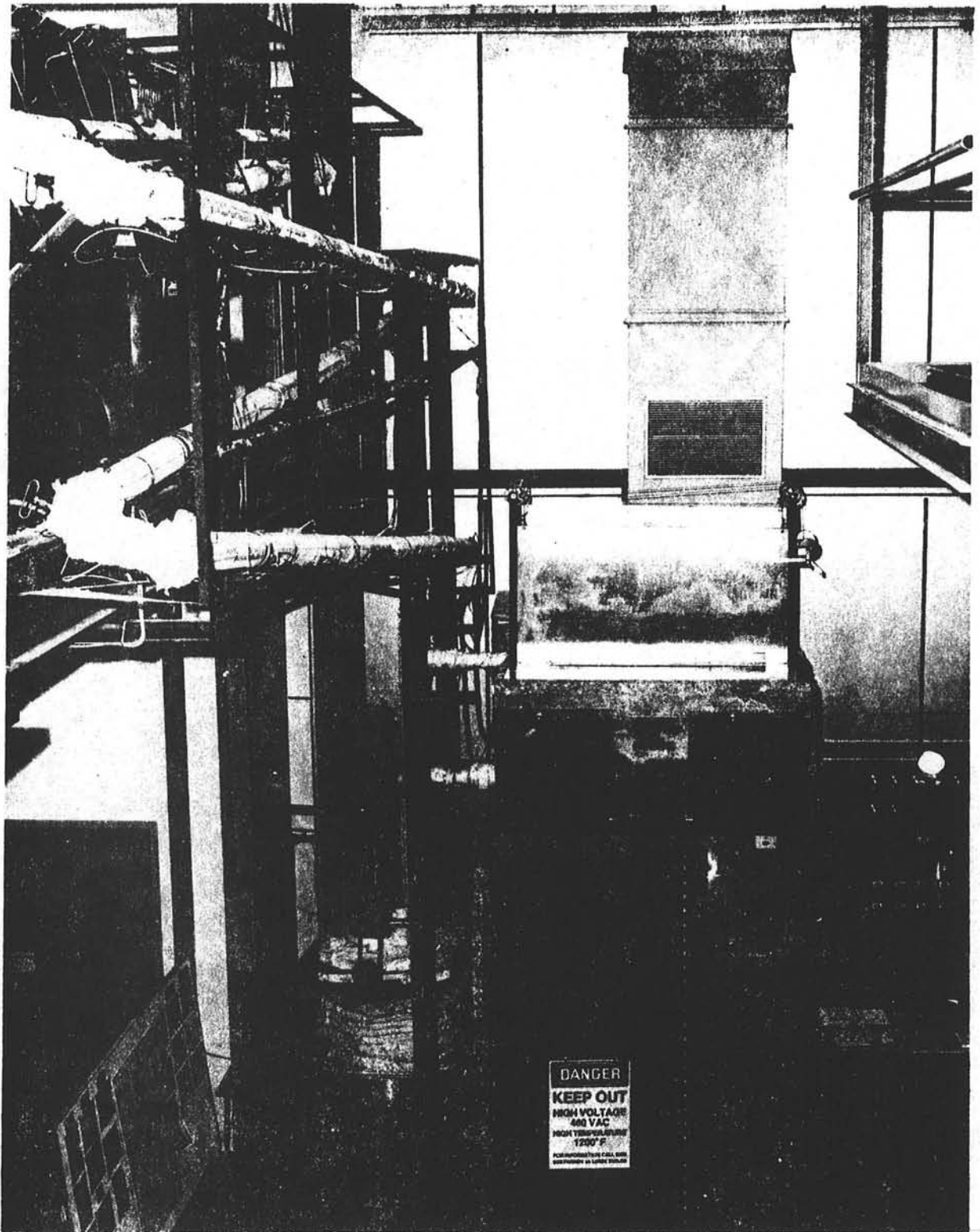


Figure VI-2 Long-Term Molten Salt Flow Loop

There are seven sample ports at various locations in the salt loop. Sample ports 1-4 (refer to the schematic, Figure VI-1) have Incoloy 800 coupons inserted into the salt flow stream, ports 5 and 6 have carbon steel coupons, and port 7 is used to sample the molten salt in the sump. Sample ports are designed so the fluid velocity across the coupons is approximately 3.5 m/s (11 ft/s), which is the design velocity of the salt flow in the full-scale molten salt central receiver system. The coupons are held in the salt stream on a removable sample holder, shown in Figure VI-3. The coupons are placed in slots in the holder, then inserted into the sample port.

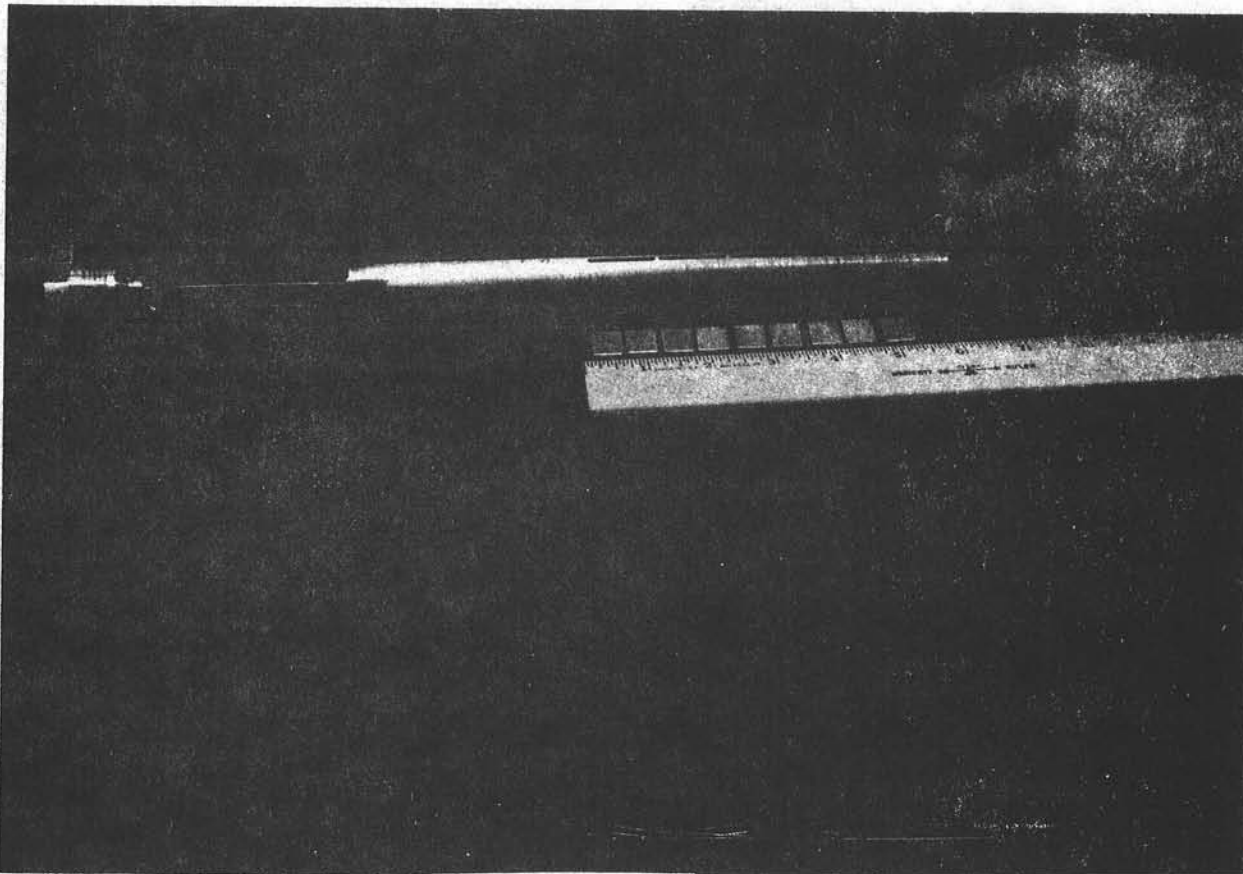


Figure VI-3 Materials Coupons with Holder

The system is designed for continuous unattended operation over a period of at least 5,000 hours. The material samples were checked every 1000 hours for weight change, and were metallurgically and chemically checked after the test was complete and at other times if weight-change data indicated significant mass transport. Molten salt samples were taken every 1000 hours and analyzed chemically as required.

D. SALT CHEMISTRY TESTS

1. Environmental Effects Test

The purpose of this test was to determine the effects of long-term exposure of the molten salt to ambient air.

Known quantities of CO₂ and water vapor were bubbled through approximately 300 g (0.66 lbm) of molten salt at 579°C (1075°F). Small Incoloy 800 test coupons were placed in each test vessel to determine the effects of long-term exposure to high CO₃⁼ and OH⁻ concentrations.

Table VI-6 shows a test matrix for this test. The salt was analyzed at the end of each test for hydroxides/oxides, carbonates, nitrates, nitrites, potassium, sodium, and chromium.

Table VI-6 Environmental Effects Test Matrix

TEST	GAS PURIFIED AIR	COMPOSITION H ₂ O	VOL % CO ₂	TEST TIME
A1	100%	0	0	1 Wk
A2	↓	↓	↓	5 Wk
A3	↓	↓	↓	15 Wk
A4	↓	↓	↓	28 Wk
B1	Balance	100% R.H.	0	1 Wk
B2	↓	↓	↓	5 Wk
B3	↓	↓	↓	15 Wk
B4	↓	↓	↓	28 Wk
C1	Balance	0	1.0%	1 Wk
C2	↓	↓	↓	5 Wk
C3	↓	↓	↓	15 Wk
C4	↓	↓	↓	28 Wk
D1	Balance	100% R.H.	1.0%	1 Wk
D2	↓	↓	↓	5 Wk
D3	↓	↓	↓	15 Wk
D4	↓	↓	↓	28 Wk

R.H. = Relative humidity at 31°C

2. Molten Salt Regeneration Test

This test was performed to evaluate the "in situ" regeneration of molten salt containing carbonates and hydroxides/oxides by exposure to gaseous nitrogen dioxide.

Molten salt at 288°C (550°F) containing carbonate and hydroxide/oxide dopants was exposed to gaseous nitrogen dioxide in the Incoloy 800 bubbler vessels used for the CO₂/water vapor tests. A test coupon of Incoloy 800 was placed in each vessel as well. The test matrix for this test is shown in Table VI-7.

Table VI-7 Molten Salt Regeneration Test Matrix

<u>Test No.</u>	<u>Initial Salt Comp</u>	<u>NO₂ Add Rate</u>	<u>Test Time</u>	<u>Final Salt Comp</u>	<u>% Reduction</u>
1	2.4% CO ₃ ⁼	5 cc/min	132 hr	0.6% CO ₃ ⁼	75
2	2.4% OH ⁻	5 cc/min	132 hr	<0.01% OH ⁻	100
3	2.3% CO ₃ ⁼ 2.3% OH ⁻	5 cc/min	132 hr	0.7% CO ₃ ⁼ 0.01% OH ⁻	70 100
4	2.3% CO ₃ ⁼ 2.3% OH ⁻	No NO ₂	132 hr	2.0% CO ₃ ⁼ 2.1% OH ⁻	15 10
5	Blank	5 cc/min	132 hr	<0.04% CO ₃ ⁼ <0.01% OH ⁻	--

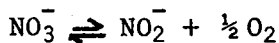
VII. MATERIALS AND SALT CHEMISTRY TEST RESULTS

A. SALT CHEMISTRY

The chemistry of molten nitrate salts is important in the development, design and operation of a power system which uses a mixture of sodium nitrate and potassium nitrate as the heat storage and transfer medium. These salts undergo chemical reactions at the proposed operating temperatures, and these reactions may affect properties of the salt such as heat transfer coefficients, heat capacities, melting temperatures, or compatibility with materials of construction. In addition, if the reaction product has limited solubility in the salt, precipitates might form at some region in the system where the solubility limit has been exceeded. In this section, salt chemistry, as determined from the static test programs, and its effect on power systems, are discussed.

1. Nitrite Formation

When mixtures of sodium and potassium nitrates are heated to the power system upper operating temperature, nitrate ion (NO_3^-) is converted to nitrite ion (NO_2^-) with the concurrent evolution of oxygen gas:



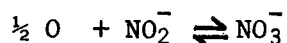
During Phase I of the Advanced Central Receiver Power Systems Program, a series of tests was conducted to determine the equilibrium of this reaction in molten salt (60% sodium nitrate, 40% potassium nitrate) at temperatures near 565°C (1050°F).

At 562°C, the value of the equilibrium constant (K_{eq}) was determined to be 0.022 atm^{1/2}. In an open system where venting of oxygen can occur, the extent of conversion of nitrate to nitrite is dependent only on the temperature and the pressure of oxygen above the molten salt. If the system is open to the air (Denver oxygen pressure in air equals 0.16 atm) at 562°C, the salt at equilibrium will contain 2.6% nitrite; if the air is replaced by oxygen at Denver ambient pressure (0.8 atm), the weight percent of nitrite ion will decrease to 1.1%. If the atmosphere above the system were continuously purged with nitrogen, the nitrite ion concentration would continue to increase because the oxygen pressure could not attain equilibrium values. If the molten salt is heated in a closed system where the oxygen pressure is not kept constant, but increases as nitrite is produced, the final oxygen pressure and extent of conversion to nitrite will depend on both the amount of salt initially present in the system, and the volume of the ullage space.

During Phase I, the relationship of the nitrite/nitrate equilibrium vs temperature was determined from salt samples heated in air to several temperatures.

In Table VII-1, the expected equilibrium constants and weight percents of nitrite ion, if the salt is heated in air (0.16 atm O₂), are listed for several temperatures. The expected weight percent of nitrite ion, negligible at 288°C (550°F), the lower operating temperature, increases to 3.0% at the 566°C (1050°F), the upper operating temperature.

The rates of the conversion of nitrate to nitrite have not been extensively studied. The rate of formation of nitrite ion is dependent on the oxygen pressure and the nitrite concentration and temperature; it is not dependent on the surface area of the salt or any agitation of the salt. However, the rate of the reverse reaction:



in which oxygen must be transported from surface to the inside of the salt, will be highly dependent on the salt surface area, agitation of the salt, the nitrite ion concentration and oxygen pressure.

One of the consequences of the formation of nitrate ion when molten salt is heated, is that heat will be required not only to raise the temperature of the salt, but also to produce the equilibrium concentration of nitrite ion. This relationship must also be considered whenever heat capacities are being calculated. If conversion to nitrite is not taken into account, erroneous heat capacities can be calculated.

Nitrite formation does not adversely affect the melting point of molten salt; addition of nitrite ion lowers the melting point of nitrate salts. The lowest temperature eutectic molten salt contains about 40% sodium nitrite. Nitrite ions are also highly soluble in nitrate salts; therefore, precipitate formation will not occur in molten nitrate salts whose only impurity is nitrite ion.

During the Environmental Effects Test a correlation was observed between nitrite and chromium concentrations in molten salt. Another example of the correlation between chromium and nitrite was found during the Phase I test in which the nitrite concentration reached 13%. After 6000 test hours the chromium concentration was 4000 ppm, the highest observed in any static test in Phases I or II.

One possible mechanism for this phenomenon is that chromium, initially oxidized by nitrate ions, complexes with nitrite ions to form soluble nitrito chromium complexes.

Table VII-1 Effect of Temperature on Conversion to Nitrite in Molten Salt

Temperature, °C (°F)	K_{eq} , ATM ^{1/2}	%NO ₂ ⁻ (Weight)
288 (550)	7.0 x 10 ⁻⁶	0.001
344 (650)	6.2 x 10 ⁻⁵	0.008
399 (750)	4.1 x 10 ⁻⁴	0.052
455 (850)	2.0 x 10 ⁻³	0.25
510 (950)	7.9 x 10 ⁻³	0.98
538 (1000)	1.5 x 10 ⁻²	0.19
566 (1050)	2.6 x 10 ⁻²	3.0
593 (1100)	4.4 x 10 ⁻²	5.0
621 (1150)	7.4 x 10 ⁻²	7.9

2. Carbonate/Hydroxide Formation

Another reaction which occurs in molten salt is the formation of oxides through decomposition of nitrites with concurrent evolution of nitrogen gas, nitric oxide (NO), or nitrogen dioxide (NO₂). Decomposition of nitrites to oxides becomes significant in sodium and potassium nitrates at temperatures above 700°C (about 1300°F). In all molten salt tests performed in the absence of atmospheric contaminants at temperatures up to 593°C (1100°F), oxide concentrations remained less than 0.05% even when high nitrite concentrations were present.

The reaction of molten salt with water vapor at 593°C appeared to reach equilibrium between one and five weeks. After that additional water did not appear to react with the salt at a significant rate.

Hydroxides are extremely soluble in molten nitrates [20% at 288°C (550°F)]. Oxides are much less soluble. However, it is unlikely that oxide concentrations would never reach their solubility limits [0.23% at 288°C (550°F) and 2.3% at 566°C (1050°F)]. However, there is a possibility that trace quantities of alkaline earths (calcium or magnesium) which may be present in commercial grade nitrates, and whose salts are less soluble than those of sodium or potassium, could form precipitates with oxides or hydroxides.

The reaction of molten salt with CO₂ is a concern. In these reactions the equilibrium is in the direction of carbonate rather than carbon dioxide. Virtually all of the carbon dioxide added (with dry air) to the molten draw salt in the 28 week test was converted to carbonate. In this test, the supernatant carbonate concentration (3.3%) was less than the carbonate concentration in the entire salt (4.6%) indicating that the solubility limit of carbonate was exceeded before the reaction reached equilibrium. Therefore, reaction of salt with carbon dioxide will never reach equilibrium; carbonate formation will continue as long as the salt is exposed to CO₂.

Formation of moderate concentrations of carbonate at upper operating temperatures may not create a solubility problem. However solubility problems can still occur when the salt is cooled. The solubility of carbonate decreases from over 3% at 566°C (1050°F) to 0.5% at 288°C (550°F). Therefore, even if carbonate concentrations are kept below the solubility limit at upper operating temperatures, precipitation of carbonates can occur when the salt is cooled. Carbonate ion may also react with trace quantities of alkaline earth elements to form species which are even less soluble than those formed with sodium or potassium.

3. Salt Regeneration Vs Atmosphere Control

In the preceding section, the severe impact of carbon dioxide on molten salt chemistry and the less severe effects of water vapor were discussed. In this section, a technique for removal of carbonates and hydroxides is compared with a technique for preventing contact of the salt with carbon dioxide or water vapor.

During the regeneration test, molten salt samples at 288°C (550°F), contaminated with carbonates and hydroxides, were regenerated by treatment with a mixture of nitrogen dioxide (NO₂) in air. Conversion of hydroxide to nitrate was 100% complete; conversion of carbonate to nitrate was 75% complete. The reduced efficiency of the carbonate conversion is a result of the carbonate/carbon dioxide equilibrium favoring carbonate to a greater degree than the hydroxide/water equilibrium favoring hydroxide.

B. DYNAMIC TESTING - MOLTEN SALT FLOW LOOP

1. Bulk Salt Chemistry

In a system in which molten salt undergoes thermal cycling, the extent of conversion of nitrate to nitrite and the rate at which equilibrium is established will depend on the residence time of salt at each temperature, oxygen pressures and ullage volumes in areas where salt is being heated; and on oxygen pressures, surface areas and degree of salt agitation in areas where salt is being cooled. In a system where molten salt temperature is cycled between 288°C and 566°C, nitrite concentrations would cycle between 0.001% and 3.0% if the salt were allowed time to equilibrate with air at both temperatures. The molten salt pumped fluid loop and the SRE receiver are not open to air at the high temperature end, but are vented at the sump (low temperature end). Residence time in the sump is much less than the time required for complete transport of oxygen throughout the salt. Therefore, in an operating thermal cycling system, bulk nitrite concentrations will be lower than 3.0% at 566°C and higher than 0.001% at 288°C.

In the salt pumped fluid loop, the nitrite ion concentration of the salts taken from the sump increased 1.23% after 4700 hours. The rate of increase was slow during most of the cycling. In the SRE receiver nitrite ion concentrations of salts taken from the sump increased from 0.08% to 1.26% during the time period from 7-20-80 to 12-1-80. Nitrite ion concentrations of salts, taken simultaneously from the 288°C and 566°C ends of the SRE, were virtually identical (1.13 ± 0.01%). It is anticipated that nitrite ion concentrations in the high temperature end of the salt pumped fluid loop at the end

of the test were also virtually identical to the 1.23% found in the sump. In both systems, a pseudo equilibrium nitrite concentration is reached throughout the entire system. The whole magnitude and rate at which this equilibrium is attained are function of design and operating parameters of the system. In both the SRE and in the loop, this pseudo-equilibrium nitrite concentration, although it may not have been reached during the test period, is not likely to be much greater than 1.2%. After nitrite concentrations reach equilibrium values in pumped systems in which thermal cycling occurs, all heat absorbed by the salt will be used only to increase the salt temperature.

The salts taken from the sump of the salt pumped fluid loop contained low concentrations of chromium. These increased from 4 ppm to 27 ppm as nitrite concentrations increased.

In both the salt pumped fluid loop and the SRE receiver, oxide and carbonate concentrations remained minimal (<0.05%) indicating that oxide and carbonate formation will remain minimal in operating systems if carbon dioxide and water vapor are excluded.

2. Reactions at Tube Walls

At the completion of the operation of the molten salt pumped fluid loop, the salt was drained and sections of the loop near the sample ports were removed. Water soluble salts, which had adhered to the wall of each section, were analyzed for nitrite and chromium.

There was a significant adherent coating on the samples and tubing near the outlet of the test loop. The coating was tan in color and was not soluble in water. Analyses showed that the material is probably a complex calcium/magnesium salt. This deposit is of concern because it could deposit on the heat exchangers in a commercial system and reduce their effectiveness. A commercial system containing millions of pounds of salt would have the potential to produce hundreds of pounds of Ca/mg salt coating.

3. Materials Samples

Incoloy 800 and A570 specimens were immersed at different temperatures exposed to a flowing salt loop to observe oxidation behavior. A noticeable shift in oxidation behavior was observed for the I800 as a function of temperature. The largest extrapolated loss was observed for the 440°C (825°F) immersion. Elemental concentrations of the salt at this location in the loop showed increased values of chromium and nitrite concentrations, thus indicating possible chromium leaching from the I800 metal substrate. This effect will have to be analyzed in detail. A570 showed direct temperature dependence on extrapolated metal loss, with accelerated metal removal at 399°C (750°F).

C. MATERIALS TEST RESULTS

1. Trace Contaminants

a. High-temperature alloys (I800, RA330, 316L, 347) - All of the alloys exposed to static, high-temperature, 580°C (1075°F), salt exhibited weight gain behavior for the first half of test exposure (~2000 hours), independent of trace contaminant addition. Subsequent weight loss for some alloys was attributed to an oxide sloughing dissolution process.

A rough estimate of 30-year extrapolated weight loss was performed assuming a cyclic weight gain-weight loss behavior. The number of these cycles (N) occurring in 30 years was determined and the 30 year weight loss was calculated by multiplying N by the peak weight gain/cycle (assuming weight gain magnitude * weight loss magnitude). For all of the alloys, the parent metal specimens exhibited lower extrapolated weight losses than welded specimens for all trace contaminant additions. Specifically, it appears carbonate ($\text{CO}_3^{=}$) trace additions represent the worst case for 316L and 347, chloride (Cl^-) for I800 and hydroxide (OH^-) for RA330. Metallographic examinations revealed a slight grain boundary penetration and surface oxide intrusion for 316L and 347 exposed to $\text{CO}_3^{=}$ additions and slight surface pitting and oxide intrusion for I800 exposed to Cl^- addition. No significant effects of contaminant additions were observed for RA330 based on visual and metallographic examination.

In summary, I800, 316L and RA330 appear to be acceptable for containment of molten (580°C) contaminated salt, realizing the assumptions used for extrapolation pertaining to RA330 oxide behavior. The high-chromium stainless steel 347 oxidation behavior needs to be examined further before its use is recommended.

b. Carbon and low-alloy steels (A570, A387) - Weight change curves for these materials showed a definite cyclic, weight gain-weight loss behavior, indicating competitive oxide growth, sloughing/dissolution processes. A570 exhibited greater oxidation resistance than A387 for all trace additions in 288°C (550°F) salt. Parent metal loss for A570 (288°C) was larger than metal losses extrapolated for welded specimens for all trace additions. No major microstructural abnormalities were observed for these alloys, although slight surface flaking was evident from visual examinations of carbonate ($\text{CO}_3^{=}$) and sulfate ($\text{SO}_4^{=}$) exposed coupons. In summary, A570 appears superior to A387 from extrapolated (30 year) weight/metal loss calculations in 288°C (550°F) salt. High temperature 399°C (750°F) use of A570 is not recommended, based on extrapolated metal loss results.

2. Extended Immersion

Extended immersion testing of candidate containment material was performed to observe long duration oxide behavior. The atmospheric control during these tests was not closely monitored, thus the level of contaminants is not precisely known. These tests were performed to observe the oxide behavior at times larger than simulated in the trace contaminant tests. Visual examinations showed RA330 and I800 to have developed tight, adherent oxides showing no evidence of flaking. Areas of oxide flaking on coupon surfaces were observed for 321, 316, A286 and 347. The ambiguous behavior of oxide growth-loss interactions is observed with A516. Its weight loss values appear reasonable, although visual examination showed a badly flaked and pitted coupon surface.

3. Surface Preparation Effects Test

A study was performed to analyze the possible effects of surface treatments (as-rolled vs as-machined) for A516, A570 and A387 exposed to blank salt at 399°C (750°F) for a period of 1000 hours. Visual examinations showed no significant effects of surface preparation treatment for these three alloys.

4. Special Purpose Materials Test

The Stellite #6 material (both parent metal and weld specimens were tested) displayed excellent corrosion resistance. Only localized areas of blue and brassy oxidative discolorations, were observed. Materials containing graphite composition, such as the Crane IX187 gasket and the Crane GF graphite packing reacted readily with molten salt, dissolving the graphite. Tungsten carbide formulations containing cobalt or nickel binders dissolved completely in molten salt, although silicon carbide displayed sustained corrosion resistance.

Metallic-foil packing material predictably reacted with the oxidizing molten nitrate salt. Copper foil blackened during only 1000 hours of exposure, and then dissolved completely after 5000 hours. Aluminum Crane 100 Al remained intact after 5000 hours of exposure to molten salt, although the metallic luster of the foil was lost, similarly, the Nickel Crane 100 Ni displayed excellent corrosion resistance to molten salt at 399°C (750°F).

5. Intergranular Corrosion/Tensile Test

It appears that the exposure of the candidate alloys to molten nitrate salts at 580°C (1076°F) for up to 9 months has no deleterious effects on alloy structural integrity or microstructural stability. From these results it appears that I800, RA330, 347, 316 and 316L are acceptable for molten salt containment at 580°C.

The austenitic stainless steel 316 and high-nickel I800 were shown to be susceptible to sensitization, due to their high carbon contents.

The effects of high carbon compositions (and, therefore, a sensitized microstructure) on the electro-chemical corrosion behavior after long-term molten salt exposures is not known at this time.

6. Stress Corrosion/Creep Loading Test

The comparison of the total creep rate in molten salt with literature values for creep rates of high temperature air exposures would give limited usefulness. The range of strain during the salt exposures indicates the major portion of the test is within the primary portion of the total creep curve, where typical literature values are for secondary, steady state creep.

Creep loading of the high-nickel alloys I800 and RA330 in molten salt at 580°C (1076°F) showed minimal degradation in terms of structural integrity or microstructural alterations. The variation in room temperature mechanical properties for I800 is the result of the combined effects of a thermal treatment on a high carbon material.

7. Thermal Cycling Test

The effects of thermal cycling by repeated heating/cooling cycles on material oxide integrity were evaluated. Metallographic and visual inspection of I800, RA330, 347, 316L and A570 showed no evidence of accelerated flaking after repeated temperature cycling.

Table VII-2 Room Temperature Tensile Properties of Materials
after Nine Months Salt Exposure

Material	Environment	Tensile Strength MPa	Yield Strength MPa	Elongation %
I-800	Unexposed	668	427	40
Parent Metal	Air, 580°C (8 months)	706	412	NR
	Salt	716	426	34
Welded	Salt	727	430	NR
316L	Air, 580°C (8 months)	643	304	63
Parent Metal	Salt	640	302	60
Welded	Salt	631	333	34
347	Air, 580°C (8 months)	761	457	46
Parent Metal	Salt	749	449	37
Welded	Salt	717	415	23
316	Air, 580°C (8 months)	663	292	54
Parent Metal	Salt	668	306	45
Welded	Salt	651	333	34
RA330	Unexposed	599	289	45
Parent Metal	Air, 580°C (8 months)	658	350	NR
	Salt	636	335	42
Welded	Salt	636	339	NR

NR = Not Reported

VIII. CONCLUSIONS AND RECOMMENDATIONS*

The basic conclusion of the program is that we strongly believe that commercial solar central receivers using molten salt as the heat transfer fluid can be designed with a high confidence that they will be successful. Specific conclusions based on our experience in this program are given below.

A. HARDWARE-ORIENTED OBSERVATIONS

- a. The overall performance of the hardware was very good. No unique manufacturing techniques or quality control procedures required.
- b. The use of bellows-type seals in valves is sufficient to prevent leakage of salt.
- c. The use of standard slopes of 1 cm/m (1/8 in./ft) in piping to assure drainability of molten salt is adequate.
- *d. Trace heater systems for commercial molten salt applications require more development. The use of MI cabling with one-conductor Nichrome elements 22 gage or larger is recommended.
- *e. Surface preparations for the application of Pyromark paint requires definition and standardization. This should probably include sandblasting.
- f. There should be no tube-to-tube welding between passes.
- *g. The performance of the flow control valve was marginal, an improved valve design for this application is required.

B. THERMO-HYDRAULIC PERFORMANCE

- a. Pumping requirements and heat transfer characteristics with molten salt as the heat transfer fluid are predictable by the use of standard correlations such as the D'Arcy-Weibach formula and the McAdams equations.
- b. No turbulent to laminar transitions were observed above $Re=4000$.
- c. No significant effects on heat transfer or pressure drop due to heating or high temperatures were observed.

An asterisk (*) ahead of an item indicates requirement for future development in the area.

- d. Draining by gravity is adequate. The use of purge gas to force the salt out of the system provided no improvement.
- e. The thermal mass of the salt was sufficient to prevent local freezing during drain operations with the cavity doors open.
- f. Pump performance was within specifications.

C. THERMAL PERFORMANCE (EFFICIENCIES)

- a. The efficiency of the receiver is $85.3 \pm 5.0\%$ at 5 MW input.
- b. The input-output relationship for a molten salt receiver is a straight line, with a negative intercept on the output axis.
- c. Flux distribution inside the cavity is an important consideration in design. A large percentage of incident fluxes on inactive surfaces will degrade performance, as evidenced by observations during the "high-flux" tests.
- *d. Available techniques for the measurement of input, output, and losses from the receiver need to be improved. Specific improvements are needed in the following areas:
 - molten salt properties, especially specific heat
 - reduction of uncertainties associated with the RTAF measurements
 - techniques for the measurement of radiation losses through the cavity aperture
 - measurement of receiver tube sun-side metal temperatures
 - correlations for the estimation of convection losses with sun-on conditions
- *e. The receiver efficiency should be recalculated using solar-calibrated RTAF flux gage data and an accurate value for the salt specific heat.
- f. The semi-empirical "input-loss" approach, combining analyses and test data, is believed to be the most accurate method of efficiency determination available within present state-of-the-art.

D. THERMO-STRUCTURAL PERFORMANCE

- a. The highest stresses in the SRE were in compression. This raises some questions regarding the use of the ASME Code Case 1592 criteria, which are based on allowables in tension.
- b. The design should be configured so that tack welds do not fail and at the same time so that they do not induce excessively high local tube stresses. The tack welds in each pass should be sufficient to maintain planarity, and each pass and header should be attached individually to the supporting structure so as to allow only for differential lengthening of each pass. Tubes between passes and headers should not be welded.

- *c. Testing of welds, both statically and in fatigue, at elevated temperature, is recommended.
- d. More extensive use of non-linear finite element modeling is recommended.
- *e. There is need for more detailed tube temperature distribution data.
- *f. A test program to check combined creep and fatigue damage should be defined.

E. OPERATIONAL RELIABILITY

- a. The use of heliostats for warmup requires monitoring and changes in procedure according to the time of the day and time of the year. Alternate techniques - such as continuous salt circulation - is recommended for the commercial design.
- *b. Control requirements need more precise definition for the commercial receiver than available for the SRE. Consideration should be given to the effect on the life of the receiver of input-fluctuations due to clouds.
- *c. The SRE analog and algorithm controls were marginally successful. Further work is required in the areas of design, analytical simulation, and experimental verification of receiver control systems.
- d. The SRE has withstood the rigors of five months of experimentation with solar operation, including 153 cycles of accelerated life testing, approximately another 100 cycles due to startups and clouds, and margin testing at higher than design flux levels. This may be construed as successfully passing a necessary (but not sufficient) test to prove the long life expectancy of the SRE.
- e. No safety problems with equipment or personnel were encountered during the program.

F. SALT CHEMISTRY

- a. The stability of molten salt is adequate for long-term solar use with carbonate and hydroxide control (by either scrubbing or salt regeneration).
- *b. There is a need for further investigation of the deposits found in the intermediate temperature sections of the molten salt loop. This may be accomplished by laboratory-scale test-simulation of the conditions leading to such deposits. This is necessary due to the potential for heat exchanger fouling as systems requiring large amounts of salt are operated.

- *c. Further investigation is required to determine the effect of nitrate/nitrite equilibrium on chromium leaching.
- *d. Preliminary economic estimates of atmospheric scrubbing and salt regeneration favor the former method of carbonate and hydroxide control. The need for more complete economic studies in this area is indicated.

G. MATERIALS TESTS

- a. I800 and RA 330 are acceptable materials for long-term high-temperature [up to 580°C (1076°F)] service. 316 and 316L may also be suitable, pending further investigations.
- *b. Control of the carbon content of I800 and RA 330 may be necessary to minimize possible long-term structural degradation of these alloys. (Particularly if sensitization is found to be detrimental to long-term service behavior.)
- c. There were no salt-related detrimental effects on either the oxidation behavior or the structural integrity of I800 and RA 330.
- d. It is recommended that this investigation be extended to other candidates for intermediate temperature (280-480°C) alloys - [possibly from the low-chromium ferritic steel (2¼ Cr - 1 Mo) family].
- *e. Additional mechanical testing in molten salt environments should include creep-fatigue interactions, and slow strain rate testing.
- *f. Based on visual examination of a limited number of carbon steel test coupons, there were no indications of significant effects of surface preparations on material behavior. There is a need to investigate the possibility of passivating tube surfaces to prevent initial high corrosion or oxidation.
- g. The carbon steels are suitable low-temperature molten salt containment materials, up to 288°C (550°F).
- h. The low alloy steel A387 (1¼ Cr - ½ Mo) appears to be a suitable candidate for low-temperature service (up to 288°C) provided chloride (Cl⁻) impurity levels in the molten salt are controlled.
- j. Carbon steels appear to be a suitable intermediate-temperature containment material if proper design allowances can be made for material loss.

H. MOLTEN SALT FLOW LOOP

- a. There is no evidence of material transport in the molten salt flow loop.
- *b. The flow loop tests should be continued for the following reasons:
 - Determine the long term weight loss of the specimens.
 - Examine the effect of preoxidizing the surfaces in air on the weight loss.
 - Investigate the cause of the tan colored deposit at the low temperature end of the loop.
- *c. It is recommended that molten salt samples from both the high, and low temperature ends of the loop be analyzed for nitrite to verify that a pseudo-equilibrium exists in the loop.
- *d. Water-insoluble precipitates from coupons and loop sections should be subjected to elemental analyses, x-ray diffraction and infrared spectroscopy. Similar analyses should be conducted of residues from the sump. Also, sections of the SRE should be analyzed if possible.
- e. I-800 coupons exposed to flowing salt in the loop exhibited similar weight gains at 565°C (1050°F) as those in the trace contaminants tests. Coupons at 329°C (625°F) and 482°C (900°F) exhibited minor weight changes. The largest changes occurred at the 440°C (825°F) sample port, and accelerated with time.

UNLIMITED RELEASE
INITIAL DISTRIBUTION

UC-62E

U. S. Department of Energy
Forrestal Building
1000 Independence Avenue, S.W.
Washington, D.C. 20585

Attn: H. Coleman
C. Carwile
K. Cherian
C. Mangold
M. Scheve
T. Wilkins

U. S. Department of Energy
P. O. Box 5400
Albuquerque, NM 87115

Attn: G. Pappas
J. Weisiger

U. S. Department of Energy
1333 Broadway
Oakland, CA 94612

Attn: R. Hughey
G. Katz
W. Lambert

University of California
Department of Electrical and
Computer Engineering

Davis, CA 95616
Attn: M. Soderstrand

University of Houston
Solar Energy Laboratory

4800 Calhoun
Houston, TX 77704
Attn: A. Hildebrandt

Aerospace Corporation
2350 El Segundo Blvd.
El Segundo, CA 90245

Attn: P. Munjal

ARCO Power Systems
7061 S. University, Suite 300
Littleton, CO 80122

Attn: F. Blake
D. Gorman

Arizona Public Service Company
P. O. Box 21666
Phoenix, AZ 85036
Attn: J. McGuirk
E. Weber

Babcock and Wilcox
91 Stirling Avenue
Barberton, OH 44203
Attn: G. Grant
I. Hicks
D. Smith

Badger Energy, Inc.
One Broadway
Cambridge, MA 02142
Attn: C. A. Bolthrunis

Bechtel Group, Inc.
P. O. Box 3965
San Francisco, CA 94119
Attn: G. W. Braun
J. Darnell

Black and Veatch Consulting Engineers
P. O. Box 8405
Kansas City, MO 64114
Attn: J. C. Grosskreutz
J. E. Harder

Boeing Engineering and Construction Co.
P. O. Box 3707
Seattle, WA 98124
Attn: R. B. Gillette

Burns & McDonnell
P. O. Box 173
Kansas City, MO 64141
Attn: M. Soderstrum

California Energy Commission
1111 Howe Avenue, MS-70
Sacramento, CA 95825
Attn: D. Pierson

Combustion Engineering, Inc.
1000 Prospect Hill Road
Windsor, CT 06095
Attn: C. R. Buzzuto

IEA/SSPS
c/o DFVLR
Apartido 19, Tabernas
Almeria, Spain
Attn: C. Selvage

El Paso Electric Company
P. O. Box 982
El Paso, TX 79946
Attn: J. E. Brown

Electric Power Research Institute
P. O. Box 10412
Palo Alto, CA 94303
Attn: E. DeMeo

Foster Wheeler Development Co.
12 Peach Tree Hill Road
Livingston, NJ 07039
Attn: S. F. Wu
R. Zoschak

Georgia Institute of Technology
Atlanta, GA 30332
Attn: C. T. Brown

Gibbs and Hill, Inc.
393 Seventh Avenue
New York, NY 10001
Attn: J. J. Jimenez

Institute of Gas Technology
Suite 218
1825 K. Street, N. W.
Washington, D. C. 20036
Attn: D. Glenn

Martin Marietta
P. O. Box 179, L#0450
Denver, CO 80201
Attn: T. Heaton
T. Tracey

McDonnell Douglas
5301 Bolsa Avenue
Huntington Beach, CA 92647
Attn: C. Finch
L. Glover

Olin Chemicals Group
P. O. Box 2896
Lake Charles, LA 70624
Attn: J. Morgan

Olin Chemicals Group
120 Long Ridge Road
Stamford, CT 06904
Attn: F. N. Christopher
L. C. Fiorucci

Pacific Gas and Electric Company
3400 Crow Canyon Road
San Ramon, CA 94526
Attn: H. E. Seielstad

Pacific Northwest Laboratories
P. O. Box 999
Richland, WA 99352
Attn: B. Johnson
S. Hauser

Public Service Company of New Mexico
P. O. Box 2267
Albuquerque, NM 87103
Attn: A. Akhil

Rockwell International
Energy Systems Group
8900 De Soto Avenue
Canoga Park, CA 91304
Attn: T. Springer
A. Ullman

Solar Energy Industries Association
1156 5th Street, NW
Suite 520
Washington, D.C. 20005
Attn: C. LaPorta

Solar Energy Research Institute
1617 Cole Boulevard
Golden, CO 80401
Attn: J. Anderson
M. Murphy
L. Shannon

Southern California Edison
P. O. Box 800
Rosemead, CA 92807
Attn: J. N. Reeves
P. Skvarna
R. W. Williamson

Stearns-Roger
P. O. Box 5888
Denver, CO 80217
Attn: W. R. Lang

Stone & Webster Engineering Corporation
P. O. Box 1214
Boston, MA 02107
Attn: R. W. Kuhr

Westinghouse Electric Corporation
Advanced Energy Systems Division
P. O. Box 10864
Pittsburgh, PA 15236
Attn: J. R. Maxwell

D. G. Schueler, 6220
J. V. Otts, 6222
R. S. Claassen, 8000; Attn: D. M. Olson, 8100
A. N. Blackwell, 8200
D. L. Hartley, 8300

C. S. Selvage, 8000A
R. J. Gallagher, 8124
M. E. John, 8125
J. Kraabel, 8132
R. L. Rinne, 8220
L. Gutierrez, 8400; Attn: R. A. Baroody, 8410
A. C. Schuknecht, 8420
H. Hanser, 8440
J. F. Barham, 8460

J. B. Wright, 8450
A. C. Skinrood, 8452
D. N. Tanner, 8452
W. G. Wilson, 8453
J. B. Woodard, 8454
Publications Division 8265, for TIC (27)
Publications Division 8265/Technical Library Processes Division, 3141
Technical Library Processes Division, 3141 (3)
M. A. Pound, 8424, for Central Technical Files (3)